DOE/BC/15167-1

(OSTI IT: 807213)

OPTICAL FIBER SENSOR TECHNOLOGIES FOR EFFICIENT AND ECONOMICAL OIL RECOVERY

Annual Report

DOE Award Number – DE-FG26-98BC15167

Reporting Period Start Date – 1 October 2000
Reporting Period Stop Date – 30 September 2001

Prepared by: A.Wang, G. Pickrell, H. Xiao and R. May
Report Issued: 31 October 2001

Submitted by: Center for Photonics Technology
Bradley Department of Electrical and Computer Engineering
Virginia Tech - M/C 0111
Blacksburg, VA 24061

CPT
CENTER FOR PHOTONICS TECHNOLOGY

Disclaimer

"This report was prepared as an account of work sponsored by an agency of the United States Government. Neither the United States Government nor any agency thereof, nor any of their employees, makes any warranty, express or implied, or assumes any legal liability or responsibility for the accuracy, completeness, or usefulness of any information, apparatus, product, or process disclosed, or represents that its use would not infringe privately owned rights. Reference herein to any specific commercial product, process, or service by trade name, trademark manufacturer, or otherwise does not necessarily constitute or imply its endorsement, recommendation, or favoring by the United States Government or any agency thereof. The views and opinions of authors expressed herein do not necessarily state or reflect those of the United States Government or any agency thereof."

Executive Summary

This report summarizes the technical progress during the third year of the Optical Fiber Sensor Technologies for Efficient and Economical Oil Recovery program, funded by the National Petroleum Technology Office of the U.S. Department of Energy, and performed by the Center for Photonics Technology (CPT) of the Bradley Department of Electrical and Computer Engineering of Virginia Tech.

Based on the intensive research work performed through the second year of this project the self-calibrated interferometric/intensity-based (SCIIB) sensor head has been demonstrated to show high sensitivity and posses a robust structure. During the third year of this project, the performance of the sensor head has been improved dramatically. By selecting suitable materials for the glass tube and optical fiber, the temperature dependence of pressure sensor has been minimized. To eliminate the pressure dependence of the temperature sensor, a special glass tube was applied, which isolates the sensor head from the outside pressure. A thin metal foil based technique was developed to encapsulate the sensor head with a special package, which serves both as a mechanical protector and a waterproof isolation medium. The sensor was successfully deployed through Chevron's hydraulic deployment method into a test well in Coalinga, California. The performance of the sensor head is being evaluated down-hole during this first oil site test.

The SCIIB signal demodulation system was further improved during this third year. Most of the important noise sources were analyzed and identified both by theoretical analysis and by experiment. Several compensating structures were designed which improved the system stability as described further in this report.

To satisfy the strict performance requirements for the pressure and temperature sensors, a spectrometer based white light signal demodulation system was developed during this period. By using a novel data processing method invented at the CPT, the stability of this system is better than 0.5psi with a 6000psi dynamic range. The resolution of the white light system has been shown to be 0.03nm corresponding to 0.03 psi for the pressure sensor system.

During the first field test, the deploy-ability of the sensor head has been verified, the remote data access through Internet has been realized and the long term stability of the sensor head in down-hole environment is currently under evaluation.

Both the fiber optic flow measurement system and acoustic measurement system have been constructed at CPT. Encouraging results have been achieved. Details of these works are presented in this report.

Table of Contents

Executive Summary
1.0 Introduction ……... 1
2.0 Signal demodulation system I—SCIIB system …… 1
2.1 Review about SCIIB system …….. 1
2.1.1 Basic configure uration and operating theory ……. 1
2.1.2 The advantages of SCIIB system …… 4
2.1.3 Opportunities for Further Improvements …….. 5
2.2 Improvement on the SCIIB system ……. 6
2.2.1 Temperature compensation of the SCIIB system …….. 6
2.2.2 Other proposed signal demodulating structures ……..22

3.0 Signal demodulation system II-white light interferometer ……... 23
3.1 Basic configurations and operating theory …… 23
3.2 Novel data processing method ……... 26
3.3 Design and implementation …….. 29
3.3.1 Hardware design and system fabrication ……... 30
3.3.2 Software design and program development …….. 33
3.4 The performance of white light system ……... 42
3.5 Compare between the SCIIB system and the white light system …….. 48

4.0 Pressure and temperature sensor fabrication …… 50
4.1 Sensor fabrication system …… 50
4.1.1 CO2 laser sub-system ……... 52
4.1.2 White light optic fiber interferometer sub-system …… 52
4.1.3 EFPI pressure sensor fabrication ……... 53
4.1.4 Regular single mode fiber sensor …….. 55
4.1.5 Regular multimode fiber sensor …… 55
4.1.6 Carbon coated multimode-single mode combo fiber sensor …….. 56
4.1.7 Prevent from leaking …… 58
4.1.8 Reduce the temperature sensitivity …… 58
4.2 Precise air-gap control …….. 58
4.2.1 Gauge length …….. 59
4.2.2 Eliminate nonlinearity …….. . 59
4.3.1 EFPI temperature sensor fabrication …… 60

5.0 Description of optic fiber sensor packaging ……. 61
5.1 Structure features of the fiber sensor protection package …….. 62
5.2 Description of the packaging process …… 63

6.0 Testing results of pressure and temperature sensors …….. 63
6.1 Testing results of pressure sensor …….. 64
6.2 Testing results of temperature sensors …… 65
6.3 First field test in Coalinga, CA …….. 69
6.3.1 Sensor deployment …… 69
6.3.2 Remote Access and Control …… .. 69
6.3.3 Long-term stability ……. 72

7.0 Fiber optic flow sensor …… 73

7.1 Principle of fiber optical flow sensor ……. 74
7.2.1 Flow sensor fabrication …… 77
7.3 Flow sensor testing system design …… 79
7.4 Experiments and results ……. 80
7.4.1 Sensor calibration …… 80
7.4.2 Resolution of flow rate measurement ……. 81
7.4.3 Sensor repeatability ……. 82
7.4.4 Long-term stability …….. 83
7.4.5 Opportunities for improvement …….. 84

8.0 Fiber Optical Acoustic Sensor …… 84
8.1 Principle ……. 85
8.2 Sensor frequency response and sensitivity design ……. 86
8.3 Acoustic sensor fabrication …… 89
8.3.1 Setup of acoustic testing system ……. 90
8.4 Experiments …… 91

1.0 Introduction

The overall goal of this three and one half year program is to develop reliable cost effective sensors for application in the down-hole environment. The physical parameters to be measured by these sensors are temperature, pressure, flow and acoustic signals. Sensor head configure urations for each of the physical measurands will be optimized to increase the sensitivity to the particular measurand of interest while decreasing the cross-sensitivity to the other physical measurands and to environmental influences. In addition, the optical signal demodulation electronics will be designed to be insensitive to environmental influences while maintaining the required resolution, precision and accurancy of the parameter being sensed. The influence of potentially detrimental agents such as water in the down-hole environment will be investigated as will methods to protect both the optical fiber and the sensor from these detrimental effects. The experimental design, results, and discussion in each of the areas mentioned above will be presented in this report.

2. Signal demodulation system I—SCIIB system

The self-calibrated interferometric/intensity-based (SCIIB) signal demodulation system combined with an extrinsic fiber Fabry-Perot interferometer (EFPI) sensor head has been shown to perform very successfully as a fiber optic sensor system. In this chapter, after a brief review of the results acquired during the second year and procedures to improve the performance of SCIIB system will be presented in detail.

2.1 Review about SCIIB system

In this section, the theory and implementation of the SCIIB system will be reviewed, then both the advantages and opportunities for improvement of this system are demonstrated

2.1.1 Basic configuration and operating theory

One of the major advantages of fiber optic sensors is their high sensitivity. Almost any physical parameter which acts on the optical fiber will influence some properties of the light propagating in this optical fiber. However, the high sensitivity of the optical fiber to some kinds of disturbance will induce poor long-term stability. To overcome this disadvantage, fiber optic sensors operated in the field site are armed with some compensating protective structures.

The self-compensation in the SCIIB system is realized by introducing an intensity-based reference channel. The basic configuration of the SCIIB system is shown in Figure 2.1.

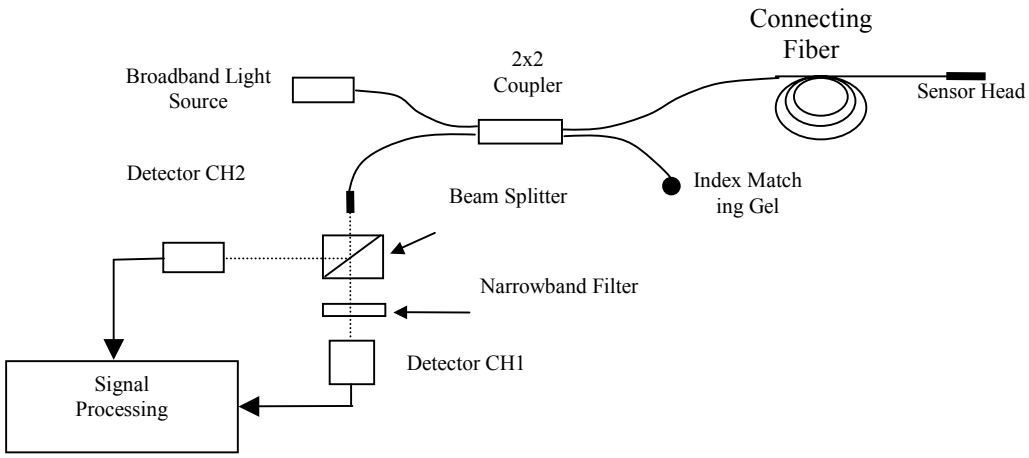

Figure 2.1 Illustration of the structure of the SCIIB

A broadband light source is used in the SCIIB system. For the multimode SCIIB system (which is suitable for short distance application), the light source is an 850nm LED. In the single mode system, a 1310nm SLED is used. Through a 2x2 fiber coupler, the optical power output from the light source is launched into the connecting fiber and propagates to the EFPI sensor head. The light signal reflected from the sensor head travels back along the same fiber and returns from the other port of the 2x2 coupler. A cubic beam splitter is used to split the received light signal into two parts: the first part passes through a narrowband optical filter, then is coupled into the photo detector of channel 1 (signal channel); the second part is coupled into the photo detector of channel 2 (reference channel) directly. Amplified by two symmetric low-noise amplifiers, the output signals from CH1 and CH2 are sampled into the PC by a high resolution A/D converter. Then, the ratio CH1/CH2 is calculated and is used to demodulate the physical parameter to be measured.

The reflection from the interface between the end-face of the optic fiber and air is about 4%, which means the sensor head is a low finesse Fabry-Perot interferometer, such that the two light beam interference method can be used in the theoretical analysis.

Suppose the output signals from CH1 and CH2 are I_1 and I_2, then the ratio R can be expressed as:

$$R = \frac{I_1}{I_2} \approx \frac{\int_{-\infty}^{\infty} I_{CH1}(\lambda)[1-\cos(\frac{4\pi}{\lambda}G)]d\lambda}{\int_{-\infty}^{\infty} I_{CH2}(\lambda)[1-\cos(\frac{4\pi}{\lambda}G)]d\lambda} \tag{2.1}$$

Here, G is the air-gap, and $I_{CH1}(\lambda)$ and $I_{CH2}(\lambda)$ are the power spectral density distributions of CH1 and CH2 respectively. Both of these channels have the Gaussian profiles.

The integral in equation (2.1) can be calculated numerically. Here, a rough picture is described based on basic physical views. The difference between CH1 and CH2 is the use of the narrowband optical filter in CH1. The spectral bandwidth in CH1 is about 10nm,while in CH2, the spectral bandwidth is about 60nm. Because the coherent length is inversely proportional to the bandwidth, so the coherent length in CH1 (L_{C1}) is much larger than the coherent length in CH2 (L_{C2}). When the air-gap G is much smaller than both L_{C1} and L_{C2}, the interference fringes will be observed in the two channels. On the other hand, if the air-gap G is much larger than both L_{C1} and L_{C2}, then, no interference exists in either channel 1 nor channel 2. If the air-gap G was set at a suitable range ($L_{C1}>G>L_{C2}$), then only the narrowband signal in channel 1 exhibits obvious interference and for the broadband signal in channel 2, no obvious interference exists. Because the two channels share the same light source and the same fiber, any fluctuations in light source or any changes in fiber loss will induce exactly the same influence on the signals in both channels, so the signal in channel 2 can act as a compensating signal for the signal in channel 1.

The relation of the output signal R and air-gap G, which is described by equation (2.1), is roughly a *SINE* function. A simulated curve is shown in Figure 2.2.

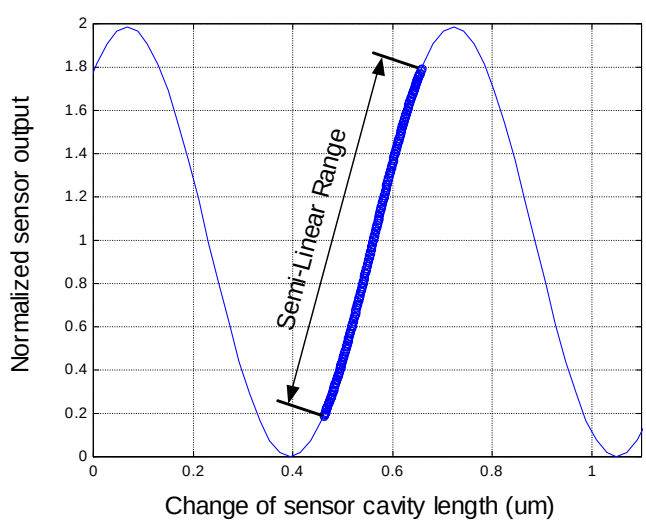

Figure 2.2 The linear range of SCIIB system

To avoid the ambiguity problem and realize a high sensitivity, the EFPI sensor should be operated in the linear range of a half fringe. This means the dynamic range of air-gap is about 1/6 of the light wavelength. (In the signal mode SCIIB system, a 1300nm SLED was used, so the dynamic range of the air-gap is about 200—300nm). The limited dynamic range is one of the major shortcomings of SCIIB system, which will be discussed further in next section. Because of this, although the pressure (or temperature) sensitivity of the sensor head can be increased by changing the geometrical parameters of the sensor head or the materials for glass tube, the dynamic range of pressure (or temperature) will be decreased by the same scale.

2.1.2 The advantages of SCIIB system

In addition to the generic fiber sensor advantages such as small size, lightweight, remote operation, immunity to EMI, electrically non-conducting, and chemically inert, the other advantages of the SCIIB system combined with EFPI sensor are summarized as below:

Ultra-high sensitivity:

The SCIIB fiber optic sensor can offer a very high resolution since the essence of the signal processing is based on interferometry.

Absolute measurement:

The operating range of the SCIIB sensor is limited to the semi-linear range of half of an interference fringe; therefore the sensor output is a unique and almost linear function of the change of the cavity length. The one-to-one relation between the sensor output and the cavity length makes it possible to measure the absolute value of the sensor cavity length after the initial cavity length is chosen and fixed. Not only is the direction ambiguity problem solved, but also the sensitivity of the sensor is kept relatively constant during the entire operating range.

Minimized complexity in signal processing:

Because the signal processing of the SCIIB sensor only involves optical power detection and a simple ratio operation of the two output signals, the complexity of the system is kept to its minimum level.

Self-compensation capability:

Since the original broadband source spectrum is used as a reference signal, the drift of the optical source power and fluctuations in fiber attenuation are thus fully compensated by the SCIIB signal processing.

High speed:

Because of the very simple signal processing used, the SCIIB sensor potentially has a very high frequency response, which may be applied to detect very high-speed signals such as acoustic waves.

2.1.3 Opportunities for Further Improvements

Although great strides have been achieved with the SCIIB system achieved during the second year, some problems also emerged. These opportunites for improvement provided the focus for the research for the third year.

In general, the two most important specifications for judging a measurement system are resolution and long-term stability.

Usually, the ultimate limit of the performance of an opt-electronic sensor system is associated with both the sensor head and the signal demodulation system. Instabilities in the signal demodulation electronics can originate from a variety of sources. The noises in the signal demodulation system can be further decomposed into two sources: the receiving electronics and the optical components.

As discussed previously, the basic optical components in the SMF SCIIB sensor system include the optical source (SLED), fiber coupler, optical fibers, GRIN lens, beam-splitter, and optical band-pass filter. In order to achieve the desirable performance of the sensor system, it is necessary for those optical components to perform their functions accurately. Unfortunately, environmental perturbations, such as temperature changes and mechanical vibrations, can easily introduce noises to the system through the interaction between the optical components and the outside medium. These noises may deviate the optical components from their desired functions and result in measurement errors.

The two main noise sources in the receiving electronics are the photo-detector and the pre-amplifier. In general, these parts are insensitive to the spectrum and polarization of the light signal. The most important issues here are linearity, temperature dependence and long-term drift. For high-speed application, special attention must be paid to the frequency response.

In this subparagraph, the main noise sources induced by different components in the SCIIB system will be discussed briefly. The efforts to solve these problems will be presented in the next paragraph.

Light Source:

Although the output of the SCIIB system is insensitive to the power fluctuation of the light source, the spectrum changes (which is mainly introduced by the temperature change) definitely introduces errors, especially when the central wavelength of the light source doesn't match with the central wavelength of the optical filter. To decrease the wavelength shift of the light source, an automatic thermoelectric cooling system was incorporated to stabilize the temperature of the light source. To reduce the mismatch between these two center wavelengths, the optical band-pass filter was rotated by an angle of about 10° from the normal incidence that it was installed. By doing this, the mismatch between the two center wavelengths was reduced within 0.5nm. The corresponding measurement error was reduced from 0.0213% to 0.0035% by estimation.

Transmitting fiber:

The change of the fiber loss can be compensated almost perfectly. Yet the fiber bending will induce both the spectrum and the polarization change of the light propagating inside this fiber.

Because some of the components are polarization dependent, the change of the fiber status will induce a system error. To overcome this problem, a recalibration of this SCIIB system is needed after the deployment process.

Beam splitter:

To realize the self-compensation, the splitting ratio of the beam splitter must be very stable, that means strict requirements for the mechanical stability and long-term stability must be satisfied. On the other hand, the splitting ratio of the beam splitter is polarization dependent. Even though a fiber optic depolarizer is connected in this system, the variation of the output signal is still as high as 0.5% when the fiber was bent or flipped.

Narrowband optical filter:

The output of the SCIIB system is very sensitive to the drift of the central wavelength of the narrowband optical filter. The spectrum characteristics of the filter are dependent on the thickness and the refractive index of the multi-layer thin films, which will change with the ambient temperature because of the thermal expansion effect and the temperature dependence of the

refractive index. With current technology, the temperature dependence of the optical filter is about 0.02nm/˚C. The temperature dependence of the SCIIB system due to this factor is about 0.1%/˚C.

Asymmetry between two channels:

The self-compensation of the SCIIB system is based on the symmetry between the two opt-electrical channels. This is achieved by ensuring that the component selection provides equivalent performance in the two channels. Yet, the absolute match between the two channels is impossible. In reality, both the temperature dependence and the long-term drift (ageing) of the components will induce a system error.

Limited dynamic range:

As described in 2.2.1, to avoid the ambiguity problem of the SCIIB system and realize a high sensitivity, the EFPI sensor should be operated in the linear range of a half fringe. Because of this reason, although the pressure (or temperature) sensitivity of the sensor head can be increased by changing the geometrical parameters of then sensor head or the materials for glass tube, at the same time, the dynamic range of pressure (or temperature) will be decreased by the same scale.

Rigorous requirement for the initial air-gap:

To fully utilize the linear range of the SCIIB system, the initial air-gap of the EFPI sensor must be set at an exact value. This makes the sensor fabrication process difficult and time-consuming. Because of the nonlinear character of *SIN* function, each sensor must be calibrated separately. That's also a painful process for large-scale production.

2.2 Improvement on the SCIIB system

To overcome the problems mentioned in last paragraph, numerous research works had been conducted in VTPL. These works are presented in this section.

2.2.1 Temperature compensation of the SCIIB system

The most important environmental disturbance to the measurement system is the temperature fluctuation. Most components, optical or electrical, are temperature dependence. If the temperature character of the whole system is repeatable, then by using a temperature sensor it could be compensated.

In this section, the temperature character of the SCIIB system was studied in detail. Both the theoretical analysis and experiment results are presented.

The setup for temperature experiments is shown in Figure 2.3

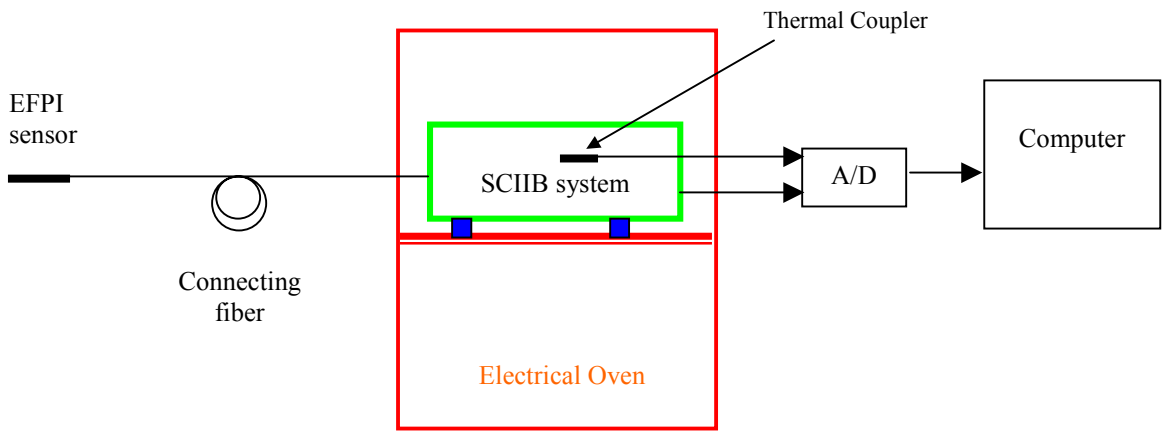

Figure 2.3 The setup for temperature experiments

An resistance heated electrical furnace (Blue M inc. Type 60406) was used in the temperature experiments. The whole SCIIB system, except the EFPI sensor head and connecting fiber, was put inside the furnace. In this way, the temperature dependence of EFPI sensor head and the temperature dependence of the SCIIB system can be studied separately.

Although the electrical furnace itself has a temperature output, to realize a high-resolution measurement, a thermocouple was put inside the electrical box of the SCIIB system. The outputs from the thermocouple and the SCIIB system were sampled by a 22 1/2 bit A/D. A notebook computer was used to store and analyze the experimental results.

The optical spectrum reflected from the end-face of a bare fiber is much different from that reflected from an EFPI sensor. In the case of a bare fiber, the reflected spectrum will be same as the spectrum of light source, which is approximately a Gaussian profile. When connected with an EFPI sensor, an interference reflected spectrum is expected. To get more useful information, the temperature experiments were conducted under two different conditions: in condition one, only a bare fiber was connected with the SCIIB system, and the end-face of the fiber was cut by a cleaver to get a 4% reflection; in condition two, an EFPI sensor was connected with the SCIIB system.

Condition one: (no sensor connected)

The temperature of a recirculating drying oven (with the SCIIB system inside) was increased to about 40˚C. To make sure a uniform temperature distribution inside the whole system was achieved, the oven was kept at 40˚C for about one hour. Then the power was shut off for the oven, and the SCIIB system was allowed to cool down very slowly. Both the output from the SCIIB system and that from the thermocouple were sampled during this period.

To analyze the temperature character of reference channel, the signal transmitting path is shown in Figure 2.4.

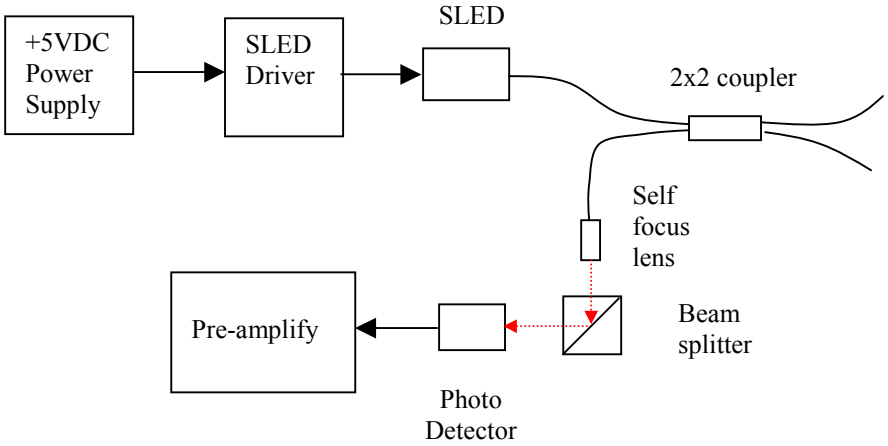

Figure 2.4 The signal transmitting path in the reference channel

The temperature dependence of each components is described as follow:

a. +5V power supply:

A +5V regulated power source (AAK Corporation) was used in the SCIIB system as the power supply for both the amplifier and the SLED driver. The temperature coefficient of this product is about 0.015% per ˚C. Because both the SLED driver and amplifier have a large compliance voltage range, the temperature dependence of the power supply can be neglect.

b. SLED driver:

A PLD-200 laser diode driver (Wavelength Electronics Inc.) was used to supply a very stable current for the light source. The temperature coefficient of the driver is about 0.01% per ˚C. The drift of the output power of light source can be eliminated when the ratio of two channels is calculated.

c. Light source:

The light source used in the single-mode fiber-based SCIIB system is a high power superluminescent light emitting diode (SLED) provided by Anritsu Corp. (AS3B281FX), with the central wavelength of 1312 nm, the spectral width of 41.5 nm, and the maximum output power of 1.21mW from a 9/125μm pigtailed single-mode fiber. Figure 2.5 shows the source spectrum measured by an Ando Optical Spectrum Analyzer (OSA).

The central wavelength of the light will shift when the temperature changes. In general, the temperature induced central wavelength drift is about 0.2-0.3nm per ˚C. Obviously, the spectrum change will induce errors in the interferometric-based measurement system, this will be discussed in later part. To increase the stability of the whole system, a TEC was used to control the temperature of LD.

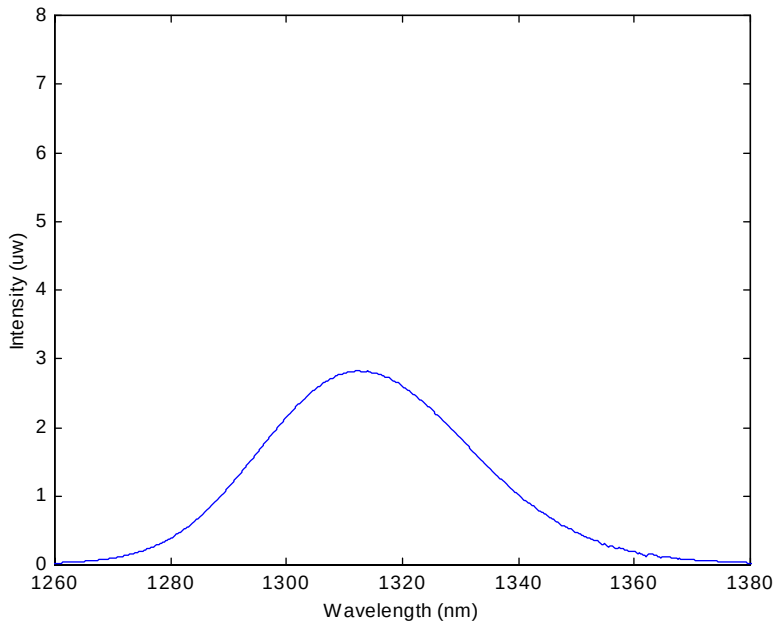

Figure 2.5 The spectrum of the SLED

d. Optical alignment:

The received light signal will be collimated by a self-focus lens, pass through a beam splitter and then be coupled into a TO-packaged large area photo detector. All optical components are installed inside a small aluminum box. The total length from the

self-focus lens to the active area of the photo detector is about 20mm. When the temperature changes, the status of alignment will change slightly, which will induce errors in the measurement results. It's difficult to predict how the status of the alignment changes with temperature, or if the self-calibration can work or not. All these had to be decided according to the experimental results.

e. Photo Detector:

The single mode SCIIB system works at 1300nm. A large effective area InGaAs photo-detector was used to provide a high response in this spectral range. Again, both the dark current and the responsivitty of the InGaAs detector are functions of temperature. The compensating technique works only when two channels have exactly the same temperature dependence, which is almost impossible in reality.

f. Pre-amplify:

The electronics for the pre-amplifier are very simple: a trans-impedance amplifier was employed to convert the photocurrent from the photo detector to a voltage output. The schematic of the circuit is shown in Figure 2.6.

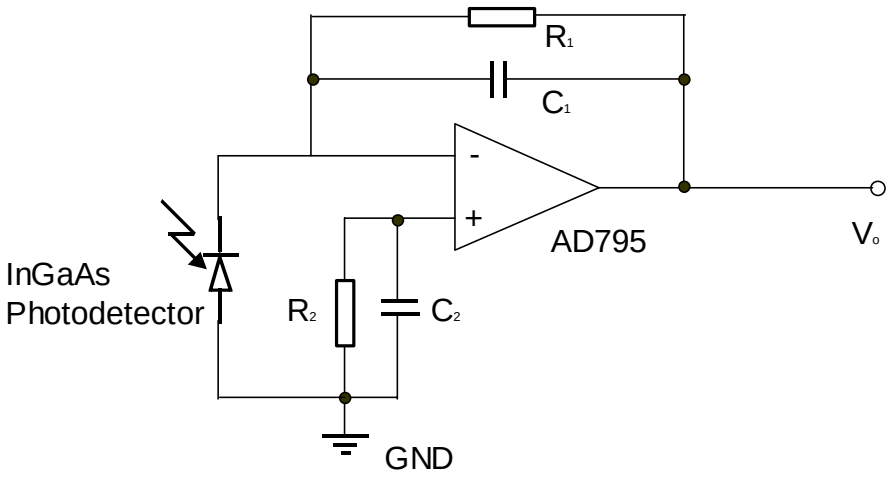

Figure 2.6 The schematics of the pre-amplify

The stability of this amplifier is mainly decided by the feedback resistor R1 and the operational amplifier AD795.

The feedback resistor is type MK lead precision power resistor (CADDOCK). Its temperature coefficient is about 0.008% /˚C.

The AD795 is a low noise, precision, FET input operational amplifier. It offers both the low voltage noise and low offset drift of a bipolar input op amp and the very low bias current of a FET-input device. The 10^{14}(Ohm) common-mode impedance insures that the input bias current is essentially independent of common-mode voltage and supply voltage variations.

The experimental results of the temperature dependence of the broadband channel, the narrow band channel and the ratio R are shown in Figure 2.7—Figure 2.9.

From Figure 2.7 and Figure 2.8, both the reference channel and the signal channel have large temperature dependence (in the temperature range of 26-30 ˚C, the drift is about 0.5%/˚C), which can't be explained by the temperature character of a separate component (most of them is in the order of 0.01%/˚C). This maybe induced by the change of the optical alignment.

The curves in Figure 2.7 and Figure 2.8 are similar, which means part of the temperature dependence can be eliminated by calculating the ratio of two channels. Figure 2.9 shows a mono-decrease relationship between the ratio R and temperature.

The temperature dependence of the ratio R comes from the asymmetry between two channels. The most important difference between the signal channel and the reference channel is the narrowband optical filter used in the signal channel. Other differences include: different photo detector, different amplify, and different optical path. The error induced by the optical filter is dependent on the spectrum of the receiving light signal, while the errors induced by other factors are insensitive to the spectrum. According to the experimental results described later, the temperature dependence of the SCIIB system is mainly comes from the optical filter.

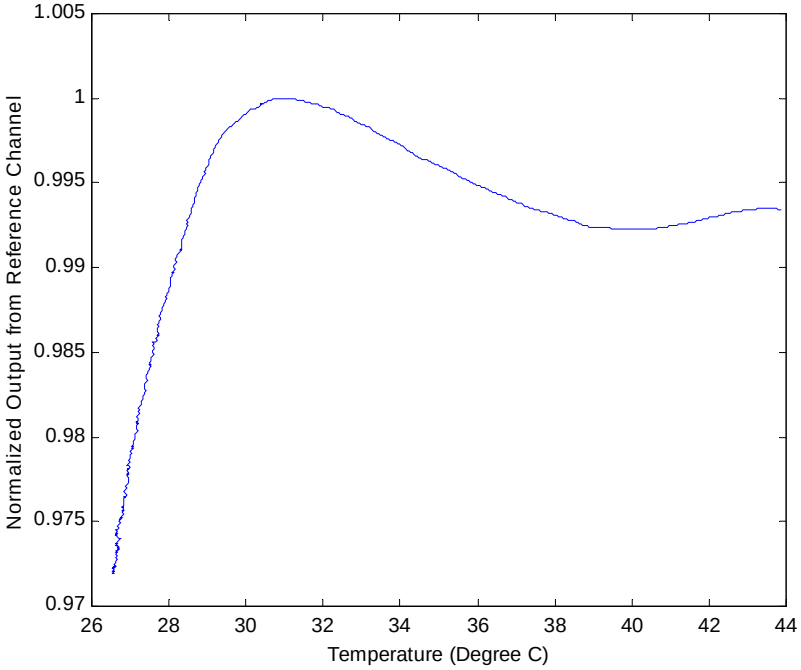

Figure 2.7 The temperature dependence of the reference channel

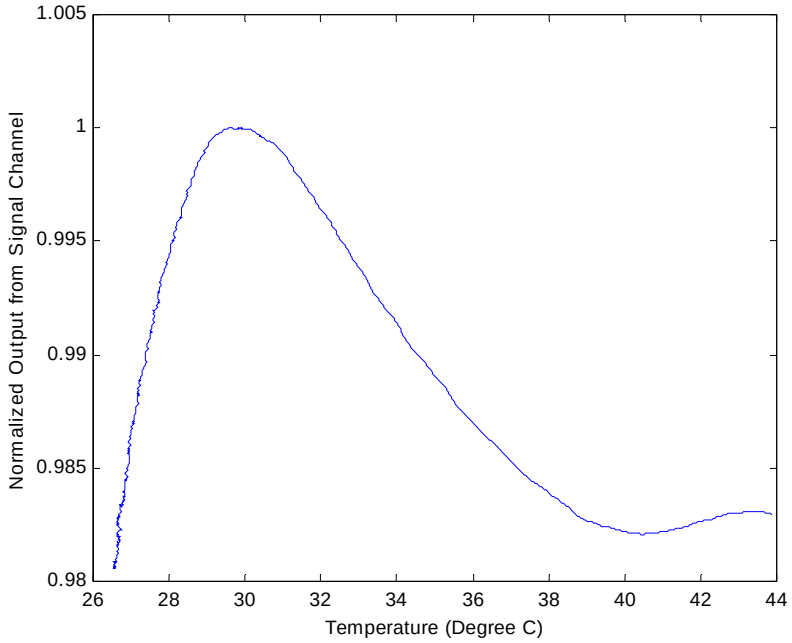

Figure 2.8 The temperature dependence of the signal channel

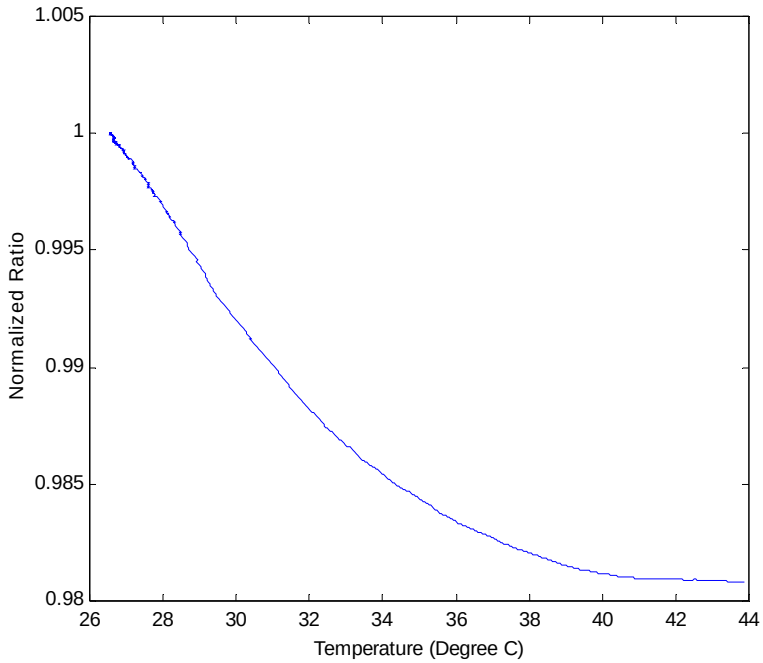

Figure 2.9 The temperature dependence of the Ratio (Signal channel / Reference channel)

As discussed above, the temperature dependence of the SCIIB system includes two parts: the first part is spectrum dependent; the second part is insensitive to the spectrum. The second part can be eliminated easily by using an optical switch in the system.

Figure 2.10 shows the experimental setup of optical switch.

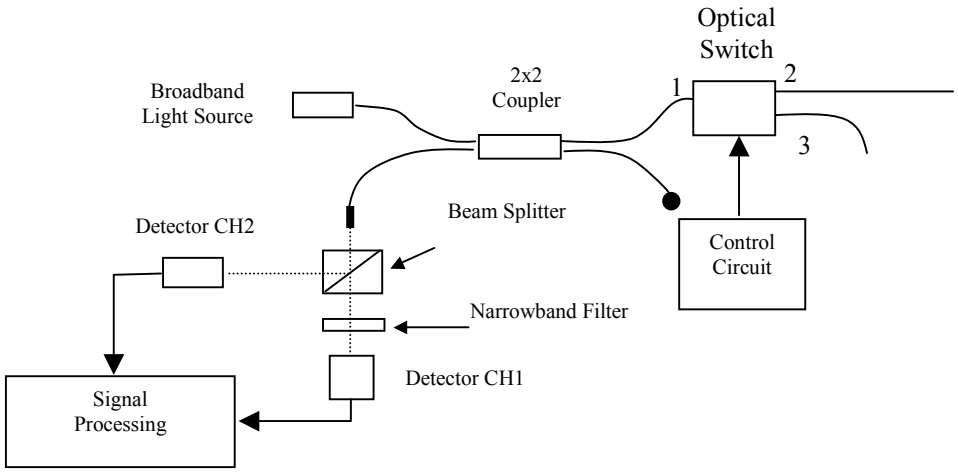

Figure 2.10 The experimental setup for optical switch

A 1x2 optical switch (Lightech fiber optics Inc.) was used in this experiment. The purpose of the introduction of an optical switch into the system is to eliminate errors induced by the asymmetry between channel one and channel two. For those light spectrum-insensitive components, like the photo detector (the band width of the light source is only 60nm, in this range, the response of the detector can be treated as a constant), amplifier, etc, this method works well. Yet, for those light spectrum sensitive components, like the optical narrowband filter, this method is almost no use.

In the first experiment, no EFPI sensor head was connected in the system. Both the port2 and the port3 of the optical switch are connected with a standard 4% reflector (a polished fiber end-face). Because the spectrums of the reflected light signals from these two fiber end-faces are identical (same as the spectrum of the light source), so all the errors induced by the asymmetry can be seen as light spectrum insensitive.

Under the control of a PC, the optical switch alternatively switches between two statues: 1⇔ 2 or 1⇔ 3. The experimental processes are described as follow:

The optical switch was first set at position one S12, the received signal in channel one is

$$I_{s1} = K_1 L_1 I_{01}$$

Where I01 is the output power from the light source at the time when the data is sampled; L1 includes the effect of the reflector and the fiber loss; K1 includes the effect of the optical alignment loss, the photo detector and the amplify in the channel one.

Similarly, the received signal in channel two can be described as:

$$I_{s2} = K_2 L_1 I_{01}$$

So, the ratio R1 in the situation is:

$$R_1 = \frac{I_{s1}}{I_{s2}} = \frac{K_1}{K_2}$$

If the two channels in the SCIIB system are matched perfectly, then K1=K2, R1=1, that means the ratio will not change with temperature. Yet, from the experimental results described above, this requirement can't be satisfied.

The optical switch was then set at position two S13, the two received signals and the ratio are:

$$I_{R1} = K_1 L_2 I_{02}$$

$$I_{R2} = K_2 L_2 I_{02}$$

$$R_2 = \frac{I_{R1}}{I_{R2}} = \frac{K_1}{K_2}$$

Obviously, to eliminate the error induced by the asymmetry between K1 and K2, what is needed is to calculate the ratio of R1 and R1: R=R1/R2

The experiment results of the optical switch were shown in Figure 2.11. The curves of R1 and R2 match with each other almost perfectly, and the final ratio R is almost no change, and therefore, insensitive to temperature. So by introducing an optical switch into the SCIIB system, part of the temperature dependence can be eliminated.

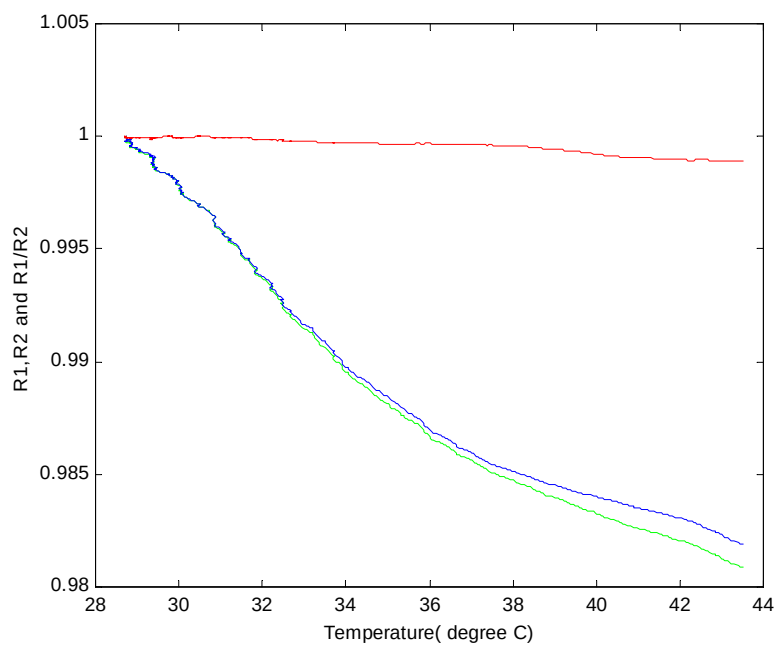

Figure 2.11 The experimental results of the optical switch
(Green line—R1; Blue line—R2; Red line—R)

Condition two: (with sensor connected)

The optical switch works well when no sensors are connected with the system, yet when the SCIIB system is connected with an EFPI sensor head, the situation is much different. The critical component is the narrowband optical filter. Because the light spectrum reflected from an EFPI sensor is much different from that reflected from a reflector, the errors induced by the optical filter will be different at these two conditions. It's difficult to use the signal from the fiber end-face to compensate the signal from a sensor head.

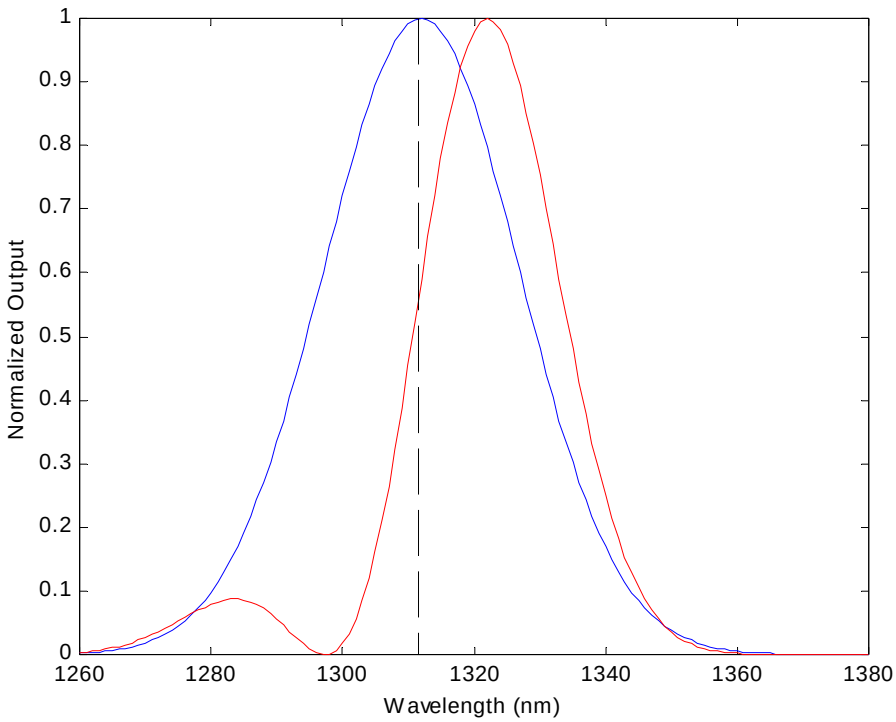

Figure 2.12 the light spectrum reflected from an EFPI sensor (Red line, the initial air-gap of the sensor head is 12000nm) and that from a polished fiber end-face (Blue line)

Figure 2.12 shows the normalized spectrum from an EFPI sensor from a polished fiber end-face. The dashed black line in the curve shows the working point of the SCIIB system (the ideal central wavelength of the optical filter). When temperature increases, the central wavelength of the optical filter will move to longer wavelengths due to the thermal expansion. These two curves

describe how the output of the SCIIB system changes when the central wavelength of the optical filter drifts. Because the slopes of the two curves are much different near the working point, the induced output errors are also much different.

In fact, if the central wavelengths of the optical filter and the light source are matched perfectly, the slope of the Gaussian function near the working point is almost zero, which means only slight errors is produced when a fiber end-face is used as the reflector. In another hand, when an EFPI sensor is connected in the system, the slope of the received spectrum near the working point is very large, and the slope will change with the air-gap (or the physical parameter to be measured). The maximum error induced by the wavelength drifting of the optical filter can be described as:

$$\frac{\delta s_{\max}}{\Delta s_{\max}} = \frac{\gamma \frac{4\pi L}{\lambda^2} \delta\lambda}{1.6\gamma} = \frac{4\pi L}{1.6\lambda^2} \delta\lambda$$

In general, the air-gap L is about 10000nm, the wavelength is about 1300nm, the temperature dependence of the optical filter is about 0.02nm/˚C. So, the error induced by the drift of the optical filter is about 0.1%/˚C.

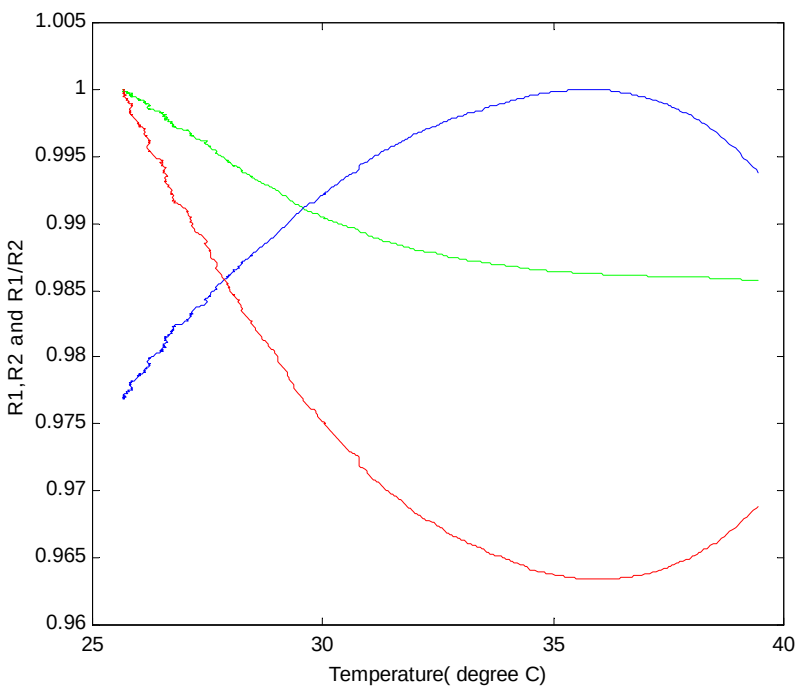

Figure 2.13 Experimental results of the EFPI sensor
(Green line—Sensor Path R1; Blue line—Reference Path R2; Red line—R=R1/R2)

Figure 2.13 shows the experimental results when an EFPI sensor head was connected in the system. In this case, the temperature character of the sensor path (optical switch was in position one, the SCIIB system was connected with an EFPI sensor) is different from that of the reference path (optical switch was in position two, the SCIIB system was connected with a polished fiber end-face.) The use of an optical switch makes the temperature dependence even worse.

To decrease the temperature dependence of the SCIIB system, another approach is using a standard temperature sensor to measure the temperature inside the SCIIB system (especially the temperature of the optical filter).

Without losing the universality, the output of SCIIB system can be simplified as:

$$R = \tfrac{1}{2}(1 + \cos(\frac{4\pi L(P)}{\lambda(T)}))$$

Here an EFPI pressure sensor head was used (L (P)), and the central wavelength of the optical filter λ(T) is a function of temperature.

Differentiating the above equation; the change of R can be expressed as:

$$\begin{aligned}\Delta R &= -\frac{4\pi}{\lambda}\sin\frac{4\pi L}{\lambda}\Delta L(P) + \frac{4\pi L}{\lambda^2}\sin\frac{4\pi L}{\lambda}\Delta\lambda(T)\\ &= K_1(P)\Delta L(P) + K_2(P)\Delta\lambda(T)\end{aligned}$$

Where

$$K_1(P) = -\frac{4\pi}{\lambda}\sin\frac{4\pi L}{\lambda}$$
$$K_2(P) = \frac{4\pi L}{\lambda^2}\sin\frac{4\pi L}{\lambda}$$

This first item on the right side gives out the pressure sensitivity of the SCIIB system; the second item shows how the system output drifts with the temperature.

Comparing with the central wavelength itself, the wavelength drift of the optical filter is very small, so λ can be treated as a constant. Both K1 and K2 are functions of air-gap L (the pressure to be measured), and that means when the pressure changes, the relationship between R and T also changes. This makes the compensation of the ratio R becoming complicated.

The form of the equation can be changed into:

$$\Delta R = K_1(\Delta L - \frac{L}{\lambda}\Delta\lambda)$$

$$\Delta P <=> \Delta L <=> \frac{\Delta R}{K_1} <=> -\frac{L}{\lambda}\Delta\lambda$$

Compare with L (10000nm), the change ΔL (about 200nm) is pretty small, the L/λ can be considered as a constant, so ΔL (or ΔP) is linearly dependent on Δλ (ΔT). Instead of compensating R with T, we can compensate pressure P with T directly.

A thermal resistor was put inside the SCIIB system just aside the optical filter, then the whole system was put inside the electrical oven. An EFPI sensor outside the oven was connected with the system through 1km of single mode fiber. The temperature of the oven first was increased to about 40°C, and then decreased to room temperature (about 25°C). Figure 2.14 shows the outputs of the SCIIB system and the thermal resistor changed with time during this period.

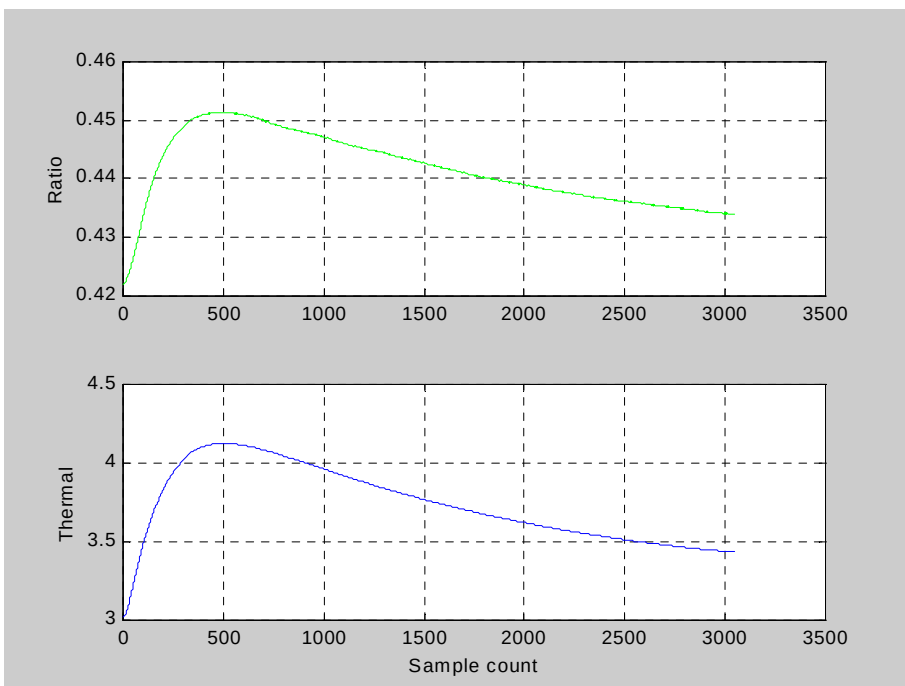

Figure 2.14 Temperature experiment of the SCIIB system (The X axis is time; The unit of the output from thermal resistor is Volts)

From Figure 2.14, The relationship of ratio R and temperature T (here, we use the voltage output of thermal resistor directly) can be worked out, as shown in Figure 2.15.

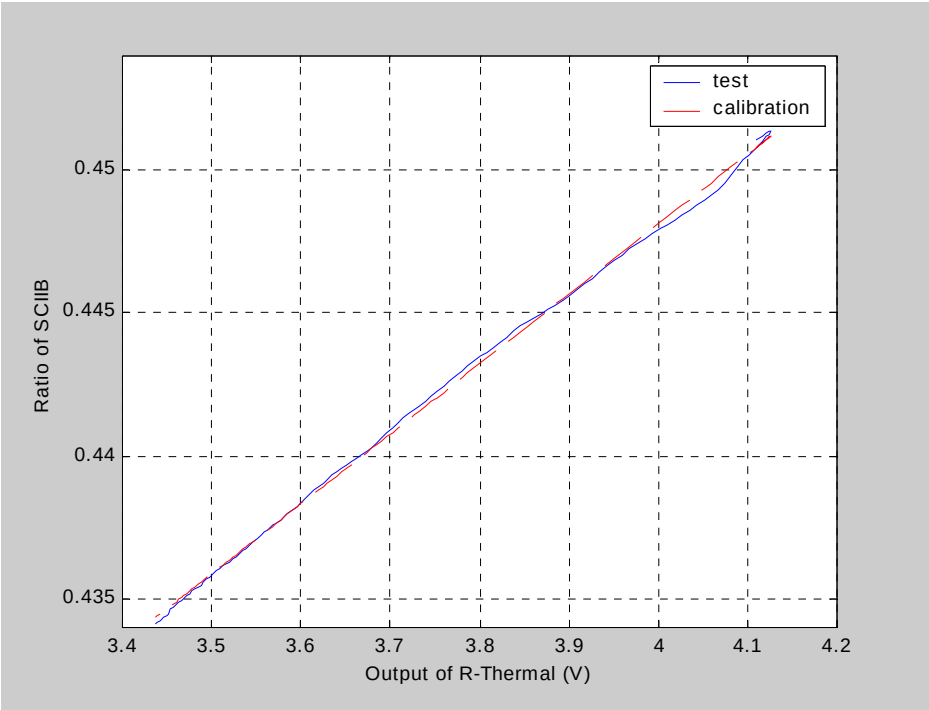

Figure 2.15 Temperature dependence of the ratio R

To setup the relation between ΔP and ΔT(ΔV), the calibrating curve of the sensor head must be acquired first, as shown in Figure 2.16

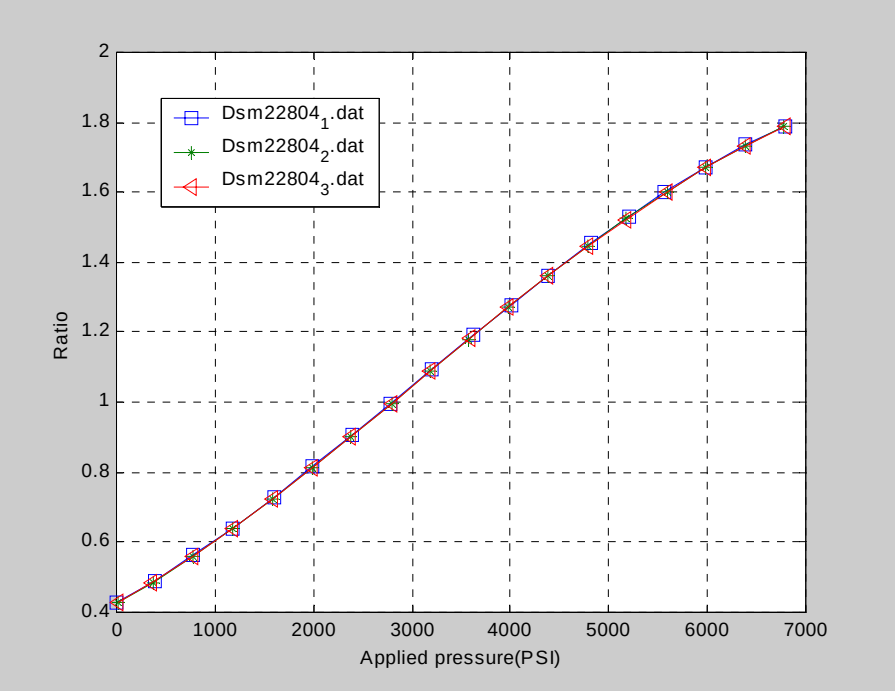

Figure 2.16 Calibration curve of the sensor head

The temperature coefficient of the SCIIB system is then be expressed as $\frac{\Delta P}{\Delta V} = \frac{\Delta P}{\Delta R}\frac{\Delta R}{\Delta V}$.

≈Based on the method discussed above, several sensors were tested. Yet, the residual errors are still greater than the requirements. The one-day-stability level achieved is only about 0.1%. The residual errors come from several sources: the characters of some components will drift with time (ageing process); the spectrum and the status of polarization changes induced by fiber bending, etc.

2.2.2 Other proposed signal demodulating structures:

While numerous works were conducted to improve the performance of the SCIIB system, other signal demodulating structures were also proposed, which include white light interferometer and dual-sensor structure.

One of the major problems of the SCIIB system is the limited dynamic range, which is only about 200-300nm. If the specification for accuracy is 0.01%, then the accuracy of air-gap measurement needs to be 0.01nm, which is about one tenth of the size of an atom.

Another problem of the SCIIB system is associated with the performance of the optical components. Most of them are sensitive to the spectrum or the status of polarization. The spectrum or polarization change induced by a long single mode fiber is difficult to control.

One possible solution for these problems is show in Figure 2.17

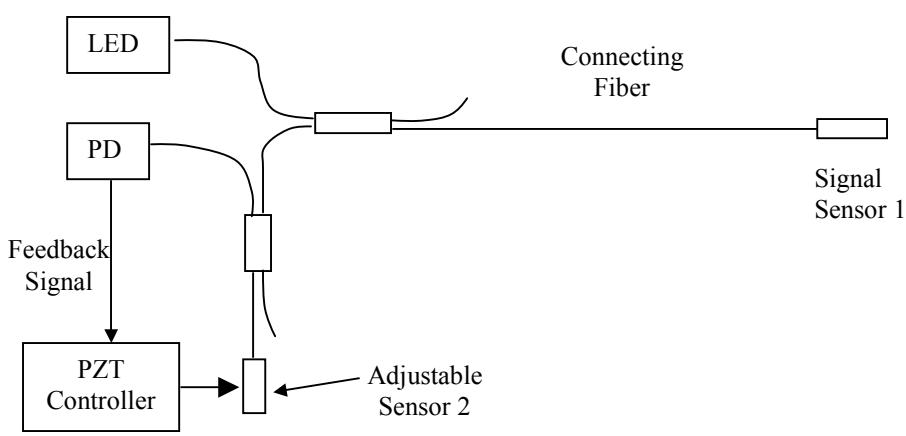

Figure 2.17 One proposed design of dual-sensor structure

Two EFPI sensors are used in this system; the signal sensor is a normal EFPI sensor, which is used to measure the pressure (or temperature) in oil site. Another sensor, which is located in the electrical box, is used to trace the air-gap of the signal sensor. The air-gap of the inside sensor is controlled and measured by a commercialized PZT control system. The photo diode was used to measure the interference between sensor1 and sensor2. To get a maximum output from PD, the two air-gaps must be equal.

When the air-gap of the signal sensor changes, the output of PD will decrease. Using the feedback signal from PD, the PZT controller will adjust the air-gap of the sensor2 till it matches with sensor1. The air-gap of sensor2 at the balance point will be measured by the PZT controller.

Obviously, in this system, the dynamic range of the air-gap is decided by the PZT system. When the air-gaps of two sensors are matched with each other, the signal received by PD is always a global maximum. A commercialized PZT system can reach 1nm repeatability with tens of μm dynamic range, so the potential accuracy of this system is better than 0.01%.

Other advantages of this structure include: insensitive to the change of polarization and light spectrum, easy to realize multiplexing, etc.

Positive preliminary results had been obtained with this structure. However, due the enormous successes achieved in the white light system, attentions were focused on that area.

3. Signal demodulation system II-white light interferometer

Parallel with the development of the SCIIB system, another interferometric based fiber optic sensor system, the white light interferometer, was also built at VTPL. The initial intent of developing such a system was to monitor the air-gap of the EFPI sensor during sensor fabrication. (The working point of the SCIIB system is decided by the initial air-gap of the EFPI sensor head. To acquire the maximum dynamic range and sensitivity, the deviation of air-gap from the optimum point should be less than 10nm). During this process, several important progresses had been achieved by thoroughly studying on the white light system. By combining elaborate hardware design with a novel data processing methods, the system reaches a sub-nm resolution with a 10 μm dynamic range. The white light system had been proved to be the best choice for high-resolution, low speed application. In this chapter, the detailed work will be presented and the research work of the next step is also discussed.

3.1 Basic configurations and operating theory

White light or low coherence interferometer is a technique which dates back to 1913 and was reapplied to optical fiber sensing in 1983.

In most of the conventional interferometric systems, to get a large coherent length, high coherent light sources (like single line lasers) are used. For such a narrowband light source, spectrum measurements are impossible, only power measurement can be realized. For this kind of system, a tradeoff is needed between the absolute measurement and the large dynamic range. To achieve absolute measurement, the change of the optical length must be limited in half of the wavelength, just like in the SCIIB system. Or using an interference counting method, the potential dynamic range can be as large as the coherent length of the light source, yet only the relative change of the optical path can be measured. When a long length of optical fiber is involved, the instability induced by the propagation of the highly coherent light in the optical fiber also becomes a big issue.

To realize both the absolute measurement and high resolution, the white light interferometer was developed. Instead of the highly coherent laser, a broadband light source, such as LED, is used in this system (that's where the terminology "white light" comes from, and in this sense, the SCIIB system also belongs to the white light system family). Although the power detection still can be used, to fully exert the advantages of the white light source, spectrometer-based detecting systems are more popular.

The white light interferometic fiber optic sensor system inherits most of the advantages from conventional interferometer, such as immune to the drift of light source and the change of transmitting loss, high resolution, large dynamic range, etc. In another hand, the use of a long life, low price broadband light source (such as LED) improves the stability of the whole system dramatically.

The basic structure of spectrometer-based white light system is shown in Figure 3.1. Similar to the SCIIB system, an EFPI sensor head was used to measure pressure or temperature. The broadband light source used is an 850nm LED with a 60nm bandwidth. This kind of light source contains a lot of virtues, such as high stability, long life, high efficiency, small size, low price, etc. A compact spectrometer fabricated by Ocean Optics Inc was used to measure the interference spectrum. The whole system is very concise and robust.

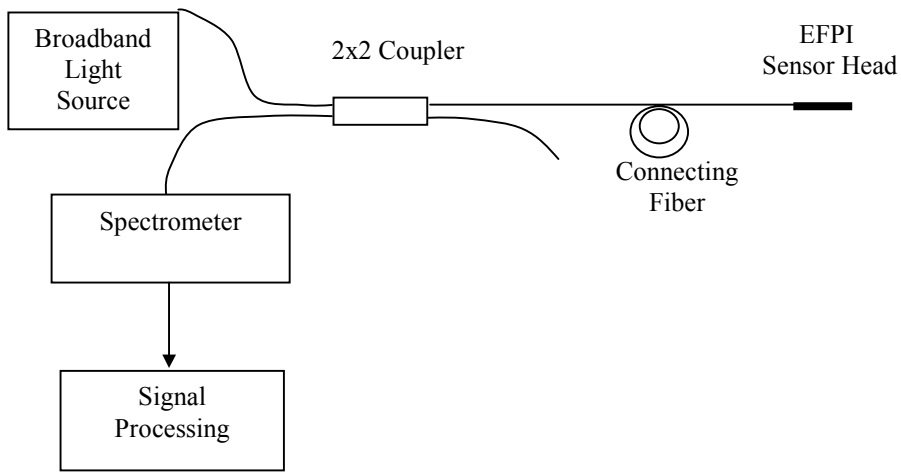

Figure 3.1 The basic structure of interferometer-based white light system

Through a 2x2 fiber coupler, the optical power output from the light source is launched into the connecting fiber and propagates to the EFPI sensor head. The light signal reflected from the sensor head travels back along the same fiber and launch out to the one dimension CCD based interferometer from the other port of the 2x2 coupler. Then, the measured spectrum is transferred to PC for date processing.

To get an interference spectrum with high visibility, the air-gap can't be over above the coherent length of system. In this system, the coherent length is mainly dependent on the spectral resolution of the spectrometer, the Numerical Aperture (NA) of the optic fiber and the quality of the EFPI sensor head. In general, the coherent length in white light system is larger than that of SCIIB system.

The interference spectrum measured by the spectrometer is given by:

$$I(\lambda) = 2I_s(\lambda) \bullet (1 + \gamma \cos(\frac{4\pi G}{\lambda} + \varphi_0)) \qquad (3\text{-}1)$$

Where $I_s(\lambda)$ is the spectral power distribution of light source, γ is the visibility of interference spectrum, φ_0 is the arbitrary initial phase difference, G is the air-gap, which is determined by the physical parameter (such as pressure or temperature) to be measured.

Normalized equation (3-1) respect to the Guassian spectrum of light source, the normalized interference output can be expressed as

$$I_n(\lambda) = 2(1 + \gamma \cos(\frac{4\pi G}{\lambda} + \varphi_0)) \quad . \qquad (3\text{-}2)$$

The value of air-gap G can be calculated out from equation (3-2) and then be used to demodulate the physical parameter.

3.2 Novel data processing method

Various methods had been developed to demodulate air-gap G from the normalized spectrum using equation (3-2). Most of these kinds of arithmetic can be cataloged into two classes. The first class can achieve high resolution (which mainly depends on the resolution of spectrometer), but the dynamic range of the air-gap must be limited in the half wavelength range; the second class can achieve a large dynamic range, yet only a low resolution acquired. The basic ideas for these methods are discussed as follow:

Class One:

The first type is based on tracing a special point in the interference spectrum (such as peak point or valley point). Then from the wavelength of this special point, the value of air-gap can be demodulated.

In the method of Peak tracing: the wavelength λm of a peak point in interference spectrum satisfies

$$\frac{4\pi G}{\lambda_m} + \varphi_0 = m2\pi \tag{3-3}$$

Where the spectral order m is a non-negative integer.

Equation (3-3) can be transformed into:

$$\begin{aligned} G &= \frac{(m2\pi - \varphi_0)\lambda_m}{4\pi} = \frac{K_m}{2}\lambda_m \\ K_m &= \frac{(2m\pi - \varphi_0)}{4\pi} = m - \frac{\varphi_0}{2\pi} \end{aligned} \tag{3-4}$$

To demodulate the air-gap G from a special peak wavelength λm, Km must be acquired first. The identification of the interference order m is so difficult that the unambiguous operating range of the air-gap is limited in only half of the wavelength.

The resolution of measuring result is mainly dependent on the resolution of spectrometer. From equation (3-4), the relative error of this system can be described as

$$\left|\frac{\Delta G}{G}\right| \cong \left|\frac{\Delta\lambda}{\lambda}\right| \tag{3-5}$$

Class Two:

To realize absolute measurement, at least two special points in the interference spectrum need to be used. In fact, there are 2048 pixels in the CCD detector of spectrometer, 1000 of them locate in the spectrum range of the light source, the more information are used, the higher resolution could be achieved.

Suppose λ1 and λ2 (λ1>λ2) are the wavelengths of two adjacent peak points in the interference spectrum. Their interference orders are m and m+1.

From equation (3-3):

$$\frac{4\pi G}{\lambda_1} + \varphi_0 = m2\pi$$

$$\frac{4\pi G}{\lambda_2} + \varphi_0 = (m+1)2\pi$$

The air-gap G can be demodulated from:

$$G = \frac{\lambda_1 \cdot \lambda_2}{2(\lambda_2 - \lambda_1)} \qquad (3\text{-}6)$$

Here, the dynamic range is only limited by the coherent of the white light system.

In this case, the relative error induced by the spectrometer is

$$\left|\frac{\Delta G}{G}\right| \cong \sqrt{2}\left|\frac{\lambda_2}{\lambda_2 - \lambda_1}\right| \bullet \left|\frac{\Delta\lambda_1}{\lambda_1}\right| \qquad (3\text{-}7)$$

Compare with equation (3-5), in *Class Two*, the relative error induced by the spectrometer will be enlarged by a factor of $\sqrt{2}\left|\frac{\lambda_2}{\lambda_2 - \lambda_1}\right|$.

The central wavelength of the light source (LED) is 850nm. In the normal operating range (air-gap 5-15 μm), this factor $\sqrt{2}\left|\frac{\lambda_2}{\lambda_2 - \lambda_1}\right|$ is about 15—50. So, this method has a large dynamic range but lower resolution.

New Algorithym:

To combine the advantages of these two kinds of methods together, a novel data processing method was developed in VTPL, which can realize both the high resolution and a large dynamic range.

The basic idea of this method is: use two peak points in the interference spectrum to get a roughly air-gap (large dynamic range is achieved); this roughly air gap was used to determine the order number m and a roughly K_m of a special peak point. Then, an accurate K_m will be recovered from the roughly K_m. From equation (3-4), the accurate air gap can be calculated out from the accurate K_m and the peak wavelength (high resolution is achieved).

The constant K_m of a special peak is calculated from the roughly air-gap, if this K_m is used directly, high resolution can't be achieved. The technique to recover the accurate K_m is discussed here:

In equation $G=K_m\lambda/2$. Although K_m is not an integer, for a given peak, it is a constant. And for adjacent peaks, the difference in K_m is 1. For example, if the K_m of one peak is 12.34, then, for other peaks, the K_m will be 13.34, 14.34, 15.34…and 11.34, 10.34, 9.34…

By calibration, the K_m value for a special peak (K_m^0) can be acquired and stored in computer. When the roughly K_m value for any peak had been acquired, the accurate K_m will be calculated out from K_m^0 by adding the integer part in the difference between the roughly K_m and K_m^0.

The whole process of demodulating air-gap G from the interference spectrum can be separated into two steps: the calibrating process and the measuring process.

The calibrating process is described as follow:

With the white light interferometer system in a stable condition, set the air-gap G to a known value G0 (or put the EFPI sensor head in a given pressure environment). The K_m^0 of a peak in the interference spectrum can be calculated from G_0 and the wavelength λ_0 of this peak.

As long as the K_m^0 is acquired, the measuring process can be carried out as follow:

1. Use two peak points in the interference spectrum to acquire a roughly value of air-gap G';
2. Select a peak point near the center of interference spectrum, use the wavelength of this peak and the roughly G' from last step to calculate a roughly K_m'
3. The accurate K_m can be calculated from K_m' and the stored K_m^0 from:

$$K_m = K_m^0 + \mathrm{int}(K_m^{'} - K_m^0 + 0.5)$$

Where function int(…) means to get the integral part.

4. The accurate air-gap G can be calculated from the accurate K_m and the wavelength of this peak by equation (3-4).

If the white system works in a harsh environment, occasionally, the outside disturbance can introduce a big "jump" in the measuring result. The magnitudes of these "jumps" are equal to half

of the wavelength exactly. These "jumps" in the measured output due to the inability of the spectral analyzer to resolve adjacent K_m values.

As described in the discussion above, the low-resolution G' value is used to determine the low-resolution K_m' value. In the determination of the low-resolution K_m' value an error can occur due to the inaccuracies in the G' value. If the error in the low-resolution K_m' value is large enough this will result in shifting the K_m value by an integer number. This shifting of the K_m value by an integer number results in a calculated change in the air gap of an integer multiple of one half of the wavelength of the light source. When monitoring a physical parameter such as pressure, the observed result is that the pressure detected from the sensor appears to "jump" to a higher or lower value when indeed the real pressure has not changed. This "jump" can occur at any time during the operation of the system and appears in a more or less random fashion.

In order to overcome the "jump" problem, another data processing method was used to monitor the value of air-gap calculated from the previous time interval. The new value of air-gap *Gn* calculated during the present time interval is compared to the air-gap value *Go* from the previous time interval

$$\Delta G = \left| G_n - G_o \right|$$

If the Δ G value is larger than one half of the wavelength of the light source used, then, the air-gap will be modified according:

$$G = G_n - \frac{\lambda}{2} \qquad \text{When } Gn > Go$$

$$G = G_n + \frac{\lambda}{2} \qquad \text{When } Gn < Go$$

Therefore, when the condition is detected such that *Gn* is larger or smaller than *Go* by more than one half of the wavelength, a new air-gap G is calculated based on the formulas above. This new air-gap G is then used to demodulate the physical parameter to be measured. The system checks for this condition during every measurement. In this manner, the jump problem has been completely eliminated.

This novel data processing method had been realized on Visual Basic, and had been applied in the oil field. Its performance was approved by the experimental results.

3.3 Design and implementation

Both the single mode and multi mode white light systems had been setup in VTPL. A VB program, integrated functions of system control and date processing, also had been developed. The details works on the system setup and program development are presented in this section.

3.3.1 Hardware design and system fabrication

The critical part of white light system is the spectrometer. The performance of the whole system, such as resolution and stability, are highly depended on the performance of spectrometer. In traditional spectrometer based system where a cumbersome and expensive spectrometer was used, the strict requirements to environmental conditions exclude the possibility to use this kind of instrument in field site. Here, a compact fiber optic spectrometer (USB2000 manufactured by Ocean Optics, Inc,) was used in the white light system.

The input fiber was connected with USB2000 directly through a SMA connector. Inside the spectrometer, a 1200 line holographic grating was used to diffract the input light on a 2048 pixels CCD array. The electrical signals output from each pixel will be read out serially. Converted into digital format by a built-in A/D card, the measured spectrum can be transferred into a PC. The interface between the computer and the spectrometer is very flexible; Ocean Optics supports most of the common ports, including USB, ISA, etc.

The Key Features of the USB2000 are listed as follow:

Computer interface:	Universal Serial Bus (RS-232 available on side connector)
Spectrometer channels:	One or two
Integration time:	3 milliseconds-65 seconds
Data transfer rate:	Full scans (2048 wavelengths) into memory every 13 milliseconds
	OOIBase32 time acquisition approximately every 25 milliseconds
Dimensions:	3.5" x 2.5"x 1.31" LWH
	89 mm x 64 mm x 34 mm LWH
Weight:	0.45 lb. without cable
	0.60 lb. with cable
	200 grams without cable
Detector:	2048-element linear silicon CCD array
Effective range:	200-1100 nm
Dynamic range:	2×10^8
Sensitivity (estimate):	86 photons/count;
Signal-to-noise:	250:1 (at full signal)

Dark noise:	2.5-4.0 (RMS)
Gratings:	Multiple grating choices, optimized for UV, VIS or NIR
Slits:	optical fiber is entrance aperture
Focal length:	42 mm (input); 68 mm (output)
Resolution:	~ 0.3 nm-10.0 nm FWHM
Stray light:	< 0.05% at 600 nm; < 0.10% at 435 nm; <0.10% at 250 nm
Fiber optic connector:	SMA 905 to single-strand optical fiber (0.22 NA)

Both signal mode and multimode white light systems were built up based on USB2000 spectrometer. In multimode system, the light source is an 850nm LED (Honeywell HEF 4857-014). In the single mode system, a super-luminescent diode (SLED from EG&G inc.) was used. To satisfy the requirements of different applications, two channels multimode system was also developed.

Figure 3.2a and b shows the structure of single channel multimode white light system. The two channel multimode white light system is shown in Figure 3.3.

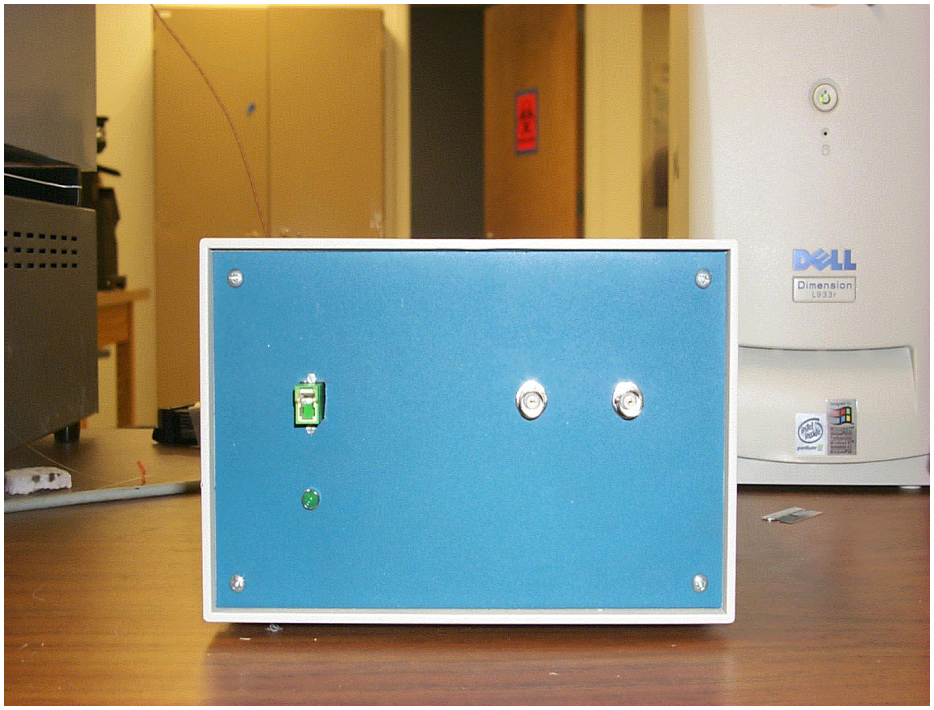

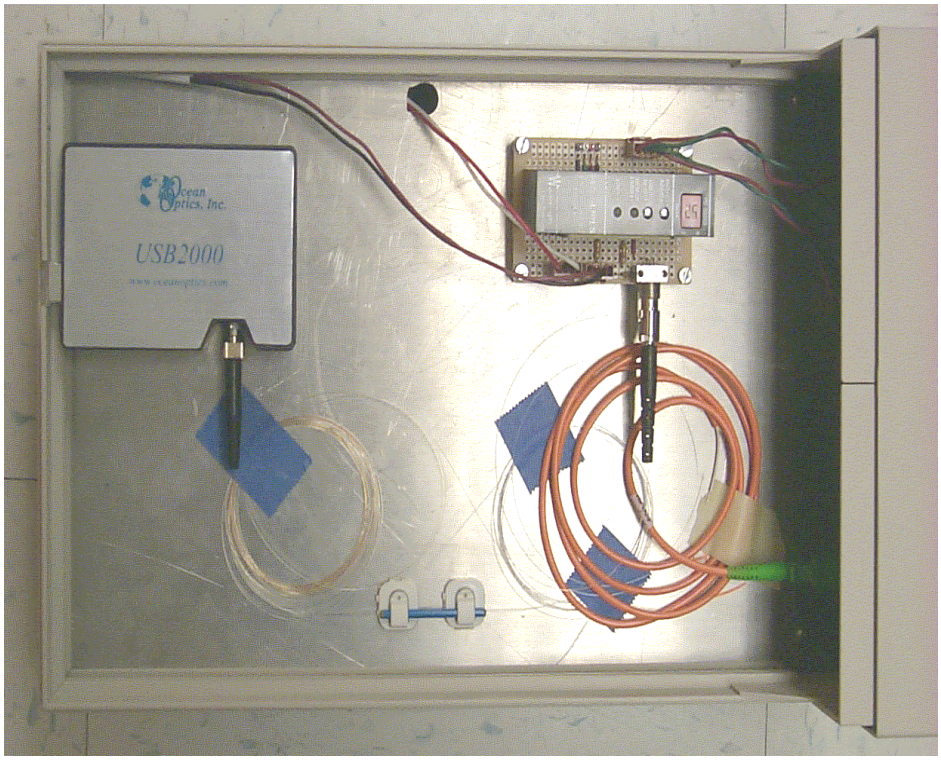

Figure 3.2 a-b the single channel multimode white light system

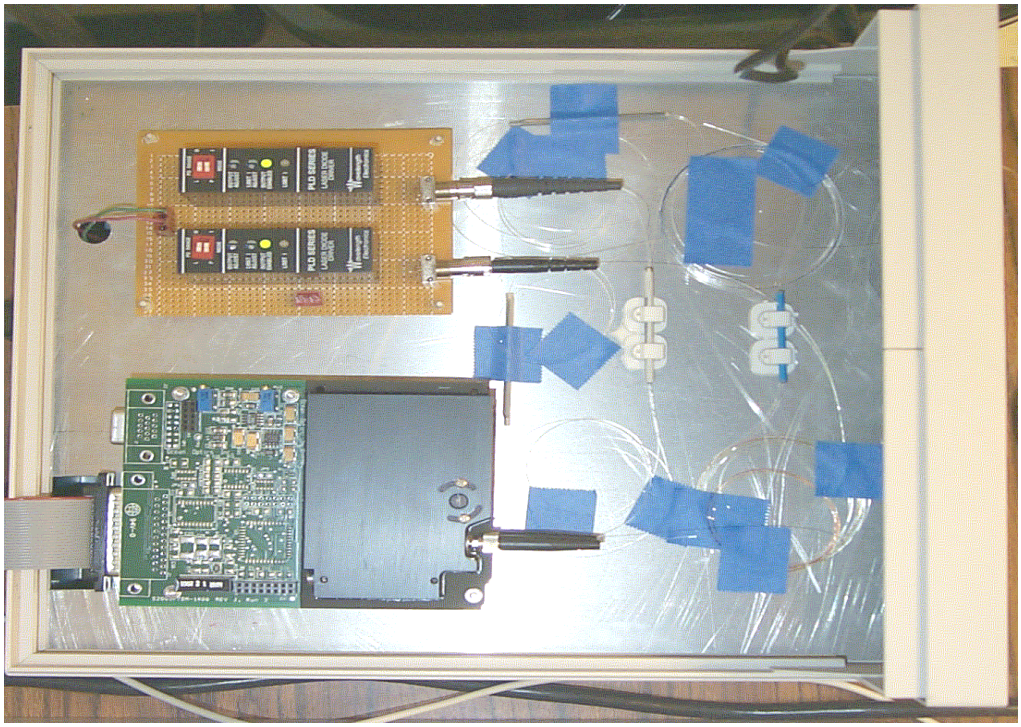

Figure 3.3 the two channel multimode white light system

3.3.2 Software design and program development

Advanced computer software was developed to demodulate the air-gap from the interference spectral signal. This program is based on the novel data processing method discussed previously . The program is implemented in the combination of Visual Basic and C languages so that both graphic interfaces and high computational speed are achieved and optimized. The block diagram of the program is shown in Figure 3.4.

The program is described in details as follow:

Initialization

The program starts with the hardware initialization, which include the initialization of the spectrometer, temperature measurement system (for compensation), etc. Then most of the important parameters, which were stored in the hard disc, will be restored in the memory. These data include the parameters for setting up spectrometer, the K_0 value, the reference spectrum of the light source, the dark current of the spectrometer, the calibration curve of the EFPI sensor head etc.

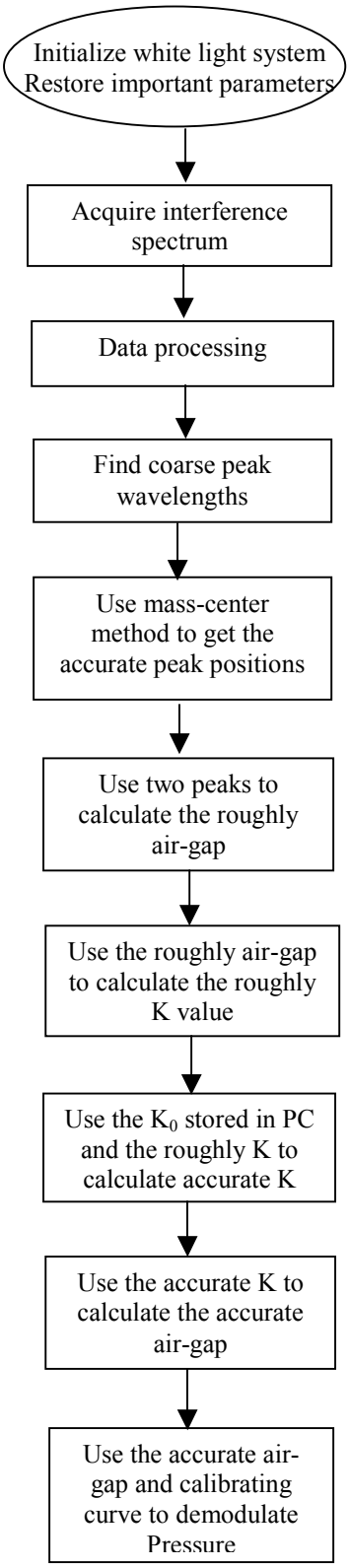

Figure 3.4 Block diagram of the program

Spectrum measurement

The interference spectrum from the EFPI sensor head will be sampled according to the given time interval. Once the received light signal comes out from optical fiber, it will be coupled into the spectrometer through a SMA connector. Once in the spectrometer, the divergent light emerged from the optical fiber will be collimated by a spherical mirror. Then, a plane grating is employed to diffract the collimated light. A second spherical mirror then focuses the resulting diffracted light and an image of the spectrum is projected onto a 1-dimensional 2048 pixels linear CCD array. These reverse-biased photodiodes discharge a capacitor at a rate proportional to the photon flux. When the integration period of the detector is complete, a series of switches closes and transfers the charge of each pixel to a shift register. After the transfer to the shift register is complete, the switches open and the capacitors attached to the photodiodes are recharged and a new integration period begins. At the same time as light energy is being integrated, the spectrum data is read out of the shift register by a built-in A/D card. At last, the spectral data will be sent to PC through an USB port.

Data processing

To demodulate pressure (or temperature) signal from the interference spectrum accurately, an advanced data processing algorithm was developed and realized based on Visual Basic. This part is the core of the whole program, and will be discussed in several sub-steps:

Pre-processing

The original spectrum data from the spectrometer is a 1x2048 array, which composes the received light signals of the 2048 pixels of CCD detector. To recover the interference spectrum, the calibrating curve of CCD was used to calculate the real wavelength from the serial number of array. To remove the dark current noise of the CCD detector and other background noises, a dark spectrum stored in the PC was deducted from the measured spectrum. The dark spectrum was acquired when the light source was power off. Figure 3.5 shows the spectrum in this step.

Smooth and Normalization

From Figure 3.5, there are obvious noises on the received spectrum. To improve the signal-to-noise ratio (SNR), a boxcar algorithm is developed to filter and smooth the raw data. The spectrum after smoothing is shown in Figure 3.6

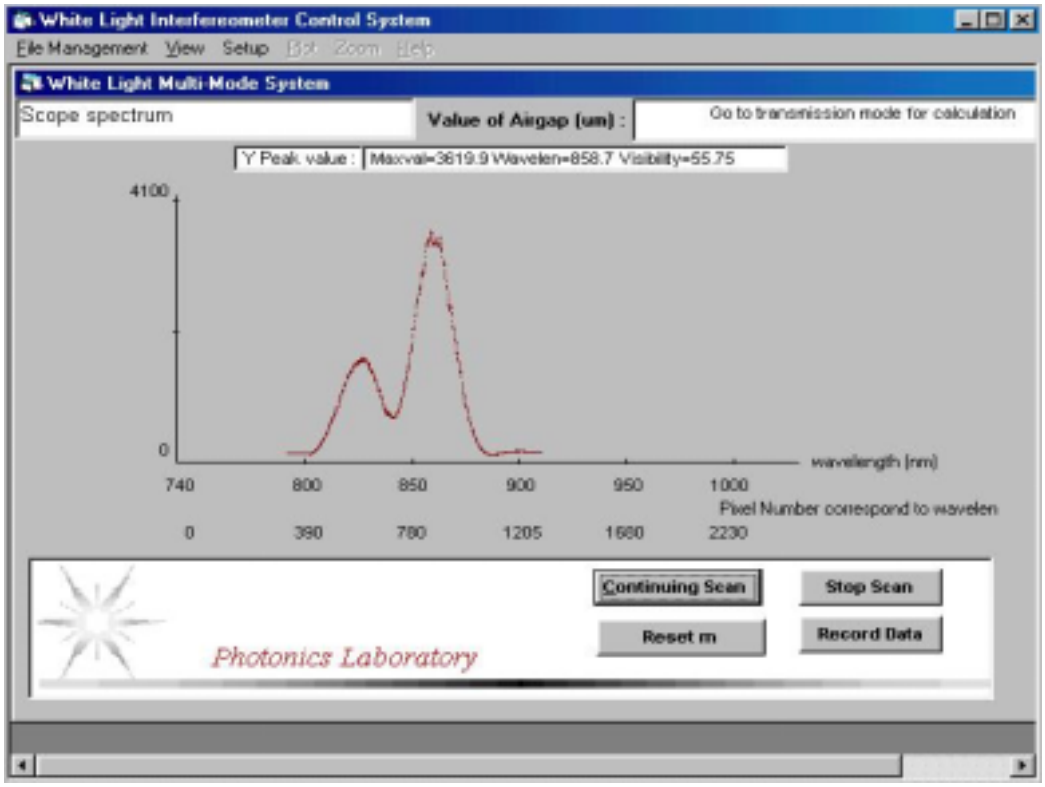

Figure 3.5 The interference spectrum after pre-processing

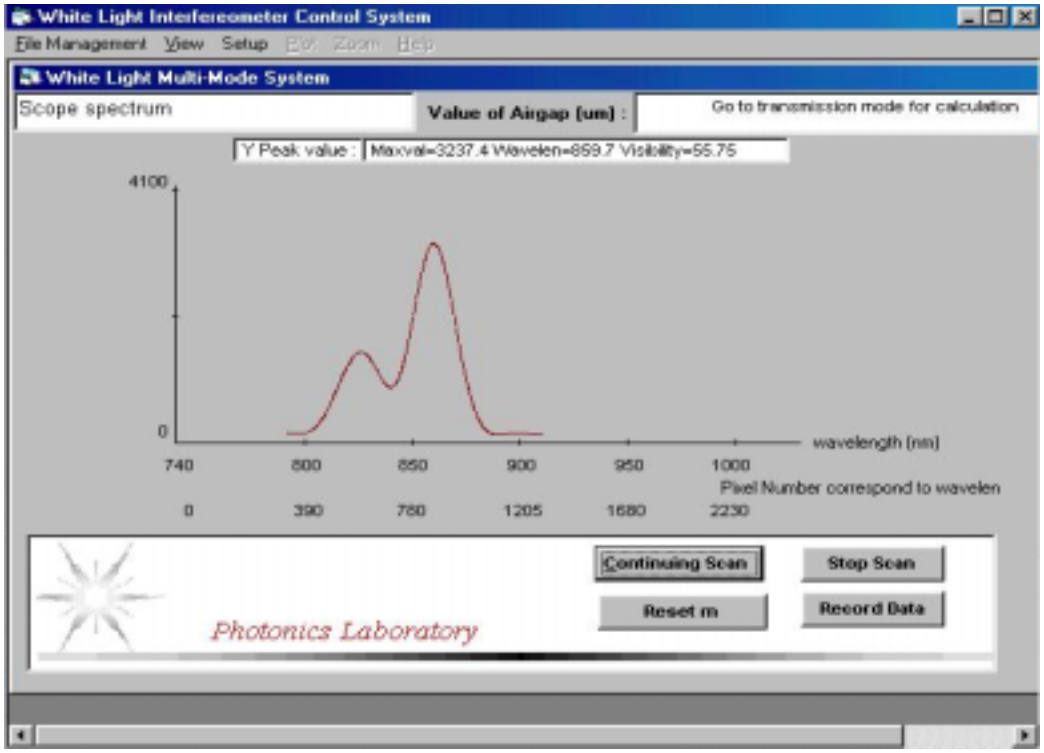

Figure 3.6 The interference after normalization

In Figure 3.6, the interference spectrum is automatically truncated according to its signal level.

This ensures that only the high SNR region of the spectrum is included in the calculations. Then the measured spectrum will be normalized by the Gaussian profile reference spectrum of the light source. The normalized spectrum is shown in Figure 3.7.

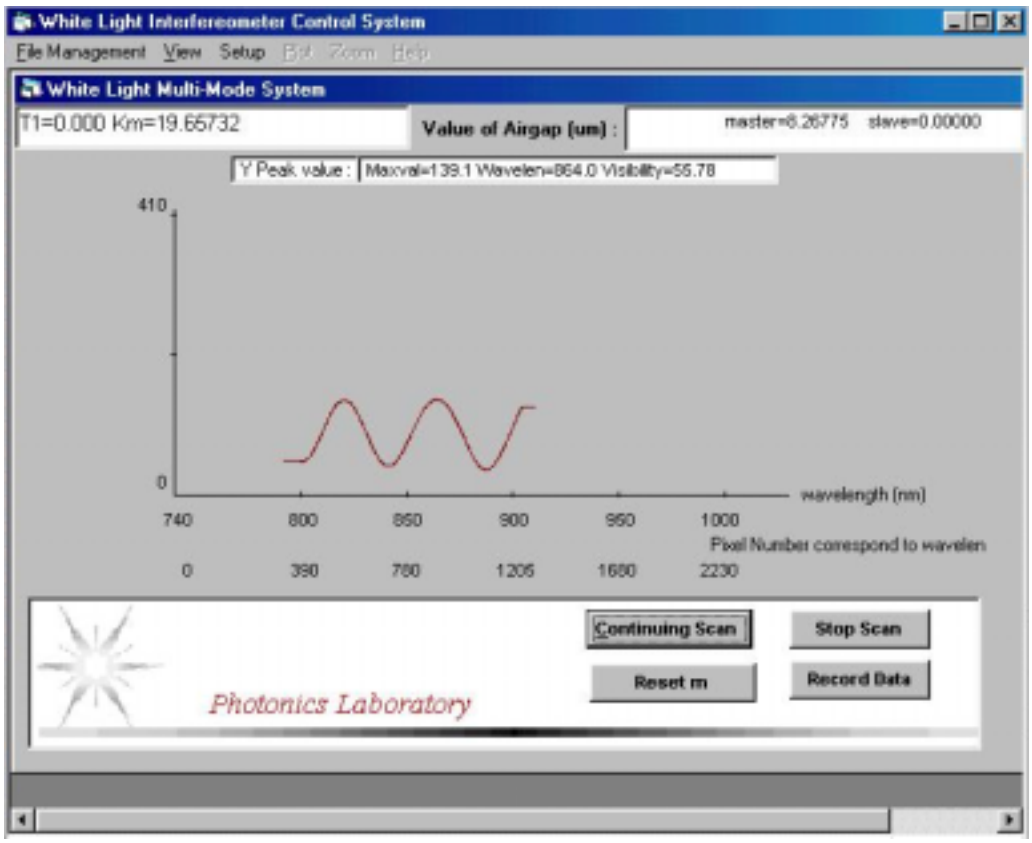

Figure 3.7 Normalized spectrum

One important parameter of the boxcar smoother is the window width, which must be selected very carefully. An unsuitable window width may induce deformation of the interference spectrum. This will be discussed as follow:

Suppose the measured spectrum is {f (i), i=1,2.., 2048}, then the boxcar smoothing process can be described as:

$$f_s(i) = \frac{1}{2w+1} \sum_{j=-w}^{j=w} f(i+j)$$

Where w is the window width.

Obviously, the larger the window width of the filter is, the better the performance can be achieved. On the other hand, a large window width will cause two problems. First, the visibility of the spectrum will decrease when the windows width is increased, that is the character of the average arithmetic. Second, because the interference spectrum isn't a symmetry function of wavelength, the average process will induce the deformation of interference spectrum and shift of peak positions.

Figure 3.8 shows the simulated results for a small window width (w=5; air-gap G=11μm). In this case, no obvious deformation can be observed, and a high visibility was achieved.

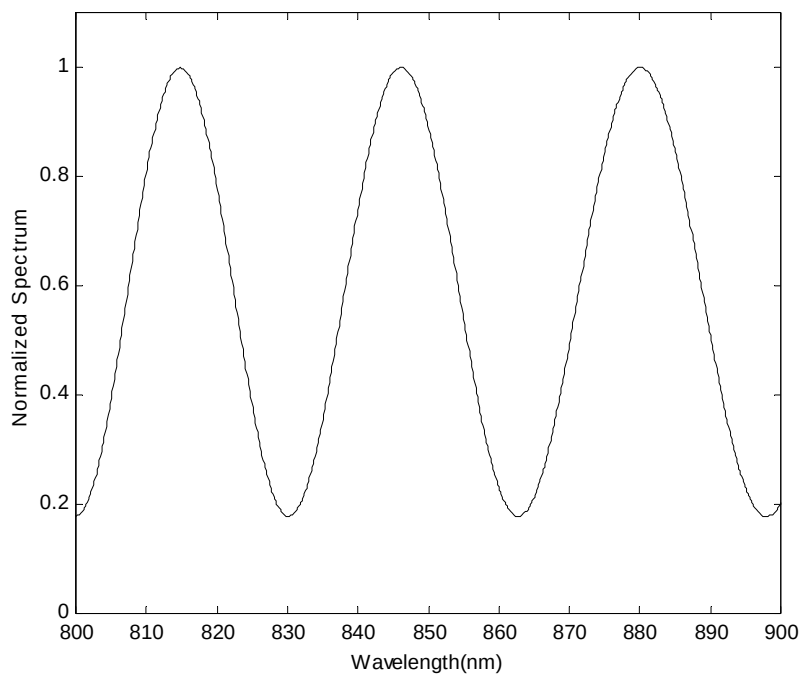

Figure 3.8 Simulated result for small window width (w=5)

As compare, Figure 3.9 shows the simulated result for a large window width (w=80; G=11). The visibility of interference spectrum decreases a lot and obvious deformation can be observed.

Figure 3-10 shows the measured results when a large window width was used. (In this case, w=61), the result is very similar to the simulated results shown in Figure 3-9.

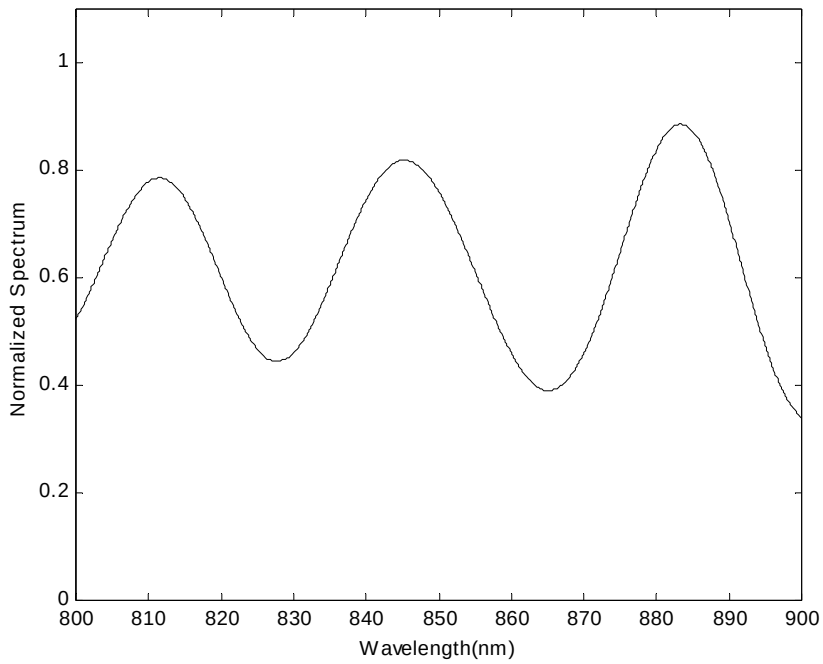

Figure 3.9 Simulated result for large window width (w=80)

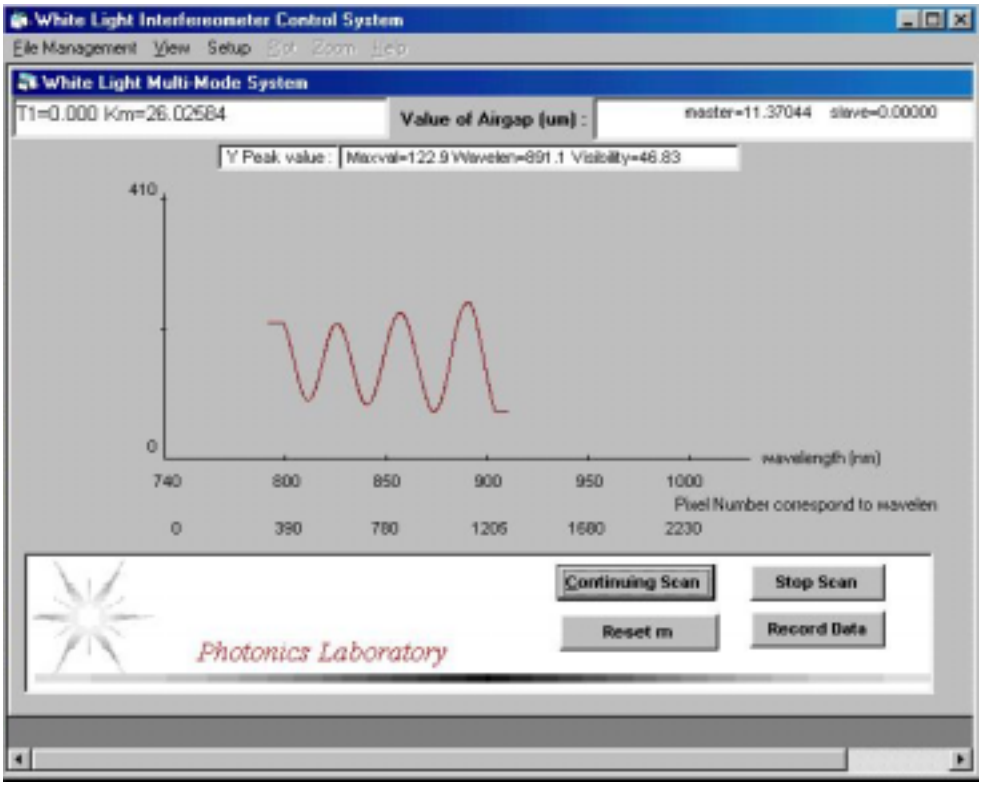

Figure 3.10 Measured result when a large window width was used

To get the best performance and prevent the deformation of the interference spectrum, the window width needs to be optimized according to a different CCD detector, light source and the air-gap of the EFPI sensor. The basic principles are: the more CCD pixels in unit wavelength space, the larger window width can be used; the smaller the air-gap of EFPI sensor (which means the space between adjacent peaks is large), the larger window width can be used.

Peaks location

The demodulation of the air-gap is based on the peak positions in the interference spectrum. The technique for peak location is described as follows:

The first step is to find the coarse locations of the peaks and valleys by a smart comparison algorithm. The basic idea is to find all the local maximum points in a special range in the interference spectrum. The size of the searching range, which is defined as the window size of peak searching, must be large enough to eliminate the influence of noise. In another hand, to avoid missing some peaks, the window size must be smaller than the space between adjacent peaks. An FFT algorithm is used to automatically estimate the optimum window size for peak searching.

After the coarse positions of peaks had been found, a mass-centroid algorithm is applied to find the accurate peak positions.

The basic theory of the mass-centroid algorithm is shown in Figure 3.11. If the function Y (x) is symmetry around its peak position, then the peak position coincides with the x coordinate of the centriod of Y (x).

As shown in Figure 3.11 the peak position Xo can be calculated from:

$$X_0 = \frac{\int xf(x)dx}{\int f(x)dx}$$

From equation $I_n(\lambda) = 2(1+\cos(\frac{4\pi G}{\lambda} + \varphi_0))$, around the peak point, the spectrum is a symmetrical function of k=1/λ. So the spectrum y(λ) need to be changed into k-space first (from $\{y_i, \lambda_i\}$ to $\{y_i, k_i\}$).

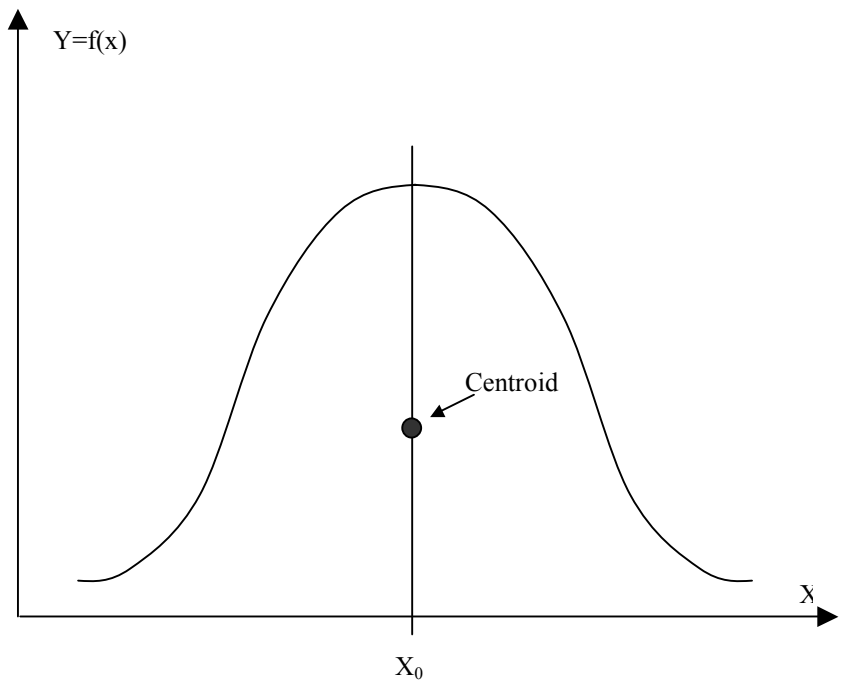

Figure 3.11 The mass-centroid method

Start from the normalized spectrum $\{y_i, k_i\}$, the accurate peak positions can be calculated from the coarse peak positions:

$$k_i = \frac{1}{\lambda_i}$$

$$k_m^p = \frac{\sum y_i k_i (k_i - k_{i-1})}{\sum y_i (k_i - k_{i-1})}$$

$$\lambda_m^p = \frac{1}{k_m^p}$$

Demodulation the measured physical parameter

Once the peak positions are acquired, the physical parameter to be measured can be demodulated:

A coarse air-gap will be calculated out using two peak positions, and then the coarse k value for a special peak will be determined. From the Ko value stored in PC, the accurate k value will be figured out, which in turn is used to calculated the accurate air-gap. The current air-gap will be compared with last air-gap value to judge if a "jump" happened during this process. If it does happen, the measuring results will be modified by a suitable value.

Finally, using the calibrating curve, the pressure (or temperature) will be demodulated from the accurate air-gap.

3.4 The performance of white light system

The multimode white light system had been used as signal demodulation system for pressure, temperature and flow sensors. Detail works will be presented in following chapters. Here, only some common results are discussed.

Large diameter and linearity

The major advantage of the white light system is the large dynamic range. Figure 3.12 shows the testing results of an EFPI temperature sensor.

During this experiment, the signal demodulating system was kept in a stable environment; the EFPI sensor head was put into an electrical oven. While the temperature of electrical oven increased from room temperature to about 200°C, the air-gap of EFPI sensor head increased from 7μm to about 16μm, which gave out a dynamic range of about 9μm. Comparing with the 200nm dynamic range of SCIIB sensors, the dynamic range was increased about 45 times.

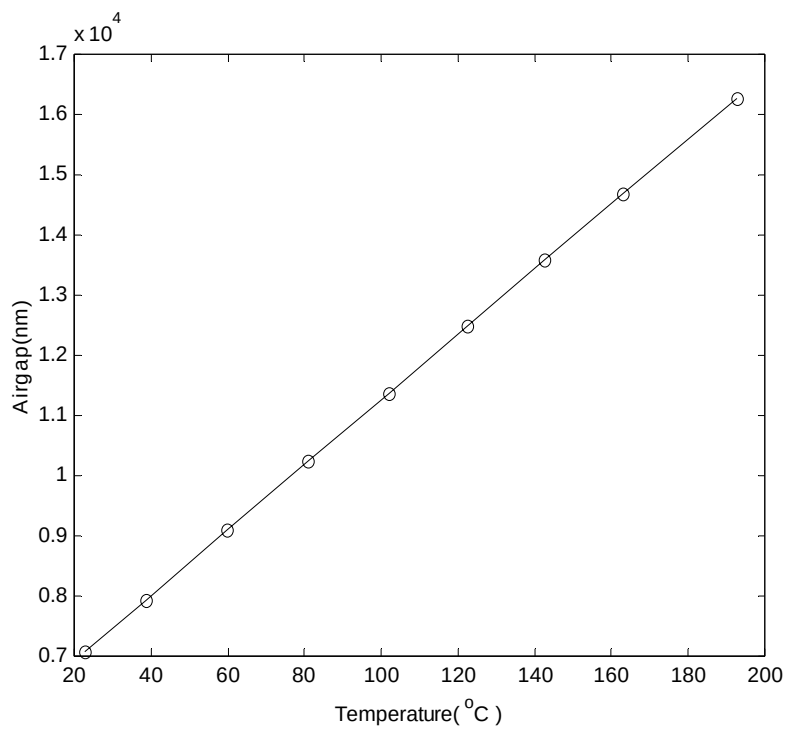

Figure 3.12 The testing result of the EFPI temperature sensor

Figure 3.12 also shows a very good linearity. In fact, as long as the coefficient of thermal expansion (CTE) of the material is a constant, the measuring results will have a linear relationship with the temperature.

High resolution

One character of the interferometric based sensor is the high resolution. Figure 3.13 shows the testing results for a pressure sensor in 30 seconds. The sample rate is about 5 times/second. During this experiment, the whole system (white light and EFPI sensor) was kept in a stable environment (both temperature and pressure).

The resolution of the sensor system is usually interpreted by its standard deviation of a series of air-gap measurements. It is common to use twice the standard deviation as the direct measure of resolution. In Figure 3.13, the standard deviation is about 0.015nm, which gives a resolution of about 0.03nm. This is the utmost resolution of the white light system. In the field application, due to various noise sources (such as temperature fluctuation, mechanical vibration, etc), it's very difficult to reach this limit.

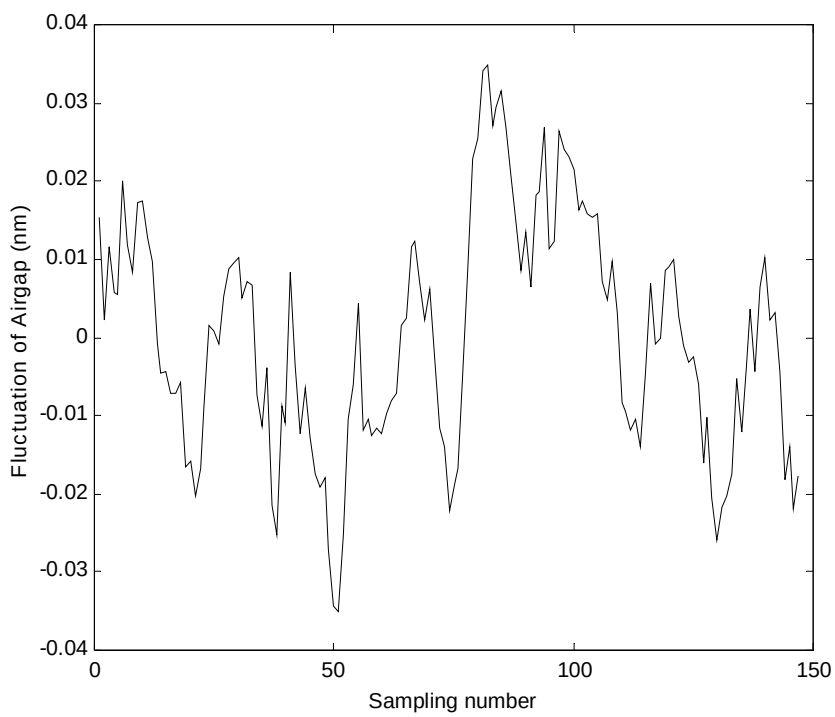

Figure 3.13 Short term fluctuation of the white light system

Temperature character

The temperature dependent of the white light system comes from two sources: LED and the spectrometer. Their contributions will be discussed separately as follow:

LED

Although the spectrum of LED had been measured and stored in PC as reference spectrum, when the ambient conditions change, the spectrum of LED maybe drifts.

Decided by the character of material, the central wavelength of the LED will shift to longer wavelength as temperature increase. Suppose the reference spectrum was acquired at temperature T_0, and the central wavelength at that temperature is λ_0 then, the reference spectrum can be described as:

$$R(\lambda) = I_0 \exp(-\frac{(\lambda - \lambda_0)^2}{w^2})$$

Here *w* is the spectral width of the light source.

When the temperature increased to T, the central wavelength of LED will shift to λ_T. Being no method can be used to acquire the spectrum of LED in real time, the reference spectrum acquired at temperature T_0 will be used to normalize the interference spectrum acquired at temperature T. The normalized spectrum N(λ) calculated in this way can be expressed as:

$$N(\lambda) = \frac{\exp(-\frac{(\lambda - \lambda_T)^2}{w^2})}{\exp(-\frac{(\lambda - \lambda_0)^2}{w^2})}(1 + \gamma \cos(\frac{4\pi G}{\lambda})) \qquad (3\text{-}8)$$

The simulating curve of N(λ) is shown in Figure 3.14. Here the air-gap G is supposed to be 9.2μm, the spectral width *w* is 27nm, visibility of the interference spectrum γ is 0.5, and the shift of central wavelength is supposed to be 5nm. Figure 3.15 shows the measuring result of an EFPI sensor when the temperature was increased to about 45°C(the reference spectrum was acquired at 25°C). The theoretical analysis and the experimental result matched very well.

Obviously, being the use of a reference spectrum acquired at a different temperature, the peak positions in interference spectrum shifted.

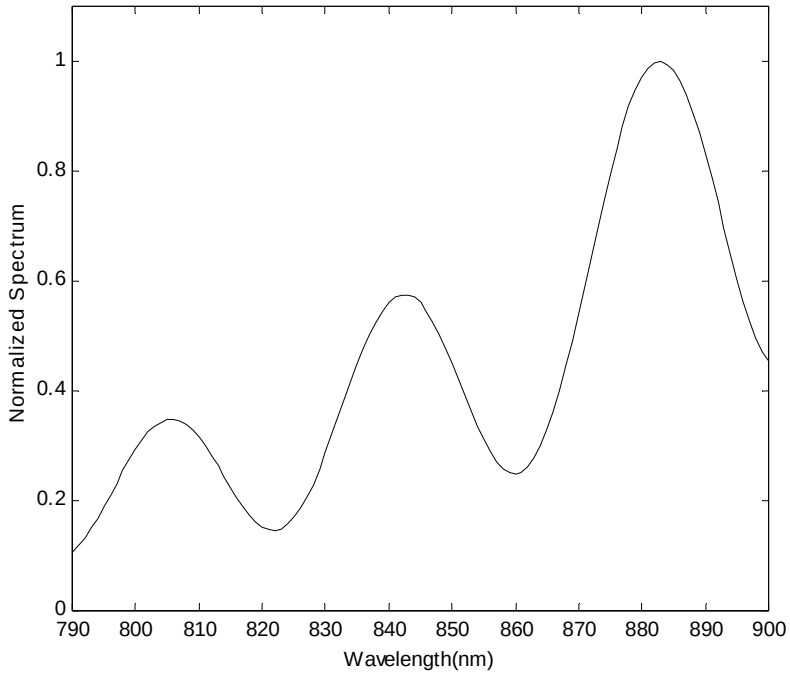

Figure 3.14 Simulated results of the normalized spectrum

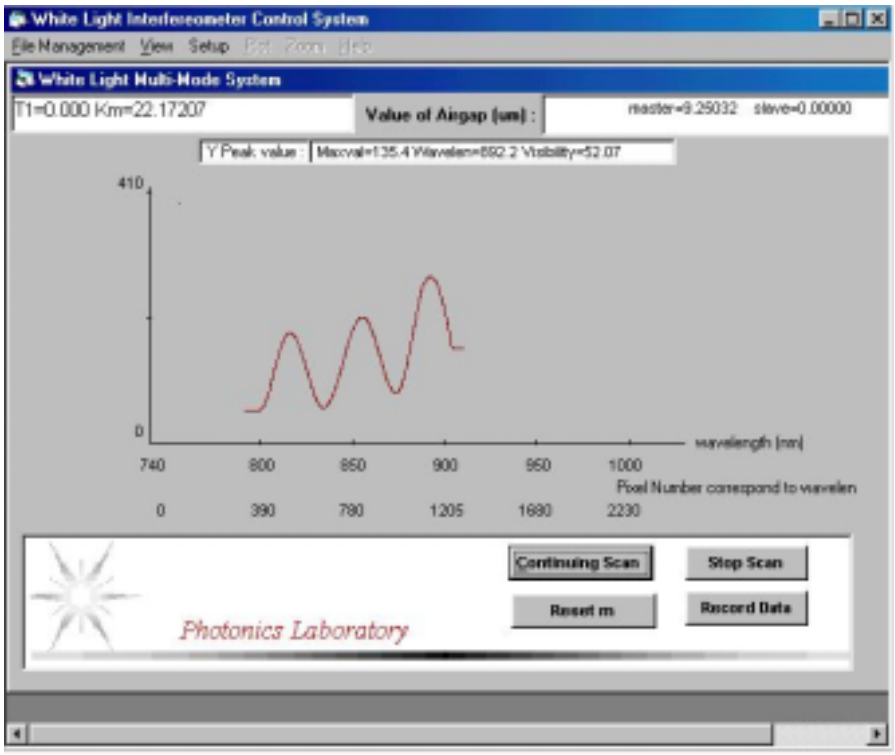

Figure 3.15 Measurement results of the normalized spectrum at 45°C

Suppose the shift of central wavelength of LED is

$$\delta = \lambda_T - \lambda_0 = a\Delta T << \lambda_0$$

Then

$$\frac{\exp(-\frac{(\lambda-\lambda_T)^2}{w^2})}{\exp(-\frac{(\lambda-\lambda_0)^2}{w^2})} \approx (1+\frac{2(\lambda-\lambda_0)}{w^2}\delta)$$

So Equation (3-8) becomes:

$$N(\lambda) = (1+\frac{2(\lambda-\lambda_0)}{w^2}\delta) \bullet (1+\gamma\cos(\frac{4\pi G}{\lambda}))$$

The peak position shift Δλ can be acquired by differentiating last equation.

$$\frac{\partial N}{\partial \lambda} = \frac{2\delta}{w^2} + \frac{4\pi G\gamma}{\lambda^2}\sin\frac{4\pi G}{\lambda} + \frac{2\delta}{w^2}\gamma\cos\frac{4\pi G}{\lambda} + \frac{2(\lambda-\lambda_0)\delta\gamma}{w^2}\cdot\frac{4\pi G}{\lambda^2}\cdot\sin\frac{4\pi G}{\lambda} = 0$$

$$\Delta\lambda = \frac{(1+\gamma)\lambda^4}{8\pi^2\gamma G^2 w^2}\cdot\delta$$

Using G=mλ/2, the error of air-gap ΔG induced by peak position shift Δλ is

$$\Delta G_L = \frac{(1+\gamma)\lambda^3}{8\pi^2\gamma G w^2}\cdot\delta_L = \frac{(1+\gamma)a\lambda^3}{8\pi^2\gamma G w^2}\cdot\Delta T \qquad (3\text{-}9)$$

In general, the temperature coefficient of an LED (a in equation (3-9)) can be treated as a constant, when the air-gap G is a fixed number, the air-gap error induced by the temperature change of the light source is linearly dependent on the temperature change.

The temperature dependence of the light source was measured by experiment. During this experiment, the light source was kept in an electric oven; the spectrometer and other parts were kept in room environment. The temperature of oven was increased to about 50°C, and kept at that temperature for about 2 hours. Then the temperature was decreased to room temperature slowly (in about 3 hours). During the temperature decreasing process, a thermocouple was used to sample the temperature in the oven, and the spectrum of the LED was sampled by the Ocean Optics card.

Figure 3.16 Shows the test results. The temperature coefficient of LED is about 0.27nm/°C.

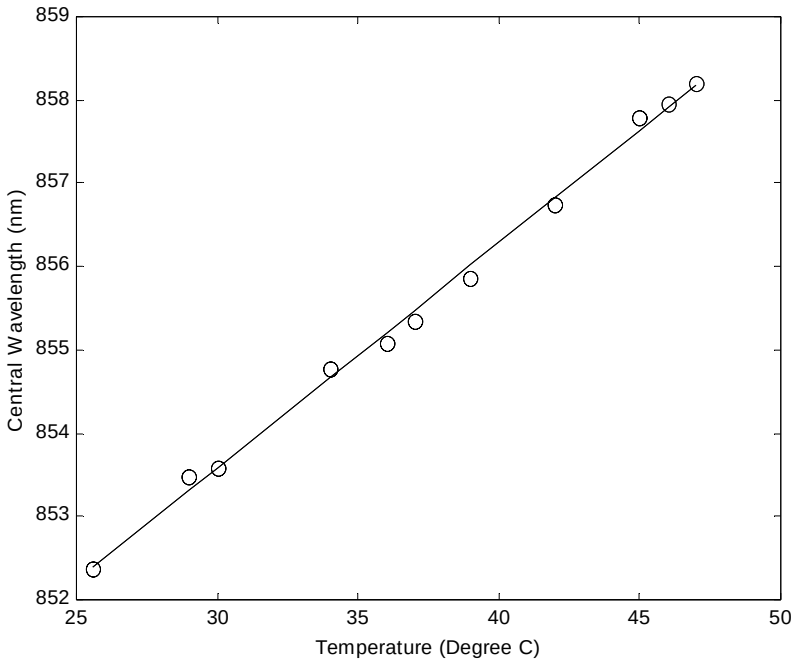

Figure 3.16 Relationship between central wavelength of the LED with temperature

For a regular EFPI sensor (G=10000nm, γ=0.6) the temperature character induced by the shift of LED central wavelength is about 0.77nm//°C.

Spectrometer

Although the spectrometer was setup on a temperature-regulated bench, the residual temperature dependence is still critical for high-resolution measurement.

Suppose the wavelength drift of spectrometer is δ_s. Obviously, the peak positions in the interference spectrum will also shift this amount. On the other hand, similar to LED, the wavelength shift will induce the deformation of normalized spectrum. So the total error of air-gap induced by the spectrometer is:

$$\Delta G_s = (\frac{G}{\lambda} + \frac{(1+\gamma)\lambda^3}{8\pi^2 \gamma G w^2}) \cdot \delta_s = b \cdot (\frac{G}{\lambda} + \frac{(1+\gamma)\lambda^3}{8\pi^2 \gamma G w^2}) \cdot \Delta T$$

The gross temperature dependent of white light system

$$
\begin{aligned}
\Delta G &= \Delta G_L + \Delta G_s \\
&= \frac{(1+\gamma)\lambda^3}{8\pi^2\gamma G w^2}\delta_L + (\frac{G}{\lambda} + \frac{(1+\gamma)\lambda^3}{8\pi^2\gamma G w^2}) \cdot \delta_s \\
&= [a \cdot \frac{(1+\gamma)\lambda^3}{8\pi^2\gamma G w^2} + b \cdot (\frac{G}{\lambda} + \frac{(1+\gamma)\lambda^3}{8\pi^2\gamma G w^2})] \cdot \Delta T
\end{aligned}
\tag{3-10}
$$

From last equation, the temperature coefficient of white light system is a function of air-gap G. That means for EFPI sensors with different air-gap or for the same sensor under different pressure (or temperature), the temperature coefficient of white light system will be different.

To realize temperature compensation, the air-gap dependent temperature coefficient K (G) must be acquired by experiment. As long as K (G) is acquired, the compensating steps are as follow:

First, the roughly air-gap G' (without temperature compensation) is acquired;

Second, use G' to determine K (G): K (G)≈K (G');

Third, Use K (G) and temperature acquired by a thermal coupler to calculate the accurate air-gap G: G=G'+K (G')ΔT

These works will be done in the following month.

Except the performances discussed here, other characters of white light system, such as repeatability, long-term stability, etc, will be discussed with a special sensor.

3.5 Compare between the SCIIB system and the white light system

Both the SCIIB system and the white light system have their advantages and disadvantage. Compare with the white light system, the major advantage of the SCIIB system is the high speed. In the case where the very high frequency response is not an important issue, such as pressure, temperature and flow measurement, the white light system has superiority over the SCIIB system. The main advantages of the white light system over the SCIIB system are discussed as follow:

Large dynamic range

The most important advantage of the white light system is the large dynamic range. Different from the SCIIB system, the operating range of the white light system doesn't have to be limited in a half of the wavelength. In fact, the dynamic range of the white light system is only limited by the coherent length and the structure of the sensor head. By choosing a large gauge length or suitable material, the sensitivity of the sensor head can be increased dramatically.

In the multimode white light system, the lower limit of air-gap is decided by the spectral width of the light source. From the data processing method discussed above, at least two peak points are needed to demodulate the air-gap from the interference spectrum. For the 850nm LED used in the multimode white light system, the effective spectral range (the range in which a high signal noise ration can be realized) is about 80nm, so, the minimum air-gap of the EFPI sensor is about

$$G_{\min} = \frac{\lambda_1 \lambda_2}{2\Delta\lambda} \approx 4.5\mu m .$$

In the real application, the lower limit of the air-gap was set at 5μm.

The up-limit of air-gap is decided by the coherent length of white light system. To achieve high-resolution measurement, a high visibility of the interference spectrum is needed. Because the spectrometer has a high wavelength resolution (<1nm), the coherent length decided by this factor is pretty large:

$$L_c \approx \frac{\lambda^2}{\Delta\lambda} \approx 700\mu m$$

So, in the working range (usually smaller than 20μm), this factor can be neglect.

A more important factor is the large numerical aperture (NA) of the multimode fiber. There are numerous modes propagate in a multimode fiber, and different fiber modes take different light paths. Obviously, the shortest path of EFPI sensor is P_{min}=2G and the longest one is about P_{max}=2G/cosθ (θ=$\sin^{-1}$ (NA)). Roughly, when the path different is larger than λ/2, the visibility was considered as too low to achieve high-resolution measurement. The NA of multimode fiber used in this system is about 0.15, so the up limit of air-gap is:

$$\frac{2G_{\max}}{\cos\theta} - 2G_{\max} = \frac{\lambda}{2}$$

$$G_{\max} = \frac{\lambda}{4}\frac{\cos\theta}{1-\cos\theta} \approx 19.2\mu m$$

By choosing a suitable initial air-gap and suitable materials for the sensor head, the dynamic range of the EFPI sensor can be limited in 5—18 μm. Comparing with the 200nm dynamic range of the SCIIB system, it's increased more than 50 times. That's the main advantage of the white light system over the SCIIB system.

Insensitive to the change of the polarization status

As discussed in chapter 2, in the SCIIB system, some optical components are polarization dependent. Even though a fiber optic depolarizer is connected in this system, the error induced by

the change of the polarization status is still as high as 0.5% when the fiber was bended and flipped.

In the white light system, the grating of the spectrometer is also a strong polarizer; it polarizes light along the vertical axis of the spectrometer. Yet, all the CCD pixels received the diffractive light from the same grating, so the polarization dependent of all pixels will be same. When the polarization status changes, the outputs from 2048 pixels will change by the same scale, the shape of the interference spectrum will not change. So the white light system is insensitive to the change of polarization status.

Demands for the geometrical parameters of the EFPI sensor

The white light system demodulates the air-gap from the interference spectrum directly. Many physical parameters, such as pressure, temperature, etc, have a linear relationship with the air-gap change, that means the white system will have a linear output in the whole dynamic range. The sensitivity is decided by the materials for the sensor head and the gauge length of the EFPI sensor. It's no necessary to set the initial gap at a very accurate value. Yet, in the SCIIB system, to fully use the limited linear range, the initial air-gap must be set at an accurate value. This makes the sensor fabrication for the SCIIB system is much difficult than that for the white light system.

Both the SCIIB system and the white light system have their special advantages. In general, for high-resolution applications, the white light system is the best candidate; when the measurement speed becomes an important issue, the SCIIB system is a good choice. In this project, for pressure, temperature and flow measurement, the white light system was employed.

4. Pressure and temperature sensor fabrication

4.1 Sensor fabrication system

As shown in Figure 4.1, the sensor fabrication system includes three sub-systems. They are the carbon dioxide (CO_2) laser heating sub-system, the white light fiber optic interferometric air gap monitoring sub-system, and the micro-positioning stage sub-system. A high-energy CO_2 laser is used as the heating source. It generates high-energy optical pulses at the wavelength of 10.6 μm. When the silica glass material is exposed to the CO_2 laser output, it absorbs the optical energy and converts it to thermal energy, which allows the silica glass materials be heated locally

up to very high temperatures. The white light fiber optic interferometric system is used in the system to allow accurate on-line monitoring of the sensor air gap. Several ultra-precise micro-positioning stages are also used in the system to allow precisely moving the two fibers in three dimensions. A computer is used to control and coordinate these three sub-systems so that the CO_2 laser output power, the motion of the stages and the sensor air gaps can be automatically and precisely controlled during the sensor fabrication process. Figure 4.2 shows the picture of the automated sensor fabrication system.

Figure 4.3 shows the Micro-positioning stage system.

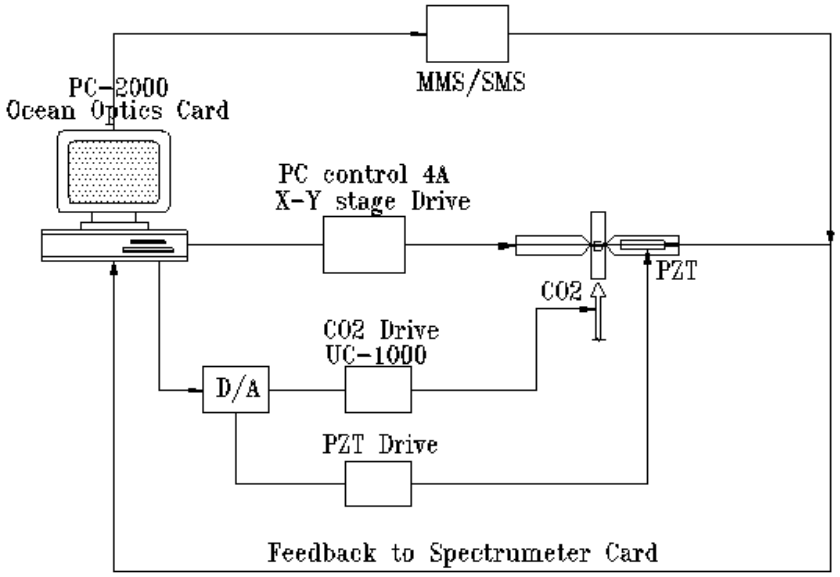

Figure 4.1 Schematic of the automated sensor fabrication system

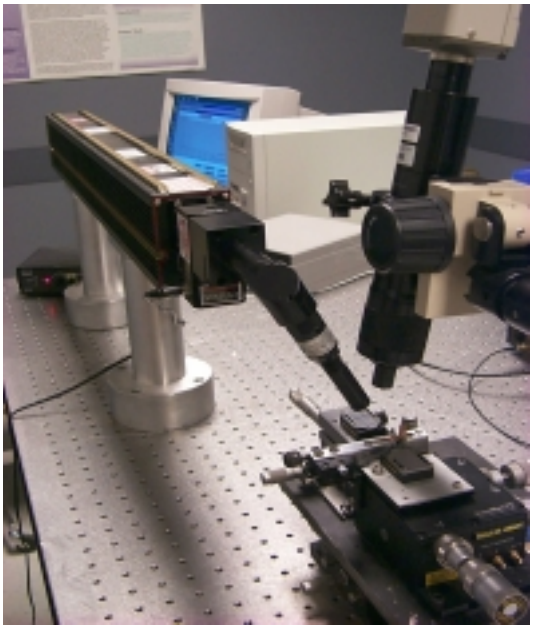

Figure 4.3 Micro-positioning stage system

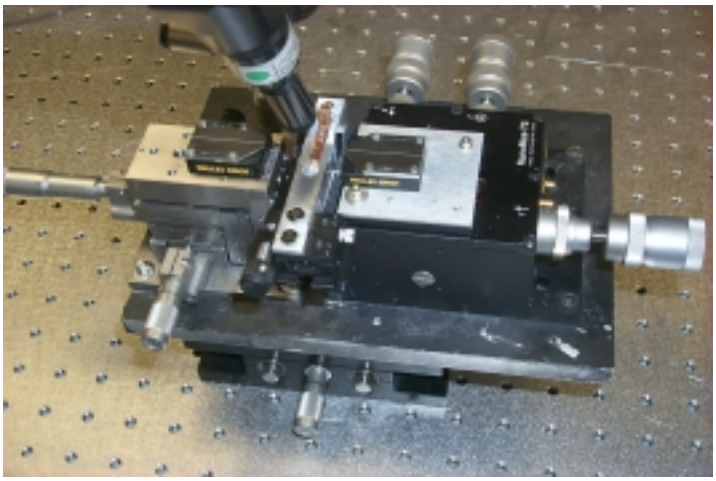

Figure 4.2 The sensor fabrication system

4.1.1 CO_2 laser sub-system

The CO_2 laser used in the system is a *SYNRAD, Inc* Model 48-2. The wavelength emitted by the laser is 10.6 μm, and the maximum output optical power under continuous mode operation is 25 W. The original beam diameter of the laser output is 3.5 mm. After using a germanium lens with a focal length of 2.5 inches, a spot size of about 100 μm in diameter can be achieved at the focal point, which results in a divergence angle of about 4 mradians. The laser can also be used to generate short optical pulses which are externally modulated through a controller, with a minimum pulse duration of about 200 μs.

The control of the CO_2 laser output involves two parts: the power level control and the lasing duration control. The power level control can be accessed by externally applying a 0-10 V voltage signal (corresponding to 0-25 W output power) and the pulse duration can be controlled by inputting a standard TTL gating signal to enable or disable the laser output. Because it is necessary to precisely control the heating time and the temperature during the sensor fabrication, we designed and implemented a special circuit to allow computer programmable control of the CO_2 laser. The block diagram of the CO_2 laser control subsystem is given in Figure 4.4. By properly programming the DIO-24 interface card (National Instruments), the power control signal is sent out to the D/A circuit, which converts the digital signal to an analog output from 0 to 10 volts at a resolution of 16 bits. The laser enabling or disabling signal is also converted to a TTL gating signal through the same circuit.

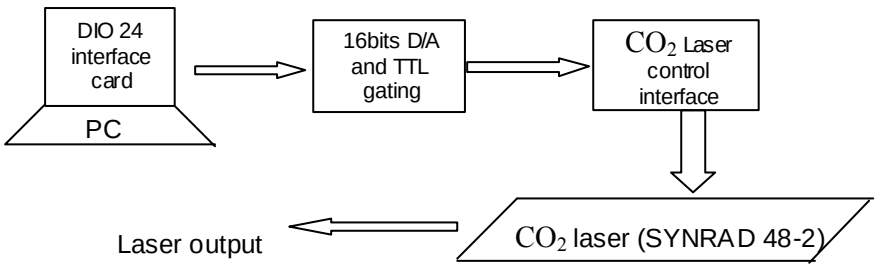

Figure 4.4 Block diagram of the CO_2 laser control subsystem

4.1.2 White light optic fiber interferometer sub-system

This sub-system is the main part of the automatic sensor fabrication system. It allows on-line monitoring of the length of the sensor air gap with a very high accuracy. The measurement of air gap length is achieved by demodulating the interference spectrum of the sensor output as described in the section below. The spectrum is obtained through a computer-interfaced spectrometer. Because we need to fabricate multi-mode and single-mode sensors, two white light interferometric air gap monitoring systems were constructed. The two systems share the same spectrometer but use different sources and fibers.

4.1.3 EFPI pressure sensor fabrication

The design issues of EFPI pressure sensor include the sensor head geometry, material, sensor sensitivity, and sensor dynamic range.

The geometry of a pressure sensor is shown in Figure 4.5. The sensor head is made by inserting two fibers into a fused silica capillary tube and thermally sealing them together so that an air gap is formed between the two cleaved fiber endfaces. When a hydrostatic pressure is applied, the capillary tube will deform, and as a consequence the cavity length will change. Effects in both the longitudinal and the transverse directions should be considered.

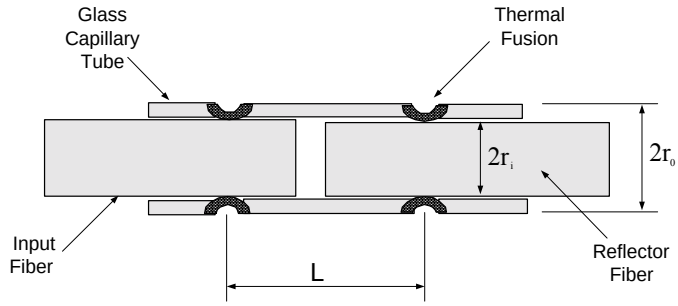

Figure 4.5 Geometry of pressure sensor head

Assume that the capillary tube has an outer radius of r_o and an inner radius of r_i. When the applied pressure changes from p_1 to p_2 the sensor air gap change (ΔL) can be expressed as

$$\Delta L = \frac{L}{E}[\sigma_z - \mu(\sigma_r - \sigma_t)], \qquad (4\text{-}1)$$

where L is the effective sensor gauge length defined as the distance between the two thermal bonding points; E is the Young's Modulus and μ is the Poisson's ratio of the capillary tube. For the fused silica materials used, $E=74$ *Gpa,* and $\mu=0.17$. Three strains are concerned in the analysis: σ_r is the radial strain, σ_t is the lateral strain, and σ_z is the longitudinal strain generated by the applied pressure. Those three strains can be calculated by the following equations:

$$\sigma_r = \frac{(p_2 - p_1)r_o^2}{r_o^2 - r_i^2}\ (1 - \frac{r_i^2}{r_0^2}) \qquad (4\text{-}2)$$

$$\sigma_t = \frac{(p_2 - p_1)r_o^2}{r_o^2 - r_i^2}\ (1 + \frac{r_i^2}{r_0^2}) \qquad (4\text{-}3)$$

$$\sigma_z = \frac{(p_2 - p_1)r_o^2}{r_o^2 - r_i^2} \qquad (4\text{-}4)$$

After combining Equations (4-2) through (4-4), the cavity length change of the sensor caused by the applied pressure can be expressed as

$$\Delta L = \frac{L(p_2 - p_1)r_o^2}{E(r_o^2 - r_i^2)}(1 - 2\mu) \qquad (4\text{-}5)$$

Equation (4-5) clearly shows that the change of the applied pressure can be measured by the change of the air gap length of the sensor. If we calibrate the sensor cavity length to a known pressure, we can measure the absolute applied pressure by measuring the change of the sensor cavity length.

The sensor head is fabricated by inserting two fibers into a silica glass capillary tube. The tube has an inner diameter of 130 μm, which is slightly larger than the fiber-cladding diameter of 125 μm. The outer diameter of the glass tube can be varied as required to achieve different dynamic ranges and resolutions according to Equation (4-5). In order to obtain good interference signals, the two fibers inside the capillary tube must be maintained in good alignment. Thereafter, the geometric parameters that can be used to modify the sensor performances are the effective sensor gauge L and the outer diameter of the capillary tube.

With the sensor head fabrication system, we can fabricate high-performance sensor heads. First, buffer-removed fibers used to fabricate the sensor head are carefully cleaned using Alcohol and well cleaved using a fiber cleaver. The buffer-removed capillary tube is also cleaned and well cleaved to the desired length. Second, with the help of the microscope, the two pieces of fiber are then inserted into the capillary tube and clamped on the positioning stages by magnetic holders. By adjusting the micro-motion stage system, the two pieces of fiber are moved to the preset positions where the desired initial sensor F-P cavity length is obtained. By moving the 2-dimention translating stage underneath the micro-motion stage system, the fiber and capillary tube assembly is brought to the center of the laser spot. The CO_2 laser emits light to heat the assembly with certain power level and duration controlled by the computer. We need to choose a proper power level and duration of CO_2 laser for good hermetically sealed sensor heads. After one side of the sensor head is bonded, the fiber and capillary assembly is then move to the other side to perform another same bonding process for the second bonding point. After completion of the second bonding process, a good sensor head is produced.

A photograph of a typical sensor head captured by the microscope is shown in Figure 4.6

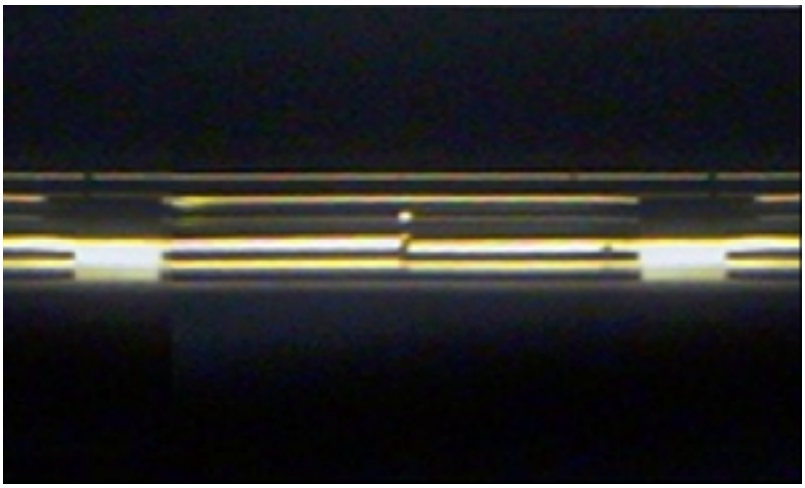

Figure 4.6 Microscopic photograph of the SCIIB sensor head

From the picture we can clearly see the sensor head F-P cavity formed by the input fiber end face and reflecting fiber end face and the two bonding points. And the sensor head is sealed hermetically.

4.1.4 Regular Single Mode Fiber Sensor

The geometry of sensor head is the same as showed in Figure 4.5. Both the input fiber and reflector fiber are 9/125 regular single mode fiber. And the fiber and the tubing are the same material. When fabricating sensor head, we use single mode White-Light system to monitor the air-gap. The measurement range is 15~50um, and the accuracy is 10nm. Figure 4.7 shows the Single mode White-light monitor window.

4.1.5 Regular multimode fiber sensor

The geometry of sensor head is the same as showed in Figure 4.5. Both the input fiber and reflector fiber are 62.5/125 (or 50/125) regular multimode fiber. And the fiber has a little bit larger CTE (Coefficient of Thermal Expansion) than the tubing. When fabricating sensor head, we use single mode White-Light system to monitor the air-gap. The measurement range is 4.5~20um, and the accuracy is 1nm. Figure 4.8. show the Multimode White-light monitor window.

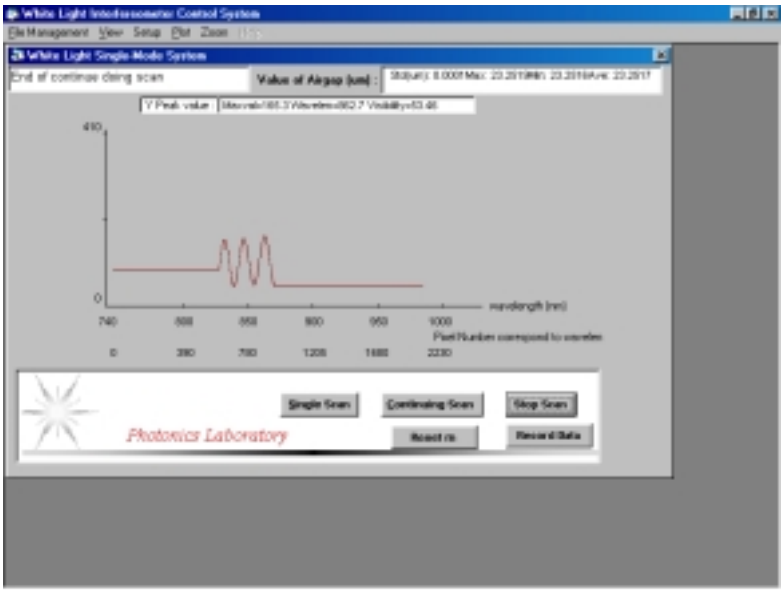

Figure 4.7 Single Mode White-Light monitor windows

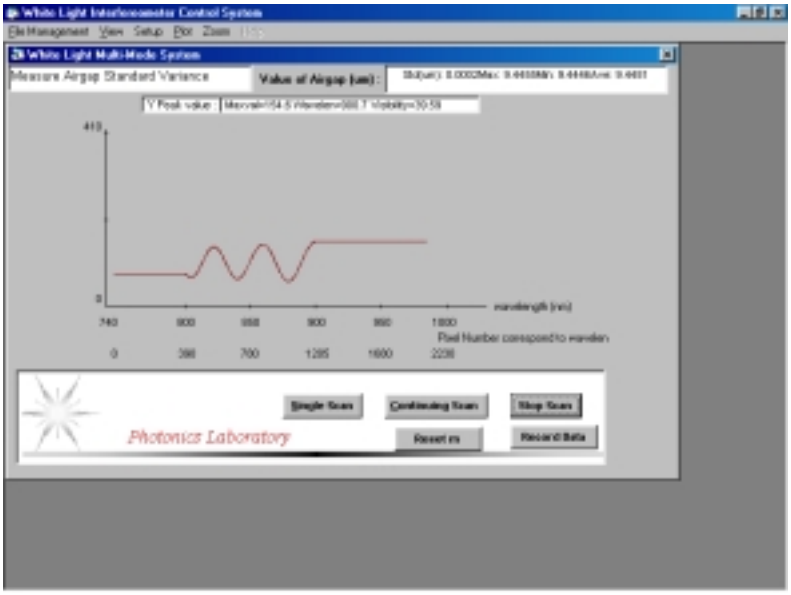

Figure 4.8 Multimode White-Light Monitor Window

4.1.6 Carbon coated multimode-single mode combo fiber sensor

In order to protect the sensor head from penetration by water, we choose the carbon coating multimode fiber in sensor head fabrication instead of regular fiber. The geometry of the carbon coating multimode fiber is showed in Figure.4.9.

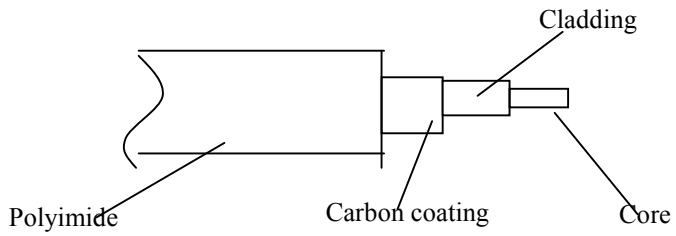

Figure 4.9 Schematic of the Geometry of Carbon Coating Fiber

Before sensor fabrication, the polyimide must be removed so that the fiber can be put in the tubing. It is not easy to remove the polyimide, two methods are developed:

(1) Using sulfuric acid erode the polyimide, first, put some sulfuric acid in a test tube, then heat it to 130 °C. Then dip the fiber in the tube until the color of the fiber change from brown to silvery. Then rinse the fiber with deionized water. This method is not difficult but time consuming and some dangerous. Remove the polyimide need 1 hour and before sensor

fabrication, the carbon coating fiber must be spliced with the output fiber of the white-light system.

(2) After much practice and experiment, we develop a technique to remove the polyimide of the carbon coating. Using sharp blade to remove the polyimide little by little. It is simple but difficult because the carbon coating is very brittle. The angle and the strength of blade must be controlled very carefully. When the technique is mastered it is only take several minutes to remove the polyimide and the fiber is not brittle as the one handled by the first method. Figure.4.10. sketch the process,

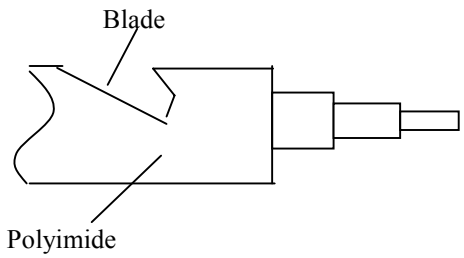

Figure 4.10 Removing Polyimide of Carbon Coating Fiber By Blade

4.1.7 Prevent from leaking

The optical fiber sensor must endure over 10000 psi pressure. We use APP system to test and calibrate the sensor, the bounding of the sensor must be strong enough to prevent from leaking.

After many experiments, a three points bounding method was developed.

The sensors have three bounding points on both sides of the air-gap is showed in Figure.4.11. In fact, the three points are continuous along the fiber and tubing, so the splice length is longer than one point bounding.

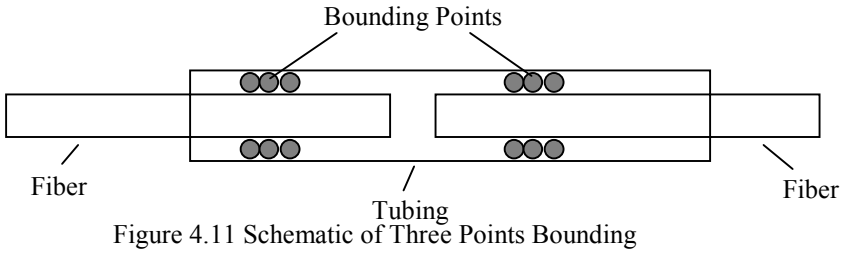

Figure 4.11 Schematic of Three Points Bounding

4.1.8 Reduce the temperature sensitivity

Since the carbon coating multimode fiber has a little bit larger CTE than the tubing, the temperature change will cause the change of air-gap (Fabry-Perot Cavity). It will cause big error in pressure measurement when the environment temperature is not stable. After many trials, we design a combo structure sensor head, as showed in Figure4.12.

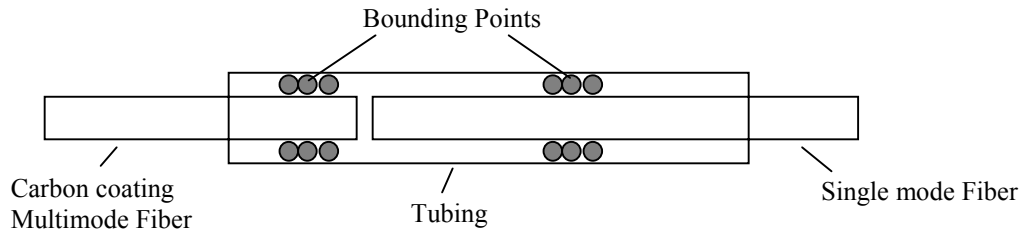

Figure 4.12 Combo Structure Sensor head

Between the two bounding sides, the length of single mode fiber is much longer than the carbon coating multimode fiber. Because the single mode fiber are the same material as the tubing, the sensor head thermal dependence is greatly reduced.

4.2 Precise air-gap control

For two reasons, we need to control the air-gap of the fiber sensor,

(1) The visibility will be related with the air-gap

(2) Air-gap measurement by the white-light system has its minimum and maximum limit.

After large experiment, we found that the air-gap can be controlled during CO2 laser bonding process. In general, we control the air-gap by bounding the reflector fiber side about 10 times. For the first 5 times, adjust the laser power by the series, 1.8w→ 2.0w→ 2.2→ 2.3w→ 2.33w. Then using the power between 1.9~2.2w to bounding final 5 times. If using the same power, the change of air-gap value will change linearly with the bounding times.

Figure 4.13 shows the air-gap adjusting process. After finished the first 5 times bounding, the air-gap changed from 21.6680 to 23.0665. Then choosing power between 2.0~2.2w, the air-gap changes linearly during the last 5 times bonding. At last, the air-gap was very close the expect value 23.1945um.

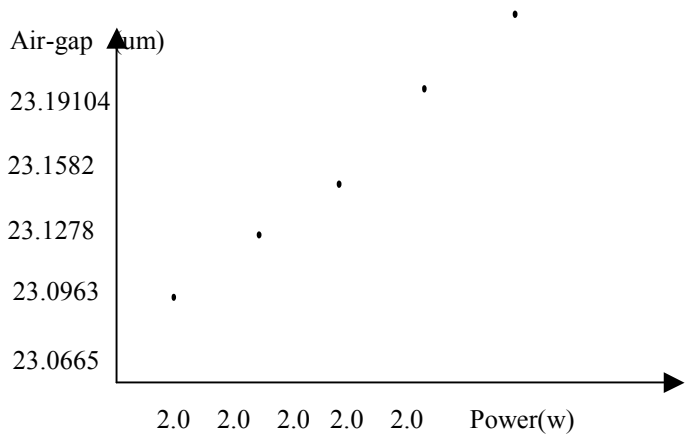

Figure 4.13 Air-gap controlled by laser bounding power

In Figure 4.13, bounding with 2.0w power will change air-gap about 30nm each time for the last 5 times. In fact we can use lower power to change air-gap more precisely. In practice, the highest precise is about 3nm.

4.2.1 Gauge length

The sensitivity od pressure sensor is directly determined by gauge length of the EFPI sensor head. In another hand, to make the sensor head deployable, the sensor size shold be small enough. After much experiment and tests, a 10mm gauge length is chosen. When pressure increases from 0~5000psi, the air-gap will decrease about 5um.

4.2.2 Eliminate nonlinearity

The air-gap will be shorter when the pressure applied on the sensor increases. In another word, the Fabry-Perot cavity will be smaller. The change of the air-gap should be linear with the change of pressure because the youngs modulus of the tubing is a constant. But some sensors show nonlinearity when pressure is relative low. After many tests, we found the reason is the friction force between the fiber and tubing in the gauge region. It maybe caused by some dust or electric static. Although the shorter the multimode fiber the smaller the thermal dependence, but we must tradeoff between thermal stability and nonlinearity. By enumerouse experiments, the optimum structure was found to 3mm carbon coating multimode fiber plus 7mm single mode fiber.

4.3.1 EFPI temperature sensor fabrication

The basic structrue of EFPI temperature sensor is similar to that of the pressure sensor,

which is illustrated in Figure 4.5. When the ambient temperature changes, the physical length of the capillary tube and the fibers will change, which results in the change of the air gap between the two fiber endfaces. Using the White light system, this air gap change can be demodulated for the interference spectrum and thus enable precise measurement of the temperature. Being the same structure was used for both pressure and temperature sensor, the fabrication process for temperature sensor are similar to that for pressure sensor.

To increase the temperature sensitivity, the geometric parameters and the material used for the alignment tube are different from that for the pressure sensor. The operating principle of EFPI temperature sensor can be described by:

$$\Delta G = (\alpha_0 L_0 - \alpha_1 L_1 - \alpha_2 L_2)\Delta T \qquad (4.6)$$

Where ΔG is the air-gap change induced by the temperature change ΔT, L_0 is the gauge length of sensor head; L_1 is the length of input fiber defined from the input bonding point to the end-face of input fiber; L_2 is the length of reflecting fiber defined from the other bonding point to the end-face of reflecting fiber; α_0, α_1, α_2 are thermal expansion coefficients (CTE) of glass tube, input fiber and reflecting fiber.

From equation (4.6), the designs of the temperature sensor focused on choosing suitable materials for the glass tube and the reflecting fiber to increase the temperature sensitivity.

The capillary tube is chosen to be made of borosilicate glass, which has a CTE of $\alpha_h=3.2*10^{-6}/°C$. In general, the optical fiber is made by doping small amount of germanium into pure silica material. Typical optical fibers have a CTE of about $7.5*10^{-7}/°C$, which is very close to that of pure silica.

In the down-hole environment, both high pressure and high temperature exist. To eliminate the pressure dependent of the temperature sensor, a special tube was used to isolated pressure from the temperature sensor.

The structure of pressure isolator for temperature sensor is shown in Figure 4.14. The pressure isolation is achieved by bonding borosilicate glass tubing outside the temperature sensor. The borosilicate tubing is sealed at one end, and is bonded to the borosilicate alignment tubing of the EFPI sensor on the other end. Thus outside pressure is isolated from the temperature sensor head. The borosilicate glass tubing can also provide mechanical protection to the joint point of lead-in fiber and the sensor tubing.

There are three reasons to choose borosilicate as the material for both inner and outer tube: First, borosilicate has much larger CTE compared to fuse silicate. From equation (4.6), a large difference in the CTE between tube and optical fiber will increase the sensitivity, resolution and dynamic range of temperature sensor dramatically. Second, the bonding point between same

materials is much stronger than that between different materials. Third, the laser power required for bonding the borosilicate tubing is much lower than the power required for bonding the fused silicate tubing. Thus the bonding process of the isolating tube will be harmless to the fiber.

The EFPI temperature sensors are also fabricated on the automated sensor fabrication station mentioned previously. The fabrication process involves inserting two cleaved fibers inside a capillary tube and using the CO_2 laser to thermally fuse the fibers and the tube together. We choose borosilicate material to make the capillary tube. In our experiments, we used the fused borosilicate tube available from Vitrocom, Inc. The inner diameter of the tube is 150 μm, and the outer diameter is 250 μm. The borosilicate pressure isolation tube is sealed with high power CO_2 laser on one end. The other end is bonded to the alignment tube.

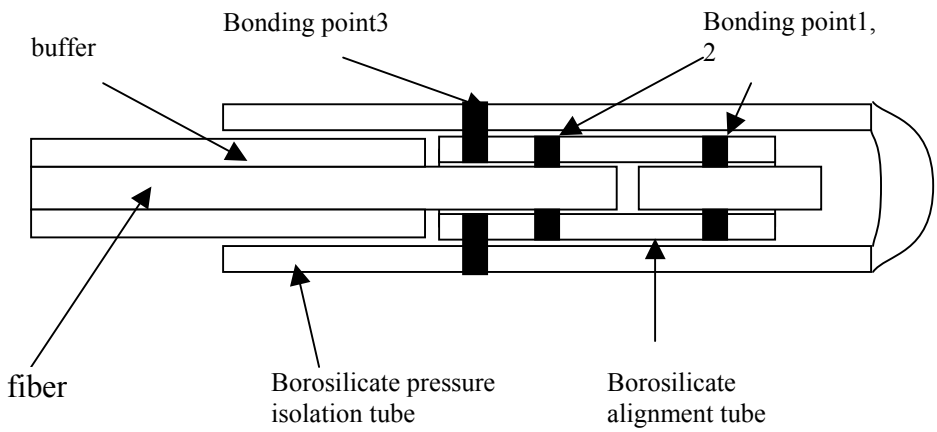

Figure 4.14 Pressure isolating tube of the temperature sensor

5. Description of optic fiber sensor packaging

The focus of this segment of the overall research project was aimed at development of suitable methods to protect the sensor head from penetration by water and to improve the mechanical durability of the sensor head such that it would be able to survive the rigorous deployment process. While the method of protection selected had to be able to provide adequate protection from moisture penetration, the protection would not be allowed to adversely affect the performance of the sensors. The requirements of the sensor packaging were:

1. Must provide adequate mechanical protection of the fiber sensor head and the connection between the sensor head and the transmission fiber
2. Must isolate the optical fiber sensor head from chemical corrosion and water penetration

3. For the pressure sensor, it must allow high pressure transduction fidelity
4. For the temperature sensor, it must isolating pressure while allowing high temperature transduction fidelity
5. The total finished size of the largest diameter of the protection package is smaller than 1millimeter
6. The method selected must be simple and easy enough that it could be applied at the oil field site
7. For simplicity, it was desired that the method used to protect the splicing point of the optical fibers also be able to protect the sensor head rather than having two separate methods for each

After investigation of many different methods to protect the sensor head including laser ablation carbon coating with and without polyimide coatings, sputtering of gold thin films, additional outer glass tubings, other method metallic coatings and methods to produce these coatings, etc., a suitable method was determined. This method involves encapsulating the sensor head in a soft metallic material while simultaneously encapsulating the metal in an outer heat shrinkable tubing. The process required identification of suitable metallic and polymeric materials such that the melting temperature of the metallic material was in the same range as the consolidation temperature of the polymeric material.

5.1 Structure features of the fiber sensor protection package:

The arrangement of the components in the structure of the packaging system are shown in Figure 1. The arrangement of the tubes could be performed quite easily be hand. In addition, no special microscopic equipment was necessary, so the process was very simple.

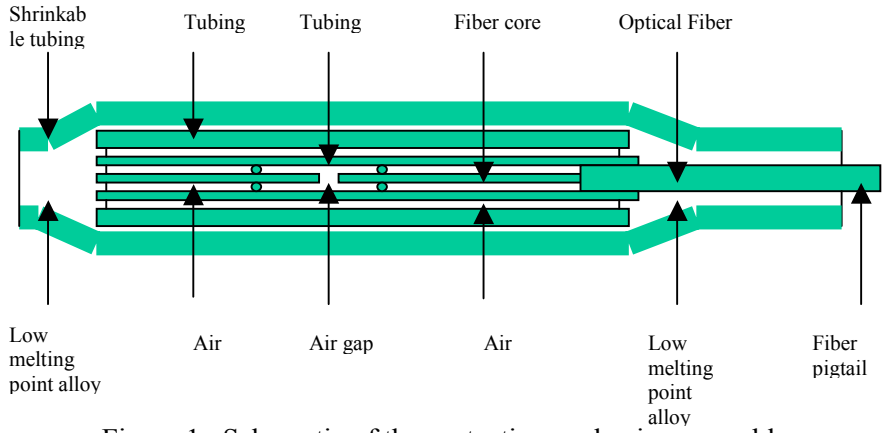

Figure 1. Schematic of the protection packaging assembly

1. Materials: Small tubing (silica glass tubing, stainless steel tubing, etc).
   Heat shrinkable tubing
   Low melting point metal or alloy

2. Structure: the sensor is positioned within the small outer tubing, of which, the diameter is only slightly larger than that of the sensor tubing. The small outer tubing is also a little bit longer than that of the sensor. The outermost part is the heat shrinkable tubing. Between the small outer tube which covers the sensor and the heat shrinkable tubing that covers the entire system, a low melting temperature metal is placed, which is used to isolate the sensor from moisture.

5.2 Description of the packaging process

Material preparation:

1. Sensor preparation—it was important to ensure that the dimension of the sensor is small enough to allow proper packaging while still meeting the overall size requirements imposed on the sensor package by the deployment process.
2. Small tubing preparation—it was important to ensure that cutting of the tubing was performed evenly and control of the length was accomplished such that the outer glass tubing was slightly longer than that of the sensor head.
3. Shrinkable tubing preparation—it was important to control the length of this tubing such that it was a little longer than small outer tubing
4. Low melting point metal preparation— metal tubing was fabricated from metal sheets to aid in assembly of the components for bonding. As such, the metal tubing was cut slightly longer than the small outer tubing and shorter than the shrinkable tubing.

Fabrication Procedure:

1. Put the sensor into the small outer tubing
2. Put the small outer tubing into low melting point metal tubing

3. Put the metal tubing into the shrinkable tubing
4. Carefully position the sensor and the tubing
5. Heat them in a controlled way to make the shrinkable tubing shrink, while the metal is melted and flows out of the two ends of the shrinkable tubing
6. The heating temperature, heating direction, and the amount of the metal is controlled
7. For the pressure sensor, the metal contacts the two ends of the sensor. For the temperature sensor, at least one end of the sensor is free.
8. Final treatment, cut the excess part of the package and remove the excess metal on the ends of the packaged sensor.

This method proved to be extremely simple to employ in an oil field setting, was robust enough to be able to be applied reliably, and was found to be a very inexpensive solution. No special tools were required to perform the operation. The only tools used were a heat gun, small screw driver, pliars and a ceramic plate to protect the surface below from heat. Extensive testing of the protected sensors was performed to ensure performance of the protection packing and to characterize the change in performance before protection versus after protection. These results will be presented in detail in a subsequent chapter, but overall the performance of the packaging method was found to be excellent.

6. Testing results of pressure and temperature sensors

To satisfy the requirements of different applications, several systems have been assembled and tested at CPT. These include the single mode SCIIB system for long distance and high speed applications; the multimode SCIIB system for short distance, low cost applications; and the multimode white light interferometer system for high resolution applications.

For pressure and temperature measurement, the principle requirement is high resolution. Therefore, the spectrometer based multimode white light system was selected as the signal demodulation system. In this chapter, the testing results of both the pressure sensor and the temperature sensor will be presented.

6.1 Testing results of pressure sensor

To evaluate the performances of the signal demodulation system and EFPI sensor heads, two pressure testing systems were designed and setup in CPT. One system has a relatively small pressure range but achieves a very high accuracy, the other system allows us to test the sensor up to a much large dynamic pressure range.

The first system is designed based on the Model 9035 pressure calibrator purchased from *Pressure Systems, Inc*. (*PSI*). The system configuration is shown in Figure 6.1. The calibration pressure range is from 0 to 250psi, and the long-term accuracy is about ±0.02% of the full range. This system allowed us to test the resolution and accuracy of the pressure sensor with a very high accuracy.

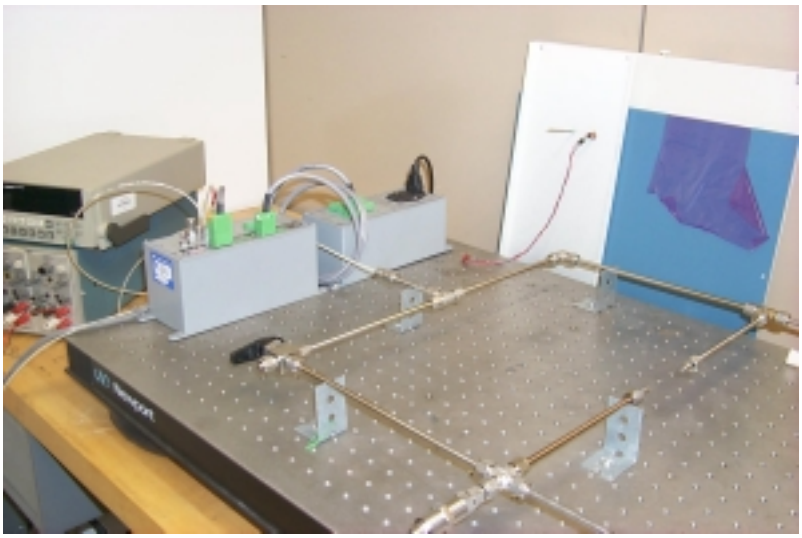

Figure 6.1. PSI 9035 based high accuracy pressure testing system configuration

The second system, as shown Fig 6.2, is a high-pressure calibration system based on the APCS controller and generator manufactured by *Advanced Pressure Products, Inc*. The pressure controller/generator supplies hydraulic pressure up to 20,000psi, and the accuracy of the pressure output is 0.02% of the full scale reading. To eliminate the interference from water penetration in the fiber and sensor head, the pressure transduction media used was a silicone based oil.

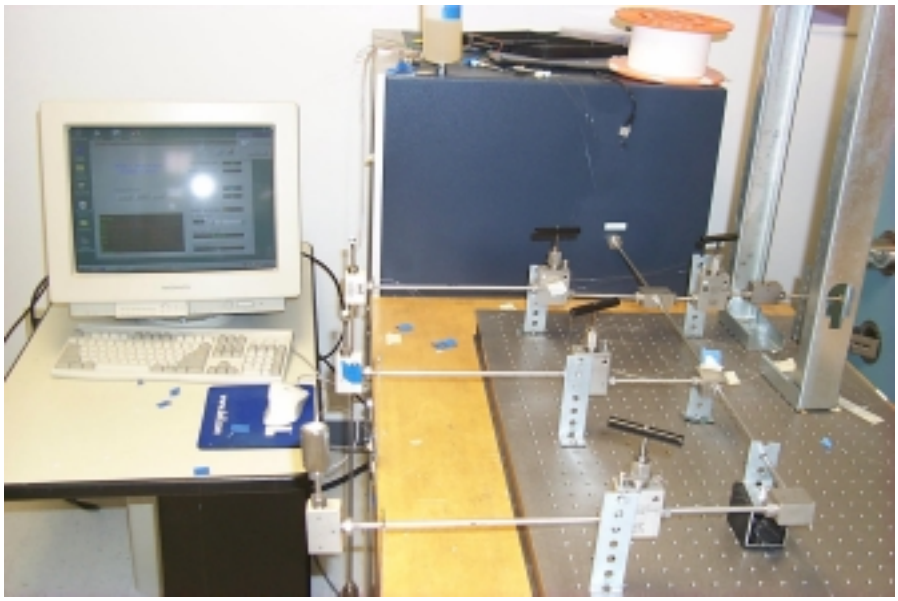

Figure 6.2. Schematic of APCS configuration with pressure sensor test system

There were three pressure channels fabricated in the APP pressure system, which can be controlled separately through several valves installed in the system piping. With this configuration, three pressure sensors could be tested at the same time. The sensors can also be tested under high pressures at elevated temperatures by heating one of the pressure test chambers using a flexible electric heating tape, which can achieve a temperature up to 700°C. This test was very important to evaluate the thermal effect on the pressure sensor. The temperature sensitivity testing results were useful feedback to the sensor fabrication improvement.

A typical test result of the pressure sensor is shown in Figure 6.3. The pressure sensor was tested up to 6000psi for 5 times. Two of them were performed under about 176 °C; others were performed at room temperature. The temperature dependence of the pressure sensor shown in Figure 6.3 is about 0.2psi/°C.

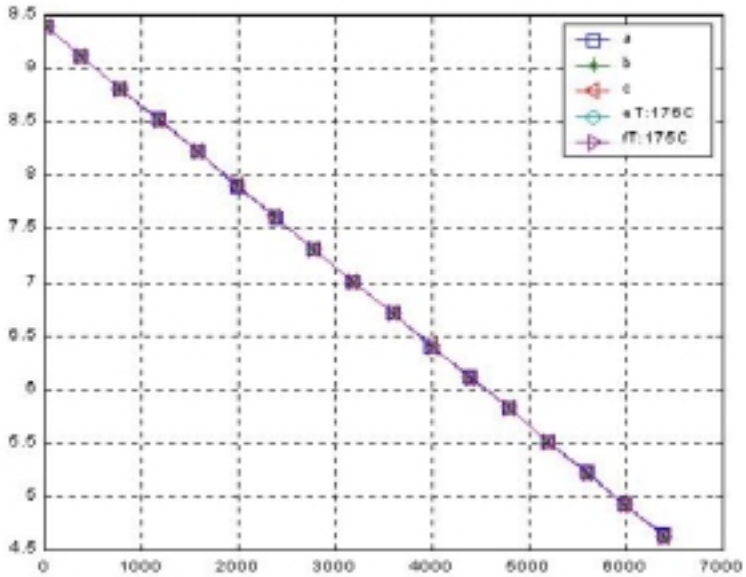

Figure 6.3 Testing results of a pressure sensor under different temperatures

The resolution of the pressure system is shown in Figure 6.4. In general, two times the standard deviation was taken as a measure of the resolution. The whole system was run continuously for 30 seconds. The sampling rate is about 5 points/second. The standard deviation calculated from the testing results is about 0.015nm, so the resolution of this system is about 0.03nm, which corresponds to 0.03psi.

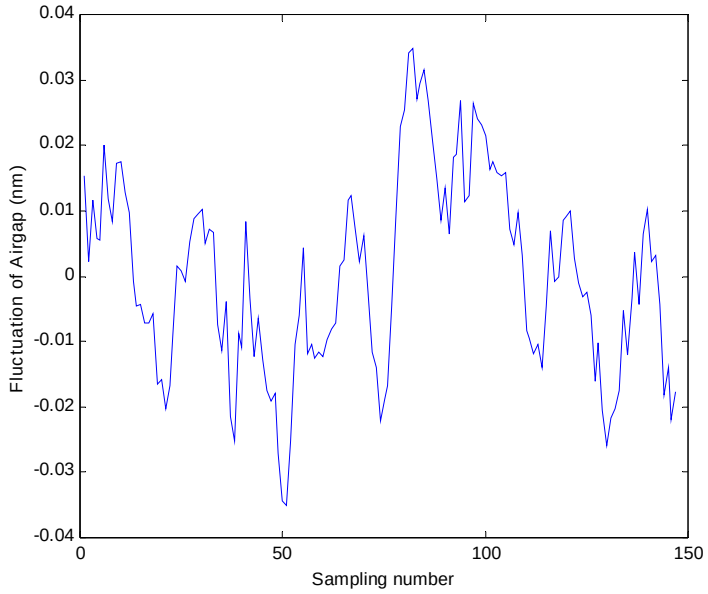

Figure 6.4 the resolution of pressure system

The 48 hours stability of pressure system is shown in Figure 6.5. The maximum air-gap error is less than ±0.5 nm, which corresponds to about ±0.5psi. Compared with the dynamic range of 6000psi, the stability is better than 0.01%.

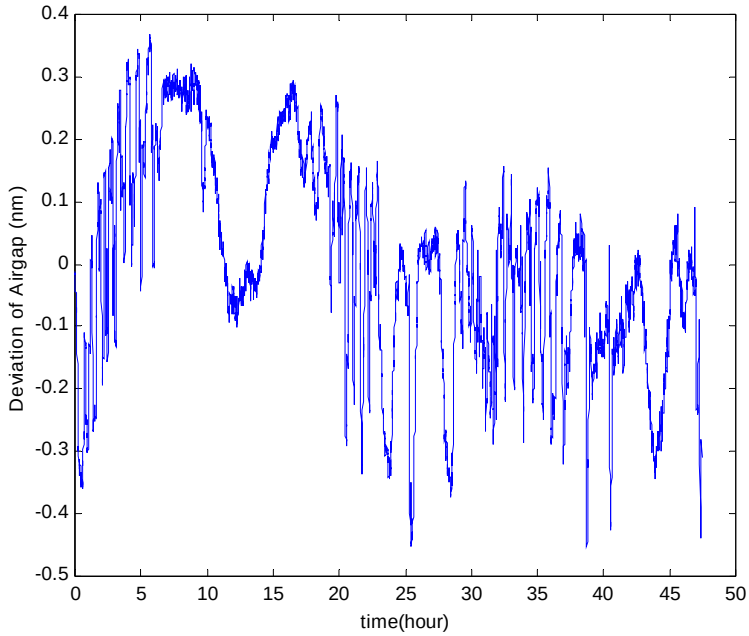

Figure 6.5 48hours stability of the pressure sensor

6.2 Testing results of temperature sensors

To evaluate the performance of the temperature sensor, a type-48000 furnace (Thermolyne Corporation) was used for the temperature test. The temperature range of this furnace is from room temperature to 1200 °C. To increase the resolution of the temperature test, a thermocouple, which was put aside the EFPI temperature sensor, was used as the temperature standard. Signals from the thermocouple and the EFPI sensor were sampled into the PC synchronously, and a self-developed program was used to evaluate the performance of the temperature sensor.

Figure 6.6 shows a typical testing result of the temperature sensor. While the temperature of the oven increased from room temperature to about 190 °C, the air-gap of the sensor head increased from 7μm to about 16μm.

One problem involved in the temperature testing is the hysteresis effect. In general, a relatively long time period is necessary for the oven to reach a stable temperature. While the heating element is heating, the temperature distribution inside the oven maybe large. This induces

the hysteresis effect between the output of thermocouple and the EFPI temperature sensor. This is shown in Figure 6.7.

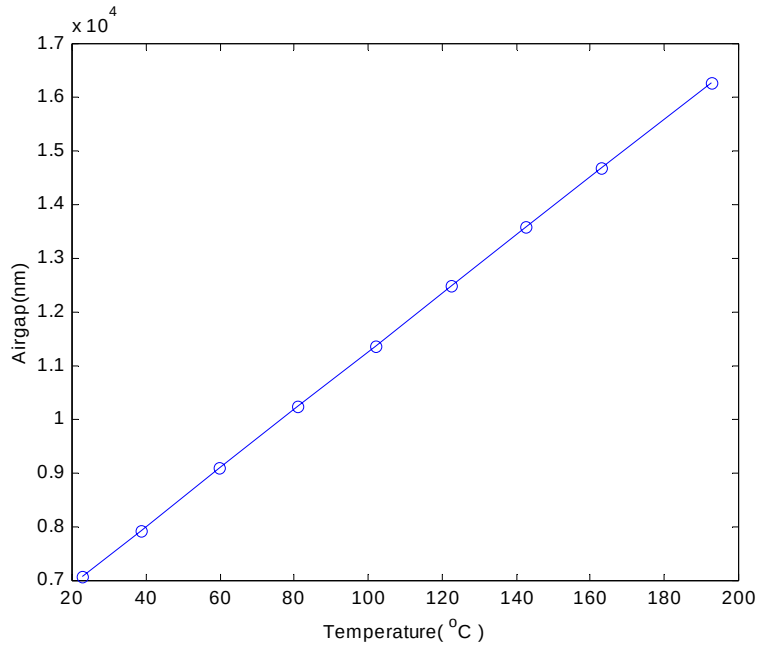

Figure 6.6 the calibration curve of temperature sensor

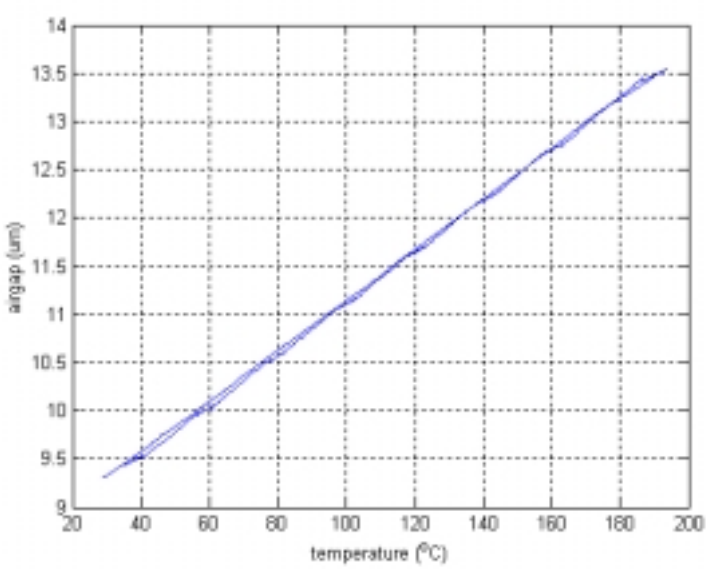

Figure 6.7 Hysteresis effect in temperature measurement

The hysteresis effect shown in Figure 6.7 is about 1.5°C. The temperature testing system is still under improvement to solve the hysteresis problem.

6.3 First field test in Coalinga, CA

To evaluate the performance of the fiber optic sensor system in the oil site, a multimode white light pressure sensor system has been tested in the oil site of Chevron Company (Coalinga CA) for more than three months. The main purpose for the first field test include: verify the deploy-ability of the sensor head; test the remote data access through the Internet; evaluate the long term stability of the sensor head in the down –hole environment.

6.3.1 Sensor deployment

A hydraulic optic fiber deployment system developed by the Chevron Company was used to deploy the pressure senor. The sensor head with connecting optical fiber was pump down by utilizing hydraulic oil as the suspension media and force imparting member. The sensor head moved down about 250m along the stainless steel pipe. The inner diameter of the metal pipe is smaller than 4mm, and there are several connectors along the pipe. Several times during the deployment of the sensor, the sensor apparently got stuck on something, and the senor had to be drawn back a little by reversing the fluid flow direction and pushed forward again. The ability of the sensor to survive the deployment process is attributable to the improvement of the mechanical durability of the sensor head. The position of the sensor head in the oil well can be monitored by OTDR.

After deployment, a pump was used to increase the pressure inside the testing pipe to about 3000Psi, and then all valves were shut off to keep a constant pressure inside the pipe.

6.3.2 Remote Access and Control

Hardware Configuration

The host computer which controls the fiber sensor measurement is a Dell Latitude, P2-350 notebook, 128MB memory and 4.5GB hard disk. The Ethernet card is a SMC8040Tx 10/100 PC Card.

The client computer is one PC Desktop which is a P2-350 with 128MB memory, 6GB hard disk and a NE2000 compatible Ethernet card. This computer will remotely control the host computer and obtain the measurement data through the internet.

Software Configuration

The operating system is Windows 98 second edition, the remote control software is Symantec pcAnywhere 10.0. And the software of VPN service is Nortel extranet access client V2.50.

Connection Establishment

a. Host Computer:

We need to make the notebook logon the Chevron's Intranet and get a static IP. It is achieved by inputing the authorized user name and correct password when the computer enters Windows 98. The host computer must maintain the logon status.

b. Client Computer:

On the client side, the computer is on the Internet all the time through the Local Area Network of Virginia Tech. Each time we want to remotely control the host computer, the following two steps are needed:

(1) Run the extranet access client software, there will pop up a window as in Figure 6.8.

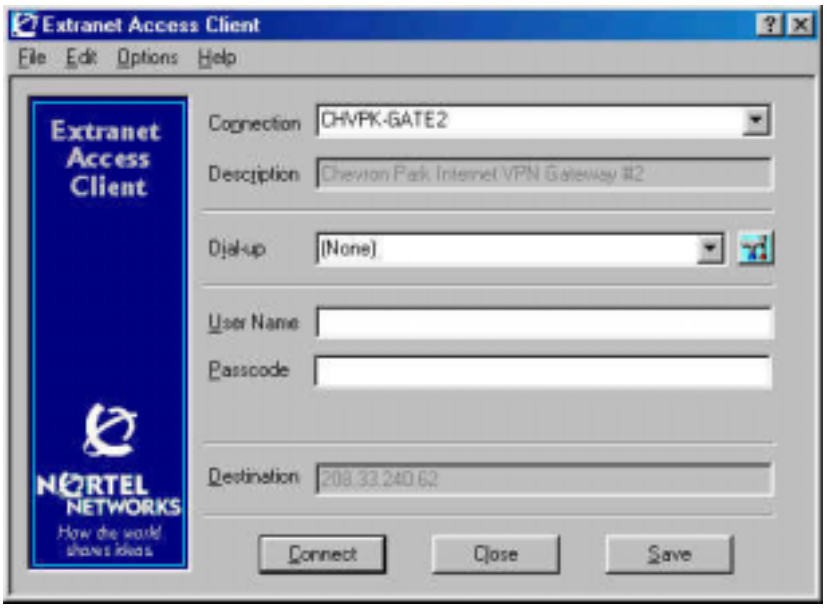

Figure 6.8. Nortel Extranet Access Client Software

Then input the authorized user name and the pin plus passcode. The passcode is generated every 60 seconds by a security card.

(2) Run ‘pcAnywhere’and start the ‘doe’ task, which will try to connect to the host computer, when the host computer responds there will pop up a window (showed in Figure 6.9) requesting the user name and password for security connection.

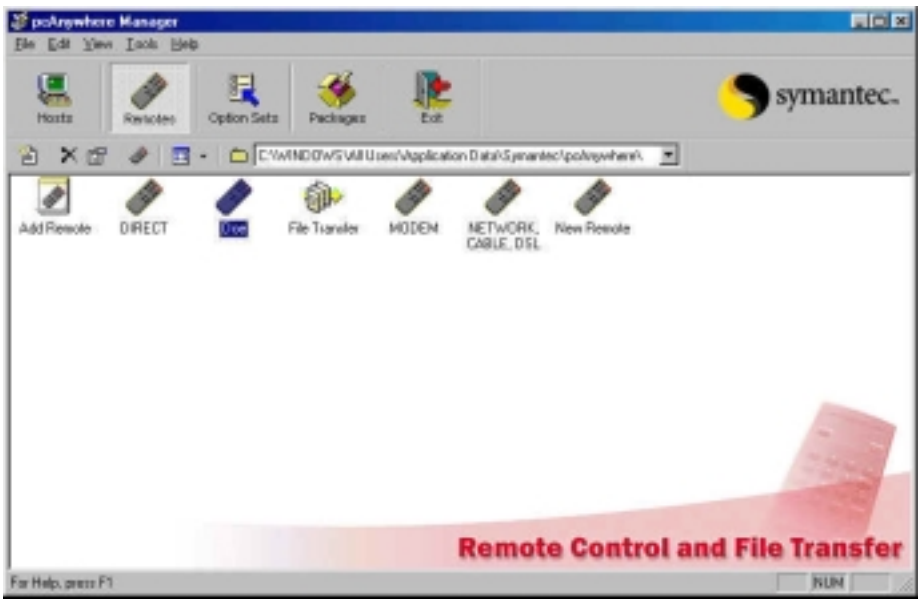

Figure 6.9 pcAnywhere Manager Window

When all of above is done successfully, the whole screen of the host computer will be displayed on the client computer. Then you can control the host computer by using the client computer’s mouse or keyboard.

Data Saving and Remote Access

The fiber sensor based measurement system measures the pressure in the oil well every minute and saves the data to the hard disk of the host computer. And the software generates a new filename at time 00:00:00 everyday so that one file will save one day’s measurement data. The filename is the date, for example, ‘10-03-2001’. The data format is text, as follows:

Time		Pressure
10-03-2001	10:23:00	2290.3298
10-03-2001	10:24:00	2290.3021
……		

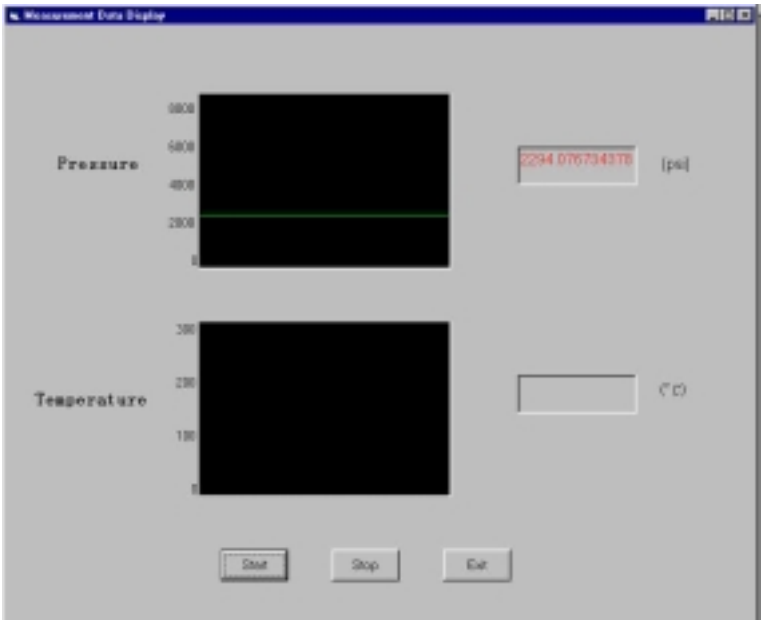

Figure 6.10 Pressure Measurement Window

It is convenient to find one day's data by searching the filenames. And using one day for one file will not cause a huge size data file so that the download will be easy.

For remote data access, we can use the 'File Transfer'function of the pcAnywhere. Run the file transfer function, there will pop up a window showing the directory list of the host and the client computer separately in two subwindows. We can use a mouse to drag the file from the host window to the client window to finish the download.

Network Security

The network security of the remote access is very important. The host computer can not be accessed without running extranet access software first. The host computer is in Chevron's Intranet. Correct username and passcode are needed. Especially, the passcode consists of PIN and Security Card Number, and Security Card Number will change every 60 seconds, it will be examined by the sever of the Chevron's gateway.

Also, pcAnywhere has its own network security, username and password are needed to establish the remote control. Therefore, the network security is very good.

6.3.3 Long-term stability

This system has been running for more than three months in the down-hole environment, and the computer can be accessed remotely from Virginia Tech. The whole system functions well during this period. Figure 6.11 shows the testing results for 90 days.

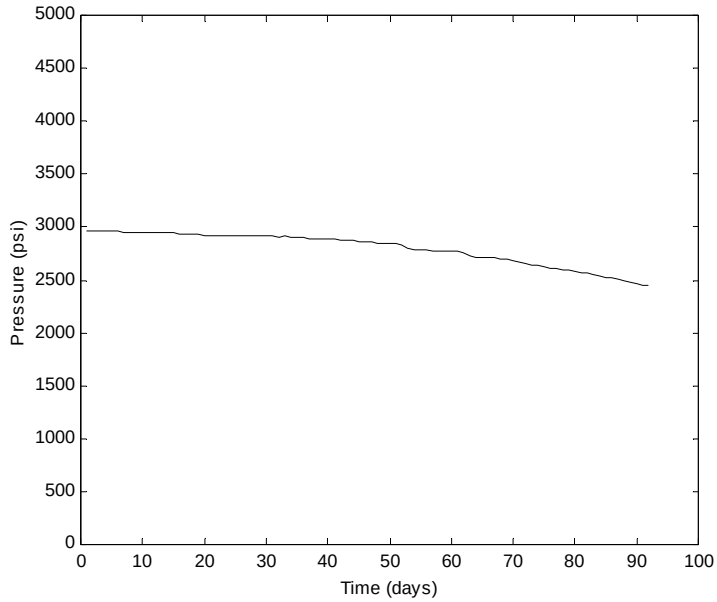

Figure 6.11 The 90 days testing result in oil site

The slow decrease in pressure had been expected because of the leakage of the pressure system. A surface mounted pressure sensor in line with the fiber optic pressure sensor also shows the downward trend of the pressure with time. The magnitude of the drift downward for the surface mounted pressure sensor is much larger than for the subsurface fiber optic sensor. It is not certain why the pressure drift of the surface mounted sensor is so large. This will be one of the objects for final test, to sort out the differences in the drift of these sensors.

7. Fiber optic flow sensor

The monitor of oil flow velocity in the oil reservoir with a high accuracy is vitally important for down-hole oil exploration and oil recovery applications. One of the tasks scheduled for this project is to investigate the application of the fiber optic flow sensors.

Since the EFPI sensor scheme has been proven to be effective for highly sensitive and accurate measurement of pressure and temperature, it is thus possible to design flow meters based on the combination of the EFPI sensor technology with various typical configurations, such as pitot tubes, orifices, thermal dispersion, acoustic dispersion and vortex shedding-induced vibration schemes. The ultra-small size of the EFPI sensor allows the fabrication of miniaturized flow sensors,

which could be easily deployed down-hole oil well, and would exert minimum perturbations in the measurement environment.

By investigating various flow meter configurations and possible combinations of them with EFPI sensors, the strain-based EFPI sensor has been chosen for design, fabrication, experimental testing and evaluation to meet the requirements for oil field instrumentation. In this section, we report the details of fiber optical flow sensor system design, fabrication method and the test result.

7.1 Principle of fiber optical flow sensor

Flow rate measurement was achieved by using an EFPI fiber optic sensor head with white demodulating system. Special considerations had been taken in order to satisfy all the requirements for the down-hole applications, which include temperature stability, high-pressure isolation, high sensitivity, large dynamic range, etc.

The basic principle of the fiber optic flow sensor is illustrated in Figure 7.1. A multimode white light system is used for demodulating the flow signal. The configuration of the sensor head is also shown in Figure 7.1.

Two symmetrical EFPI sensors were used to construct the flow sensor head. The structure and operating principle of EFPI sensor were described in Chapter 4. Again, the automatic CO2 laser sensor fabrication system was used to fabricate the EFPI flow sensor. The difference between the flow sensor and pressure sensor is that only one fiber (the reflected fiber) was thermal bonded with the glass tube, the other fiber can be moved inside the tube freely. By adjusting the poisition of free fiber, the air-gap of the EFPI sensor can be set at a suitable value. Then the two EFPI sensors were bonded on the two sides of a brass plate (act as a cantilever). Both two ends of capillary tube and two fibers were bonded firmly on the surface of metal cantilever beam, and then cover the free ends of the capillary tube with solder film to isolate from the water. The cantilever beam was fixed by the T-fitting into the testing pipe. When the liquid medium flows through the pipe, a force will be applied on the metal cantilever. The air-gap of EFPI sensor will change as the brass plate deforms, as a consequence the cavity length of the sensor can be used to demodulate the flow rate. Obviously, as the flow rate increase, the air-gap of EFPI sensor faced to the flow rate direction will increase, and the air-gap of sensor attached on another side will decrease. Theoretically, if the two EFPI sensors are identical, they will have the same responses to changes of temperature and pressure. So by calculating the difference between the output of e

two, the applied flow rate can be detected and the influence of the temperature and pressure can be compensated automatically.

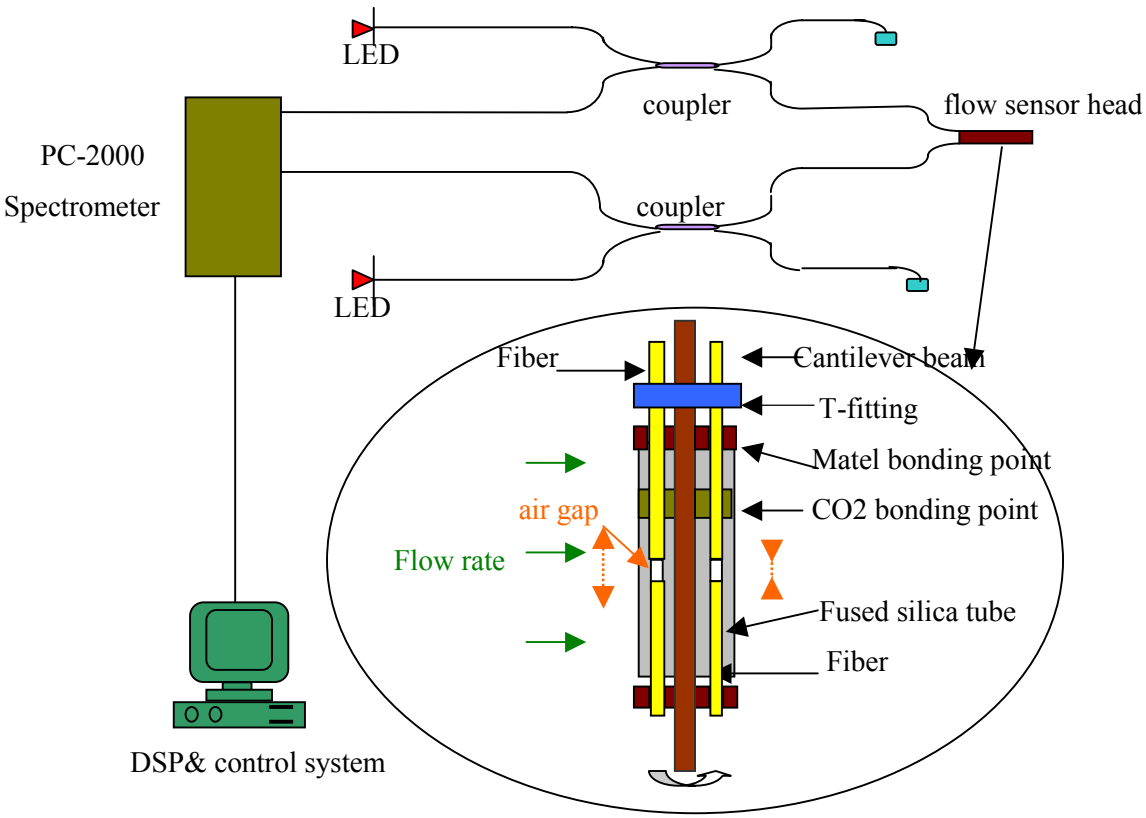

Figure 7.1 Illustration of the principle of the fiber optic acoustic sensor.

Assume that the substrate has a length of L, a width of c and a thickness of d, when the liquid flow through the pipe, the force acted on the substrate can be calculate from the momentum principle:

$$F \times t = m \times v \tag{7.1}$$

Here F is the force on the cantilever, m is the masses of fluid pass by the cantilever with in time t, and v is the flow rate of the fluid.

The mass of fluid can be calculated from:

$$\begin{aligned} m &= \rho \times V, \\ V &= S \times l = S \times v \times t, \\ S &= c \times L_b \end{aligned} \tag{7.2}$$

Where ρ is the density of the fluid, V is the volume of liquid flowed through in time t, S is the area of the cantilever beam, c is the width of cantilever, d is the thickness of cantilever.

From equation (7.1) and (7.2), the applied force F is

$$F = \frac{m \times v}{t} = \frac{\rho \times S \times t \times v \times v}{t} = \rho \times S \times v^2 \qquad (7.3)$$

Suppose F acts on the cantilever uniformly, the related strain will be

$$\varepsilon = \frac{6FL_b}{Ecd^2} \qquad (7.4)$$

Here E is the young's modulus of substrate, L_b is the distance between two bonding points.

At the end of the cantilever, the length changes of the beam is

$$\Delta L = \varepsilon \times L = \frac{6FL_b L}{Ecd^2} = \frac{6\rho S v^2 L_b L}{Ecd^2} = \frac{6\rho v^2 L_b{}^2 L}{Ed^2} \qquad (7.5)$$

Here L_b is the length of the cantilever beam.

Supposed that strain of the beam transfer to the sensor tube completely, because the fibers were bonded with tube, so the change of the sensor's air gap can be getting from the above equation.

$$\Delta L = \varepsilon \times L = \frac{6FL_b L}{Ecd^2} = \frac{6\rho v^2 L_b^2 L}{Ed^2} \qquad (7.6)$$

Where L is the distance between the 2 bonding points.

For the cantilever made of brass shim, $E = 4.2 \times 10^{10} Kg/m^2$. The geometric size of cantilever is L_b=25mm, c=5mm, d=0.5mm.The tube length of EFPI sensor is L=20mm, the original air gap is a= 12.00um.

Figure 7.2 shows the relationship between the output of air gap changes and the applied flow rate that is described in equation (7.6).

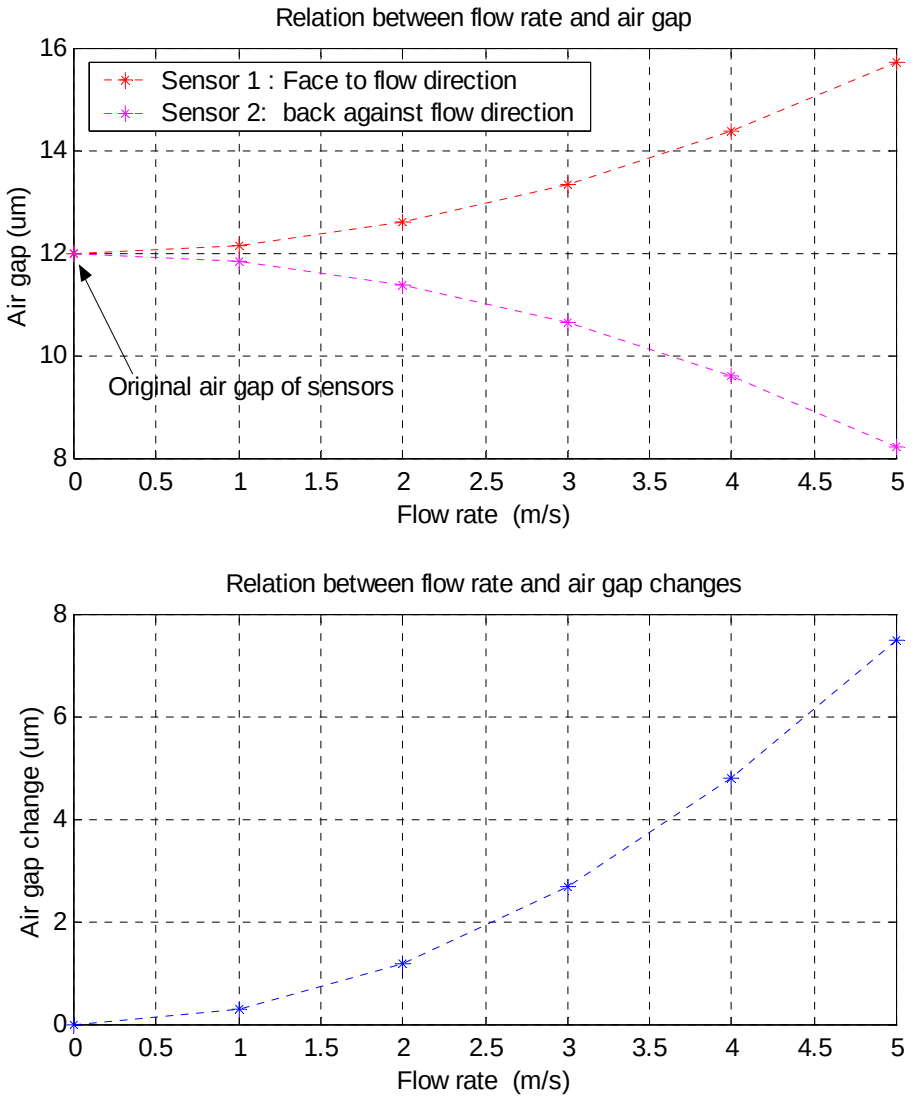

Figure 7.2 Relation between the air-gap of flow sensor and the applied flow rate

Equation (7.6) and Figure 7.2 show out that the air gap of EFPI sensor is clearly related to the applied flow rate. After the calibrating curve is acquired, we can measure the absolute applied flow rate by measuring the change of the sensor cavity length.

7.2.1 Flow sensor fabrication

From the principle of flow sensors described above, the fabrication of the flow sensor includes several steps: the first is the fabrication of EFPI sensors; the second is the package of flow sensor. Based on the previous works of EFPI sensor fabrication, we have very effective

technique to control the characteristics of sensor, such as the effective gauge length, the air gap, visibility, etc. The fabrication of EFPI sensor is described in chapter 4. The ultra-small size of EFPI sensor allows the fabrication of miniaturized flow sensors, which could be easily deployed down-hole oil well, and would exert minimum perturbations in the measurement environment.

To compensate the temperature and pressure dependents of the flow sensor automatically, two EFPI sensors are attached on the different sides of the brass plate. The technique to transfer the applied flow rate to the strain of the substrate successfully is the key point. Because the package processing usually change the sensor characters, the symmetry of the two sensors after package is very important.

In first step, works are focus on the flow sensor structure package technique with single EFPI sensor. Many kinds of materials had been tried as the cantilever beam; also several methods had been used to bond the EFPI sensor with the cantilever beam. A relative stable flow sensor had been achieved by attaching the EFPI sensor on the brass steel with low temperature solder.

Although metal materials usually have high CET, which will affect the air gap of sensor head greatly when temperature changes, as described in 7.1, this effect can be reduced effectively if the characteristics of two EFPI sensors are identical. The prototype flow sensor is shown in Figure 7.3.

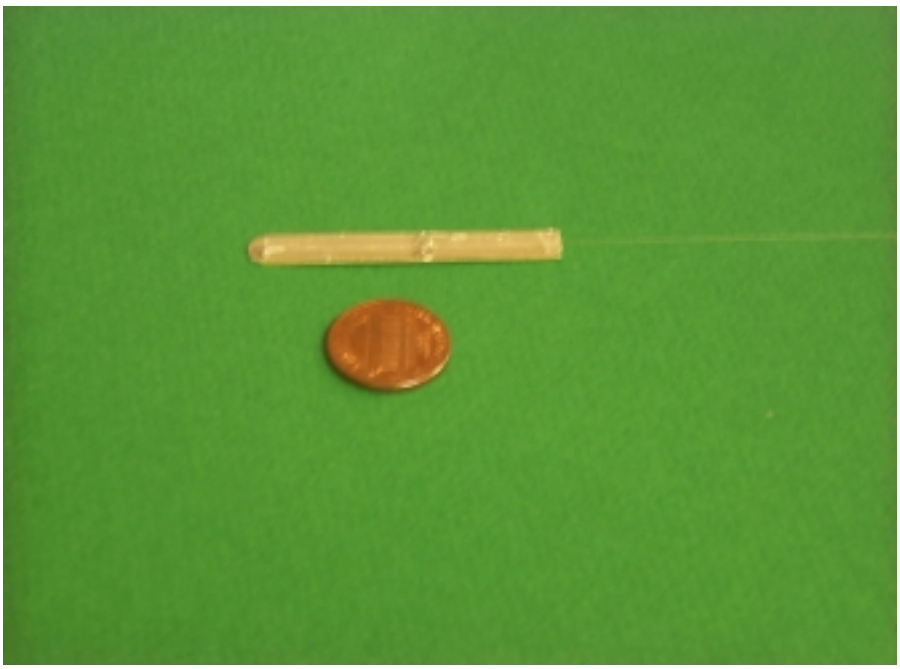

Figure 7.3 Illustration of prototype flow sensor

7.3 Flow sensor testing system design

To evaluate and test the performances of flow sensor, a flow sensor testing system was setup in VTPL. The structure of flow sensor testing system is shown in Figure 7.4.

The experiment set-up includes a *FP7001* paddlewheel flow meter purchased from *Omega Technologies Company.* Using 1" pipes, the calibration flow rate range is from 0 to 50 G/M, and the long-term accuracy is ±2% of the full range. A ¼ HP *Wayne* submersible utility pump drive the water to the PVC pipes, and the maximum flow rate inside the pipe is about should up to 40G/M. A *DPF700* meter was used to record the flow rate output from the FP700I flow meter, and it can be connected with a PC through RS-232 port.

As shown in Figure 7.4, both the fiber optical sensor and the thermometer were put into the testing pipes. The pumped flow rate can be adjusted by change the power input of the electrical pump. Both the flow sensor output and the flow-meter output were recorded automatically. The testing system is also shown as Figure 7.5.

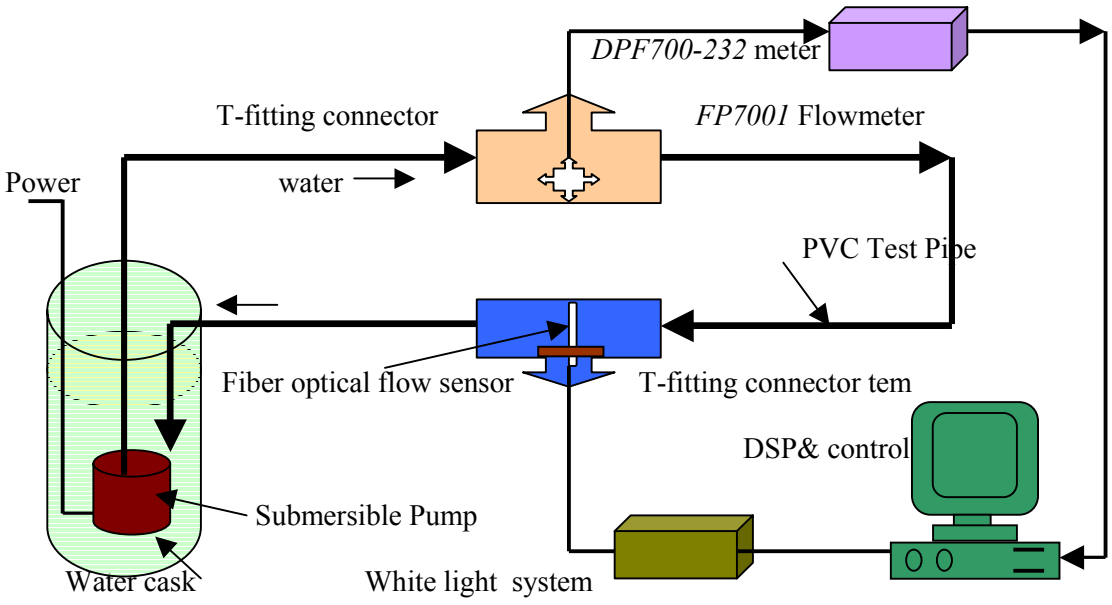

Figure 7.4 Flow rate testing system configuration

Figure 7.5 Picture of flow rate testing system

7.4 Experiments and results

Using the testing system described in last subsection, many experiments have been taken out to evaluate the performance of the flow sensor system. The maximum flow rate of the ¼ HP *Wayne* submersible utility is only 13G/M (1.6m/s), which is 1/3 of the supposed full range. In this range, the related accuracy of the Omega flow meter will decrease to 8%. A high power pump had been ordered, which can deliver a flow rate up to 50G/M.

7.4.1 Sensor calibration

Before the flow sensor probe can be used for actual flow measurement, it must be calibrated to find out the relation between the output and the applied flow-rate. The sensor calibration is usually conducted by applying known flow rate within its operating range. The one-to-one relation between the sensor original output and the applied flow rate form the calibration curve which can be stored in PC and later is used to convert the sensor output to the flow rate reading.

Using the experiment setup showed in Figure 7.5, the flow sensors were calibrated. To ensure the accuracy of the calibration, the pump held at each flow rate for about 3 minute before moving to the next step. By averaging the outputs of both flow meter and EFPI flow sensor at

each step, the errors can be minimized. Figure 7.6 plots the flow sensor output versus the applied flow rate after averaging. The one-to-one relation of the applied flow rate and the output from white light system was then used to find the calibration equation through polynomial fitting. Experimental results revealed that the optimal order of the polynomial fitting was 3. Usually, the calibration curve was obtained by taking the average of several consecutive calibration data to further ensure the accuracy of calibration.

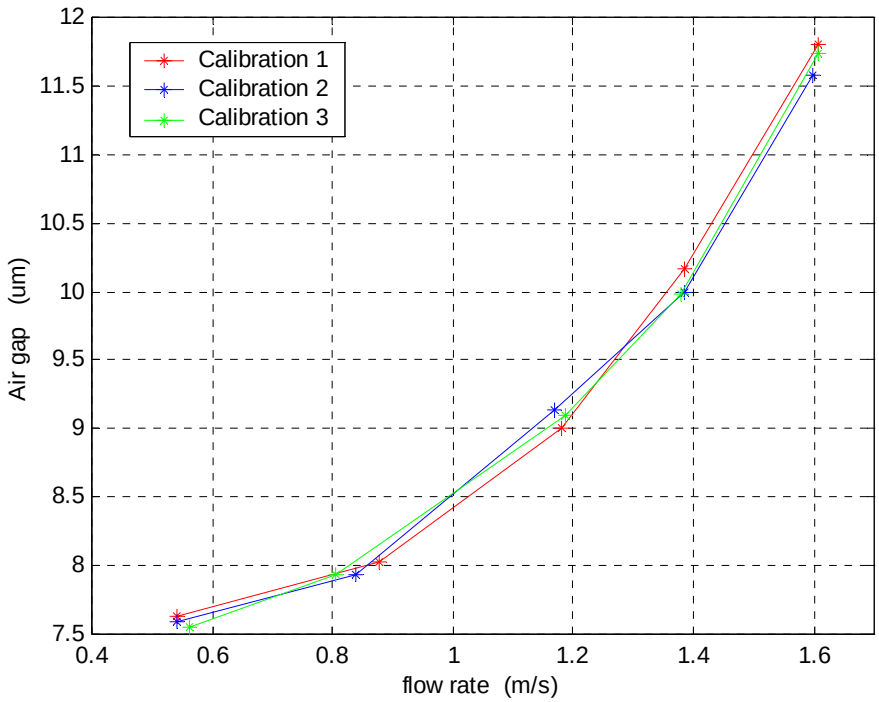

Figure 7.6 Flow rate sensor system calibration lines

7.4.2 Resolution of flow rate measurement

The resolution of the sensor system is usually interpreted by its standard deviation of a series of pressure measurements. It is common to use twice the standard deviation as the direct measure of resolution. The evaluation of the sensor resolution was performed using a calibrated sensor with the linear range of 1.6m/s. The sensor was put into the testing pipe; the data from the testing system was sampled at a rate of 50 samples per second for one minute, which should be high enough compared to the system's frequency response of 10Hz. The flow rate measurement outputs within the one-minute sampling period are plotted in Figure 7.7. The standard deviation of the flow rate within this time period was calculated to be σ=0.0033m/s. Therefore the resolution of the sensor system was estimated to be 2σ=0.0066m/s. The normalized resolution with respect to the dynamic range of the system was 0.4% of the full scale.

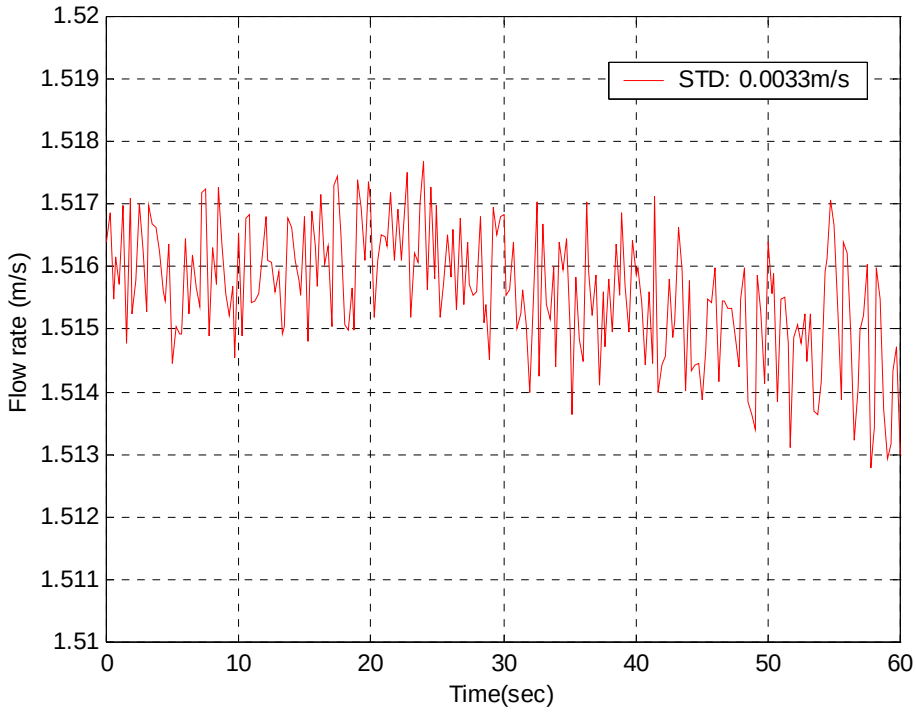

Figure 7.7 Standard deviation measurement of the SCIIB pressure sensor

7.4.3 Sensor repeatability

Repeatability of the flow sensor can be measured by applying flow rate in a certain preset range repeatedly. The largest difference of the sensor output readings can be used to specify the repeatability of the sensor. The same calibrated flow sensor was used to evaluate the repeatability of the system. Using the testing system mentioned above, three consecutive measurements up to the maximum operating range of the pump were performed with the results shown in Figure 7.8. For comparison purposes, the original calibration data is also shown. The deviation of the two measurement results with respect to the calibration data are plotted in Figure 7.8. As shown in Figure 7.8, the maximum deviation between the measured flow rate and the calibrated flow rate was within ±0.04m/s. The normalized repeatability of the sensor system respect to its dynamic range was therefore ±0.5 % of the full scale.

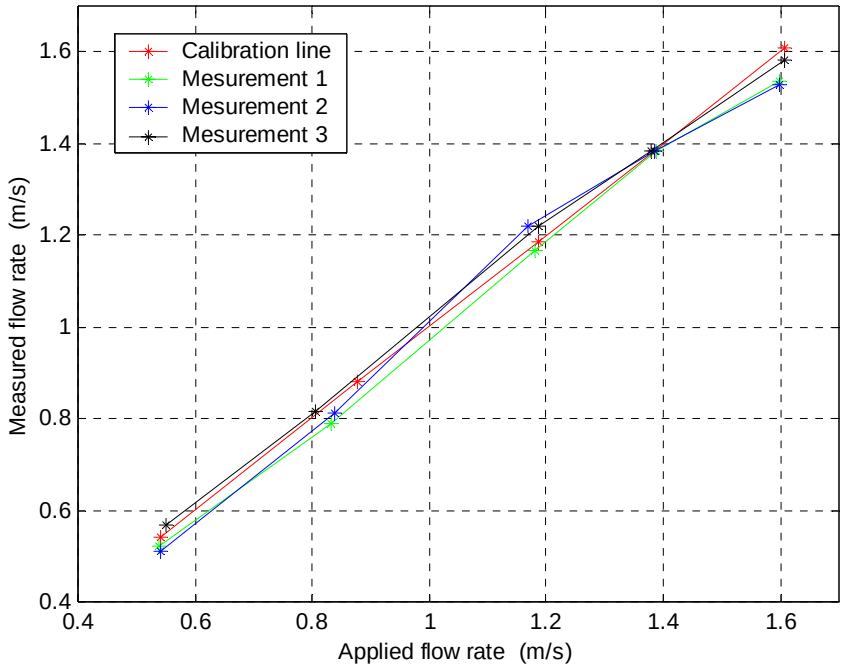

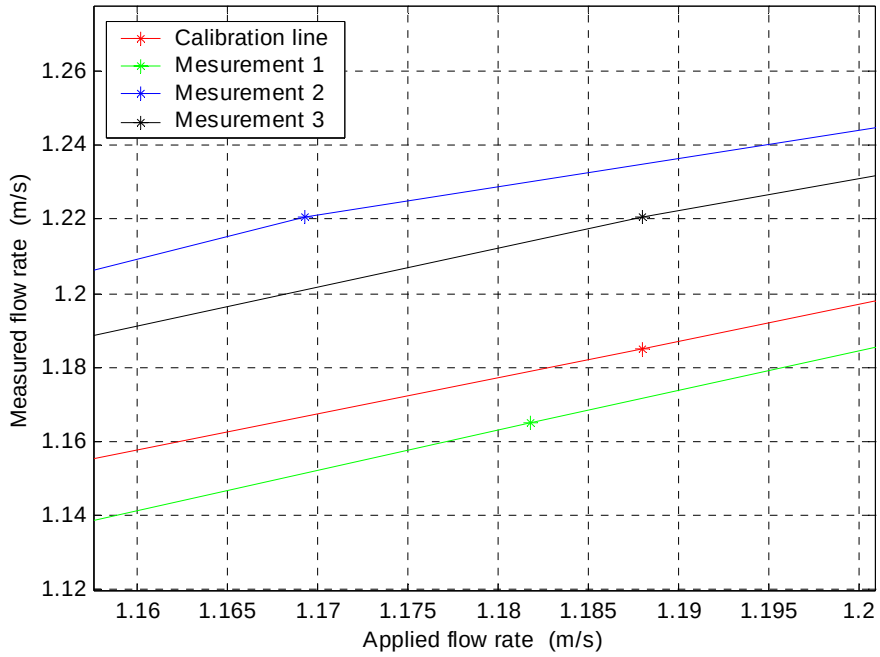

Figure 7.8 Repeatability test result of the pressure measurement

7.4.4 Long-term stability

The same flow sensor was also used to test the system stability. The sensor was kept in the testing pipes for 24 hours. The flow rate of the testing system was maintained to the 0.5m/s. The test result is shown in Figure 7.9. The maximum peak-to-peak flow rate within 24hour time was 0.016m/s. The test result also shows that the shift of the flow sensor system is not to one direction.

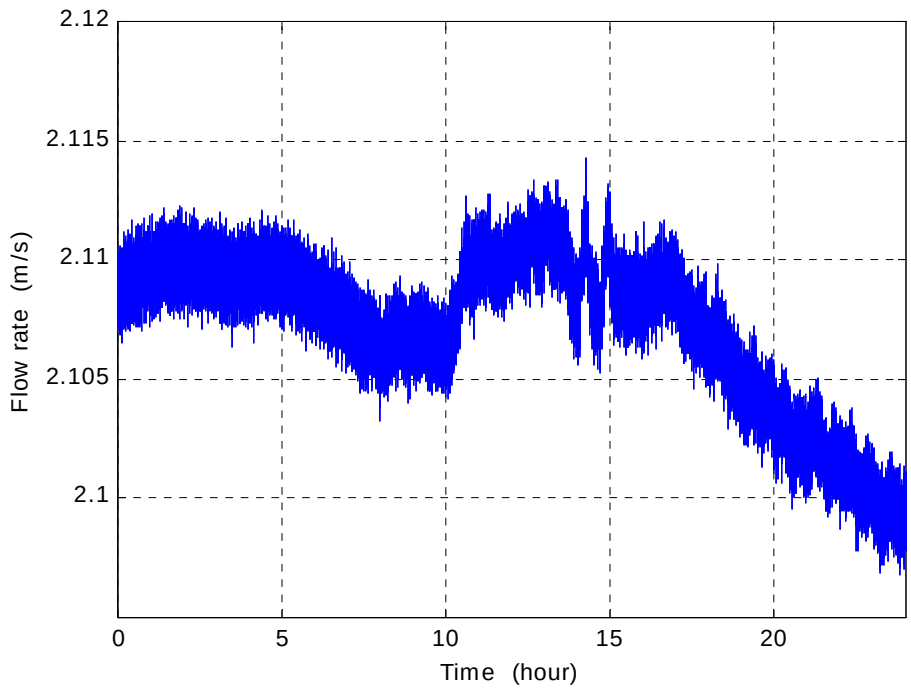

Figure 7.9 System stability testing over 24 hours

7.4.5 Opportunities for improvement

The flow measurement was realized by combining the EFPI sensor and cantilever beam technology together. By using two symmetrical EFPI sensors, the temperature dependence of the flow sensor has been minimized. A flow sensor testing system was also setup in VTPL to evaluate the performance of the flow sensor. Preliminary experimental results demonstrate the effectiveness of this structure.

Several problems, such as the hysteresis character and mechanical stability, need to be solved. The repeatability and the long-term stability still need be improved. These are the focus of future works.

8. Fiber optical acoustic sensor

Acoustic (or seismic) signal is another very useful information in down-hole oil recovery. The acoustic wave can generate very small pressure when it is propagating in the oil reservoir, therefore, the detection of the acoustic wave signals can be realized by using a fiber optic sensor with a high sensitivity and a high frequency responsibility. In this section, detailed work on the design and implementation of the acoustic sensors will be presented.

8. Principle

The basic principle and configuration of the fiber optic acoustic sensor can be illustrated using Figure 8.1. The system consists of a sensor probe, a light source, an optoelectronic signal processing unit, and an optical fiber linking the sensor probe and the signal-processing unit. As shown in the enlarged view of the sensor head, the input fiber and the thin silica glass diaphragm are bonded together in a cylindrical silica glass tube to form a Fabry-Perot sensing element.
Figure 8.1 illustrates the principle of operation of the diaphragm-based fiber optic acoustic sensor. The small pressure generated by an acoustic signal causes a deformation of the diaphragm and modulates the sealed air gap length. The sensor therefore gives outputs that correspond to the acoustic signals. Like regular interferometers, the measurement will have ultra-high sensitivity. On the other hand, however, the measurement would suffer from the disadvantages of sensitivity reduction and fringe direction ambiguity when the sensor reaches peaks or valleys of the fringes. One of the key successes of our sensor is that a controlled bonding technique is used to fabricate the acoustic sensor so that the sensor operates only over the linear range of a half fringe. As shown in Figure 8.2, the initial operating point is chosen to be the central point of the interference fringe, and the thickness of the diaphragm is designed in such that the imposed acoustic signal only deforms the thin diaphragm within the linear part of the sensor response curve. Therefore the sensitivity reduction and fringe direction ambiguity problems can be completely avoided.
It deserves special mentioned here that parallel with the fiber, a capillary was use to through into the inner hole of the ferrule, which is used as a pressure filter to transfer the pressure effect between the cavity and the outside. So when the sensor is deployed in the oil down-hole where there is high pressures, the sensor can compensate the high pressure automatically to isolate the pressure effect on the sensor.

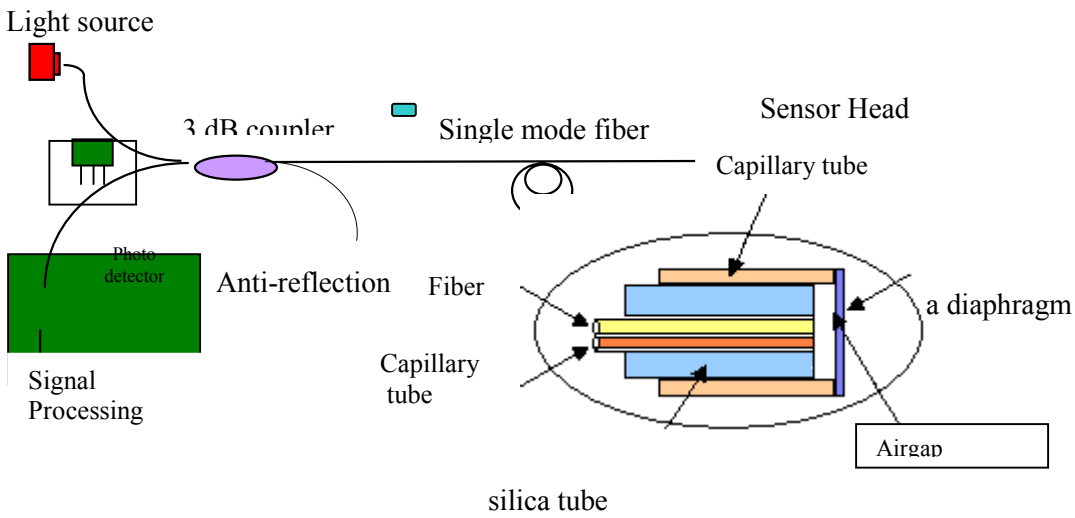

Figure 8.1 Illustration of the principle of the fiber optic acoustic sensor.

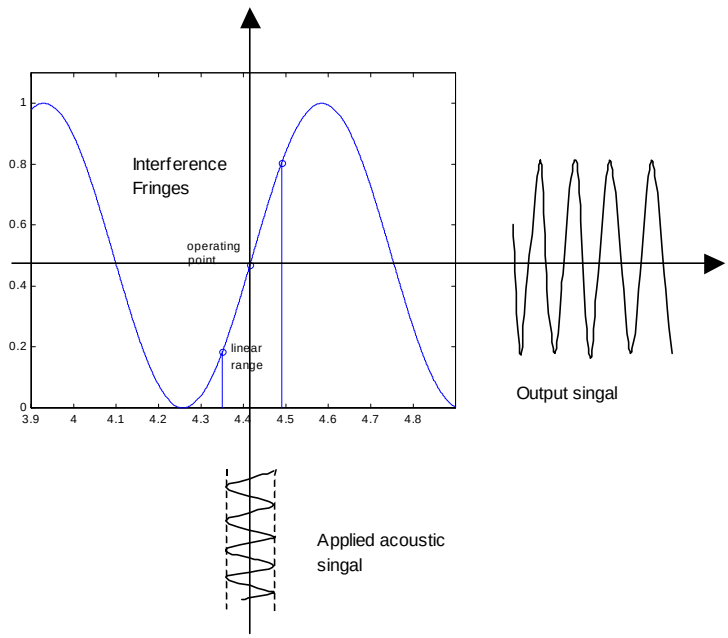

Figure 8.2 Illustration of a linear operating range of the sensor response curve.

2. Sensor frequency response and sensitivity design

We can use the structure shown in Figure 3 to model the acoustic sensor. The diaphragm vibrates at the presence of an acoustic wave when it imposes a dynamic pressure on the diaphragm. It is very important to design the sensor head to ensure high enough frequency response and

sensitivity to achieve optimum detection of the acoustic signals.

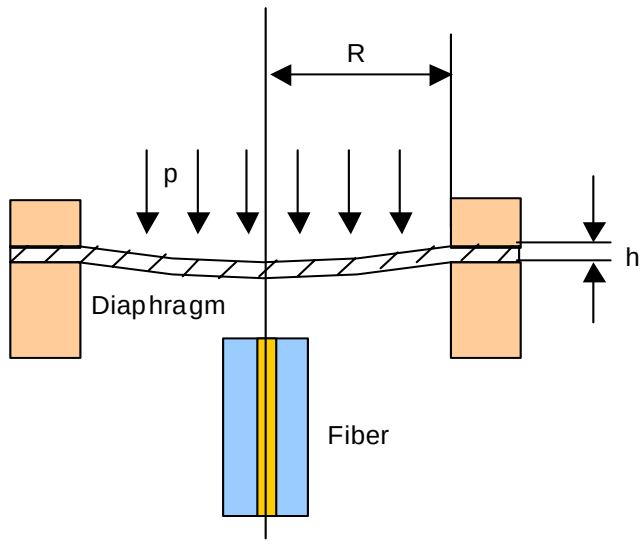

Figure 8.3 Structure model for diaphragm-based acoustic sensor

The frequency response of the sensor is limited by natural frequency (f_n) of the diaphragm. The natural frequency can be calculated by the following equation[3]:

$$f_n = \frac{\alpha}{2\pi R^2} \times \sqrt{\frac{Dg}{hw}} \tag{1}$$

where α is a constant related to the vibrating modes of the diaphragm, and takes a value of 10.21 for the fundamental mode; R is the effective radius defined by the inner diameter of the silica sensor-housing glass tubing; h is the thickness of the diaphragm; g is the gravitational constant; w is the specific weight of the diaphragm material (for fused silica at 25 C°, 2.202×10^3 kg/m^3); and D is the flexural rigidity of the diaphragm defined by

$$D = \frac{Eh^3}{12(1-\mu^2)} \tag{2}$$

where μ is the Poisson's ratio ($\mu = 0.17$ for silica glass material at 25°C); E is the Young's modulus of the silica glass material ($E = 73.73$ GPa or 7.49×10^9 kg/m^2 at 25°C); The frequency response of the sensor can thus be calculated by combining Equations (1) and (2) into

$$f_n = 2.749\times10^9 \frac{h}{R^2} \text{ (Hz)} \tag{3}$$

where h and R are in microns.

As indicated by Equation (3), the frequency response is proportional to the thickness of the diaphragm and inversely proportional to the square of the effective diaphragm radius. If we

choose the diaphragm with the effective radius of R= 1mm, we can plot the predicted frequency response of the sensor as a function of diaphragm thickness as shown in Figure 4. So as to a $100\,um$ -thickness diaphragm, the theoretical natural frequency response in air should be 274.9kHz. So any acoustic signals under this frequency can be detected by this diaphragm-based sensor.

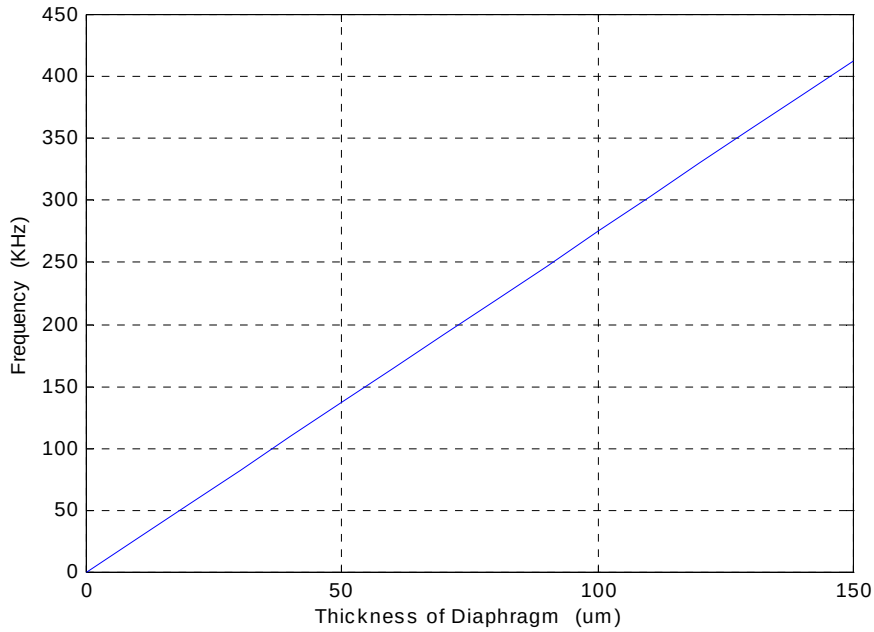

Figure 8.4 Predicted frequency response of the sensor at R=1mm

The diaphragm will be deflected when there is a differential pressure p between the inside and outside of the sealed cavity. The out-of-plane deflection of the diaphragm y as a function of the pressure difference at any radial position r is given by[3]

$$y = \frac{3(1-\mu^2)p}{16Eh^3} \times (R^2 - r^2)^2 . \tag{4}$$

In our sensor configuration, the fiber is positioned to the central part of the diaphragm so that only the center deflection y_0 is of interest, which is given by

$$y_0 = 1.71 \times 10^{-8} \frac{R^4}{h^3} p , \tag{5}$$

where again, y_0, R and h are all in microns, and p is in the pounds per square inch (*psia*).

From the above equations, it is seen that the sensitivity of the sensor can be designed to fit different application requirements either by choosing diaphragm materials with different μ and E

or by changing the geometric parameters of the sensor head with desired effective diaphragm size R and thickness h. In general, a diaphragm with a larger radius and a smaller thickness will render more sensitive detection of the acoustic signals. However, as indicated above, the operating range of the acoustic sensor head needs to be limited within the linear range, which is a fraction of an interference fringe in order to avoid the sensitivity reduction and fringe direction ambiguity problems. This imposes a limitation on the thickness of the silica diaphragm. Figure 5 shows the sensor response with R= 1mm predicted by Equation (5). Still as to a 100 um -thickness diaphragm, the theoretical pressure sensitivity in air should be 0.017um/psi.

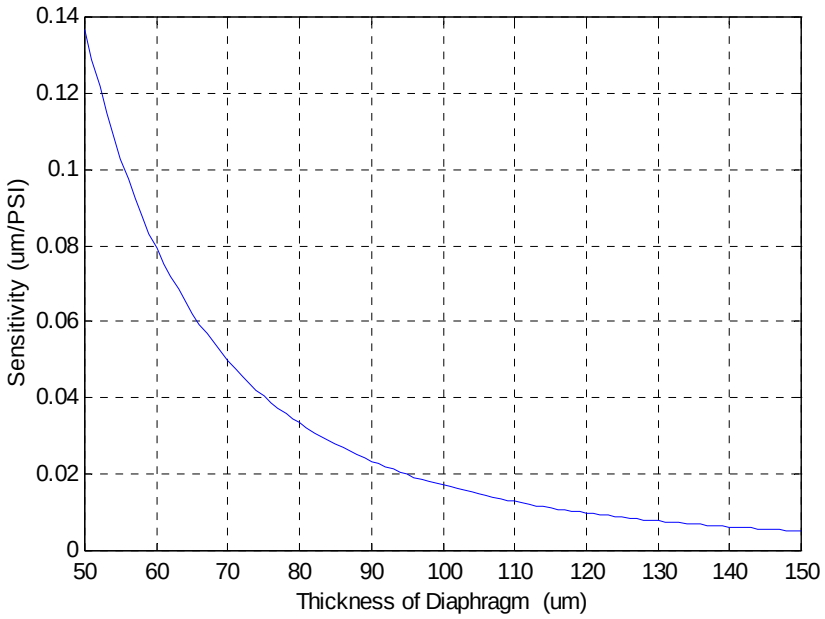

Figure 8.5 Theoretical sensor response (μm/ psi) versus diaphragm thickness at R= 1mm.

8.3 Acoustic sensor fabrication

Many bonding methods have been investigated to find a best approach to maintain both the mechanical strength and temperature stability. To test the structure of the high pressure isolation, at these period, epoxy bonding method was used to fabrication the acoustic sensor head which is easy to do because only the normal temperature processing is need.

The white-light fiber interferometric system is used to monitor the change of the air gaps in the sensor head. Because the tunable laser will be used as the light source, so now the original air gap

of the sensor can be select at any effective value only to sure that the sensor head have the enough visibilities separately for the detected acoustic waves. The fabrication steps include polish the end of single mode optical fiber,silica ferrule and silica tube separately; put the diaphragm above the flat endface of the tube and bonding them with Epoxy-907; at the same time through the fiber and capillary tube into the silica tube, sure of the end faces of fiber and capillary tube out of the ferrule another end face then bonding them together; when both of them are dry after the solidification time, through them in to the silica tube, adjust the distance between the fiber's endface and diaphragm carefully to get the high visibility, bonding the diaphragm when the suitable interference airgap was found, then using Epoxy-907 to bonding them together. The airgap and visibility of the sensor head will change during the solidification, usually by adjust the laser wavelength of the tunable laser, still we can found the suitable airgap.

8.3.1 Setup of acoustic sensor testing system

To evaluation the performance of acoustic sensors, the test system was setup to the performance of the flow rate sensors which is illustrated in Fig.8.4. A WDU transducer is used to generated the ultrasonic signal by input the pulse signal from a C-101-HV-2014 pulser. Also a WDU piezo-electric sensor is used as the standard to calibrate the fiber optical sensor. A 1221A preamplifier is used to amplifier the detected acoustic signal from the WDU sensor. The WDU piezo-electric sensor and the fiber optical sensor were put into the water box to detect the acoustic signal from the WDU transducer. Both the amplified signals from two sensors are put into the two channels of Lecroy 505 digital storage oscilloscope e, so by compared these two outputs the fiber optical acoustic sensor can be calibrated. Figure 8.7 shows out the experiment setup that used for acoustic sensor testing.

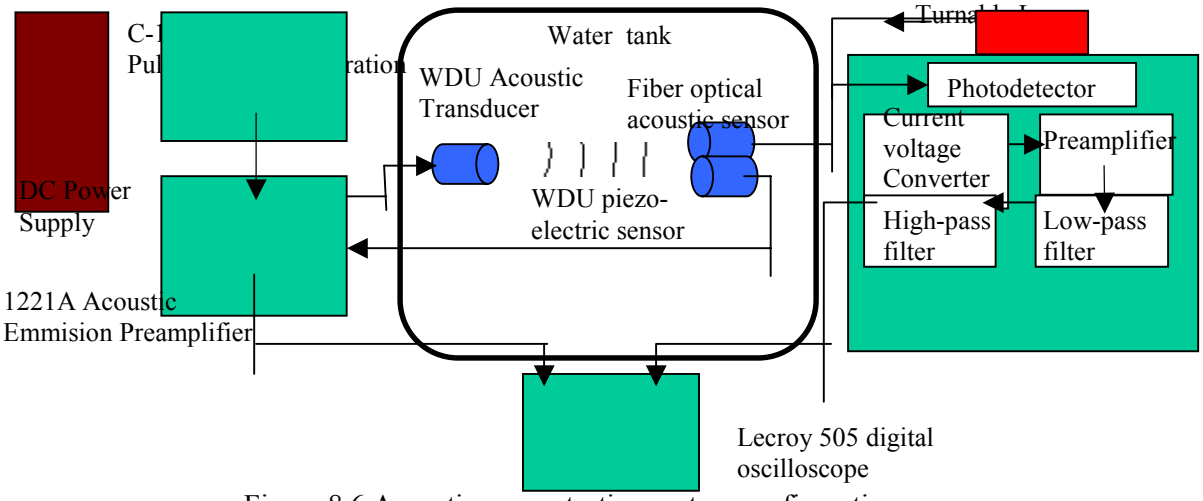

Figure 8.6 Acoustic sensor testing system configuration

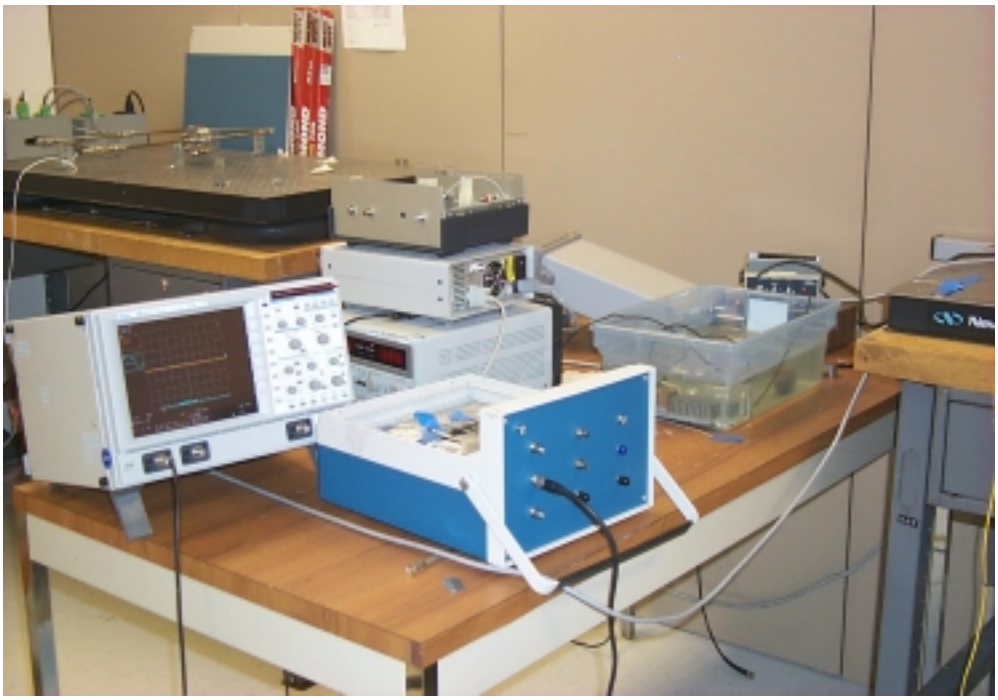

Figure 8.7 Picture of acoustic testing system

8. 4 Experiments

Based on above testing system, some experiments were done to test the basic characteristics of the fiber optical acoustic sensors. Some data of a fiber optical acoustic sensor with 1mm-diamter, 100um-thickness diaphragm is shown here.

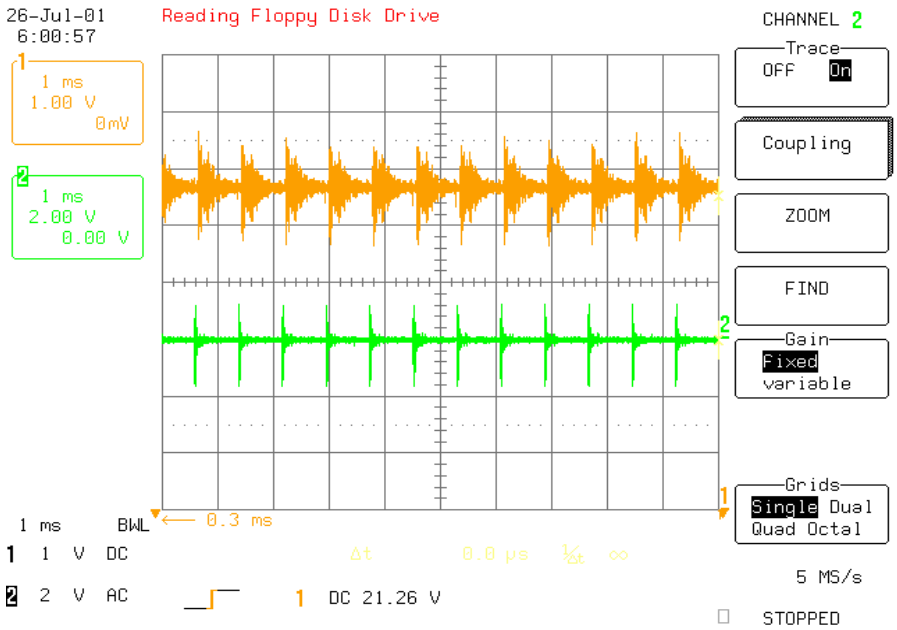

Figure 8.8 (a) Acoustic signal from Lecory 505 oscillograph

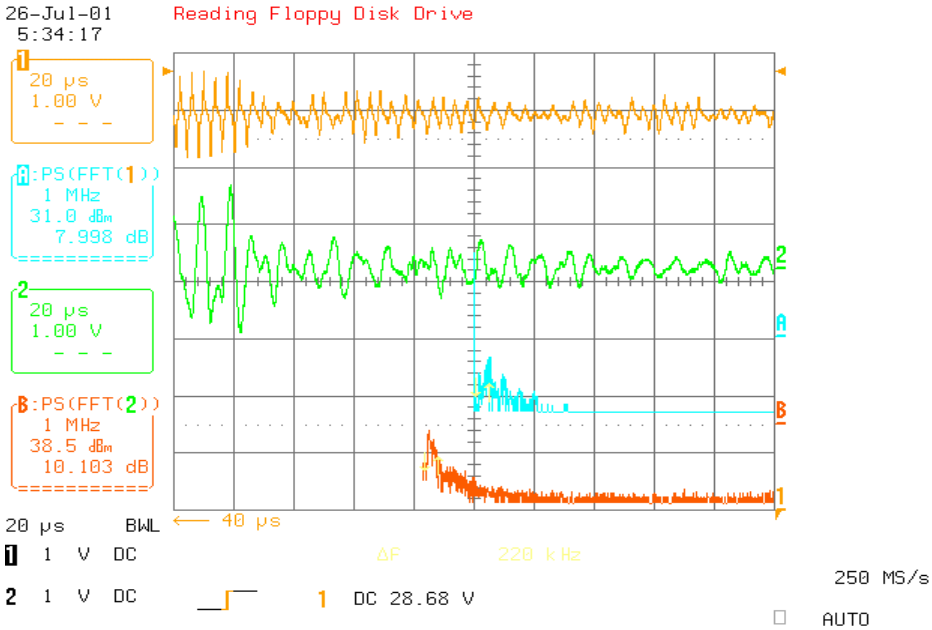

Figure 8.8 (b) Enlarge of Acoustic signal from Lecory 505 oscillograph

Figure 8.8 Compare of Acoustic signal from acoustic actuator(Yellow) and acoustic sensor(Green)

Drove by the pulse signal from C-101-HV-2014 pulser, the acoustic waves are generated and transfer to the sensors by water with fundamental frequency as f=130kHz and its harmonic components. The output of Figure 8(a) illustrates a series detected signals from the fiber optic

sensor and the WDU sensor. From the Enlarge signal of Figure 8(b). From the FFT results, it is clear that fiber optical acoustic sensor can trace acoustic signals very well.

To detect the pressure sensitivity of the acoustic sensor, the static water pressure was added to the sensor head and the single-mode white light system was used to detect the air gap changes of the acoustic sensor.

The relation between the static pressure and the air gap was shown in Figure 9, the sensitivity is around 0.008nm/Psi which near to theoretical value. So if we select the thin diaphragm, according to the equation (5), we can get very high sensitivity using this kind of acoustic sensor.

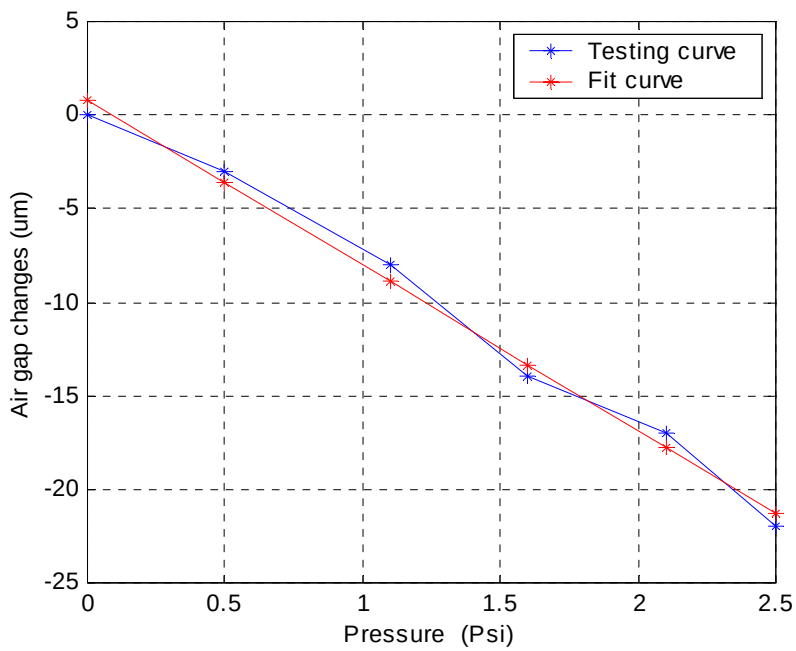

Figure 8.9 Pressure sensitivity of fiber optical acoustic sensor

This demonstrates that fiber optical acoustic sensor can respond to the acoustic sensor with high sensitivity in lab. The results above give us confidence that the developed fiber optic sensor system has the capability for precisely detecting in downhole.